

Circumstellar Environment

W.C. Danchi

UC Space Sciences Lab
University of California, Berkeley

OUTLINE

- TUTORIAL MATERIAL
 - Types of geometries
 - What has been done
 - Radiative xfer models / Spherical
 - Disk models
- LATE STARS
 - EVOLUTION FROM SIMPLE TO COMPLEX MODELS
 - MOLECULES
- FU OR, Disk ?
- δ Cas - Disks, 1 armed density wave.
- APERTURE MASKING - @ KECK - $2\mu\text{m}$
 - REAL MAPS
 - DIFFERENT TYPES OF GEOMETRIES OBJECTS
 - EVOLUTION - TIME VARIATION.

CIRCUMSTELLAR ENVIRONMENT.

- MATERIAL AROUND STARS

- Physical Conditions

- Temperature + density structure

- Dust, molecules, ions

- kinematics

- MANY TYPES OF GEOMETRIES

- Spherical shells - continuous - many

- multiple - α Ori
NAL Tam

- Clumps - θ Cet, IRC + 10216

- Disks - Be Stars, τ Cas

- FU Ori, MWC 349, LkHa 101
C116

EXAMPLES OF STARS THAT HAVE BEEN STUDIED ...

1. LATE STARS -

SUPERGIANTS

MIRA VARIABLES

CARBON STARS

SEMI-REGULAR

IRREGULAR

11 μm - ISI

2 μm - Keck

" - PTI

2. WOLF-RAYET STARS

" HIGH MASS EVOLVED STARS -

2 μm Keck

3. HERBIG Ae/Be STARS

MED. / HIGH MASS YSOs

(DUSTY - WC9...)

2 μm Keck

11 μm ISI

4. Be STARS - EMISSION LINES

γ Cas, η Tau, ϕ Per, (H α)/cont.

χ Per, χ Per, ζ Tau, β CMi

Optical - M λ III

GI2T

5. T-TAURI STARS - YSOs

Fu Ori

PTI

GEOMETRIES ...

- SPIRALS - WR 104, WR 98A

- JETS - ...

ISI Personnel

Science Team:

M. Bester (now in Space Physics Group)
W.C. Danchi (PI)
E.A. Lipman (just graduated, Ph.D.)
J.D. Monnier (Ph.D. student)
C.H. Townes (PI)
P.G. Tuthill (Post-doctoral)

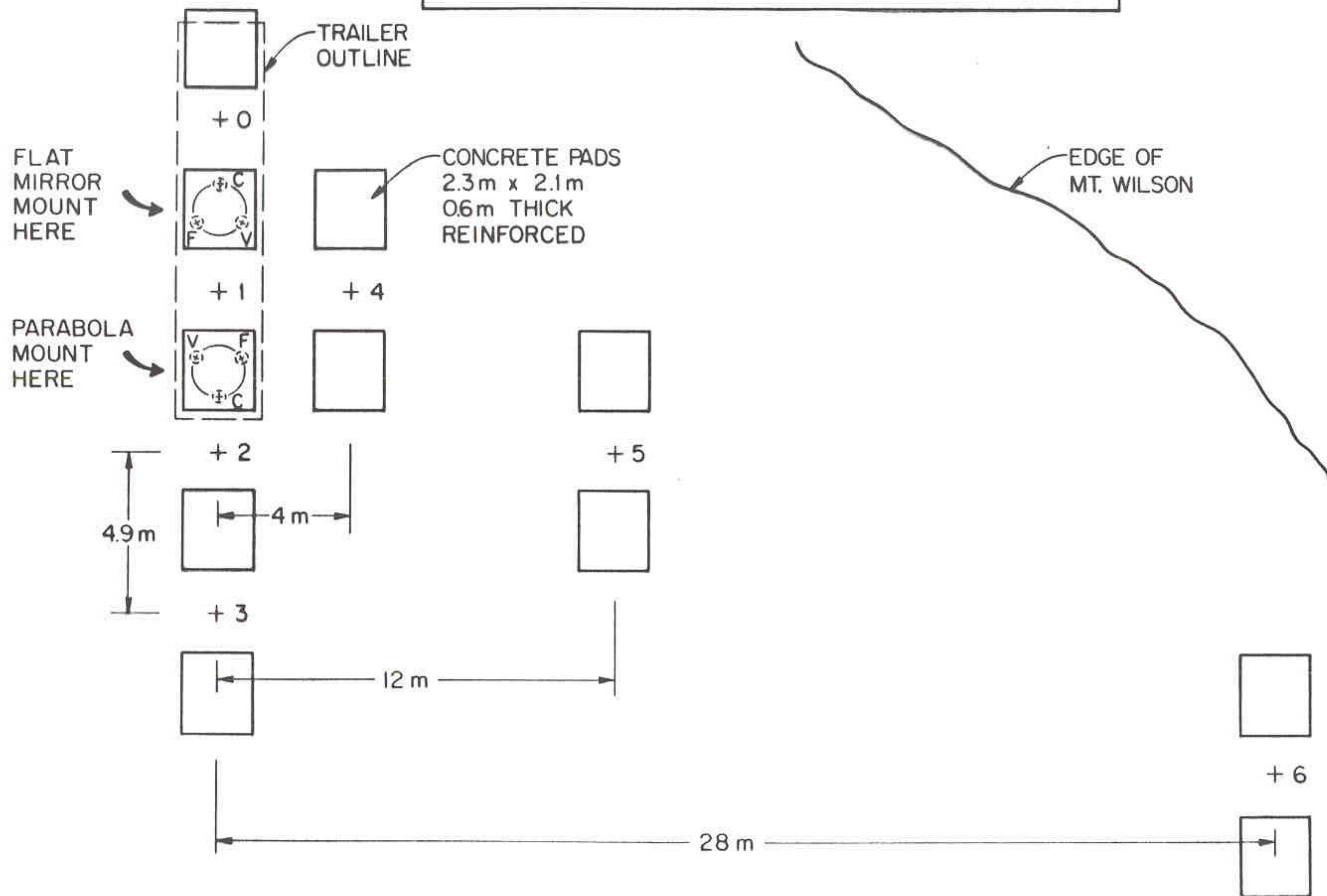
Engineering and Programming

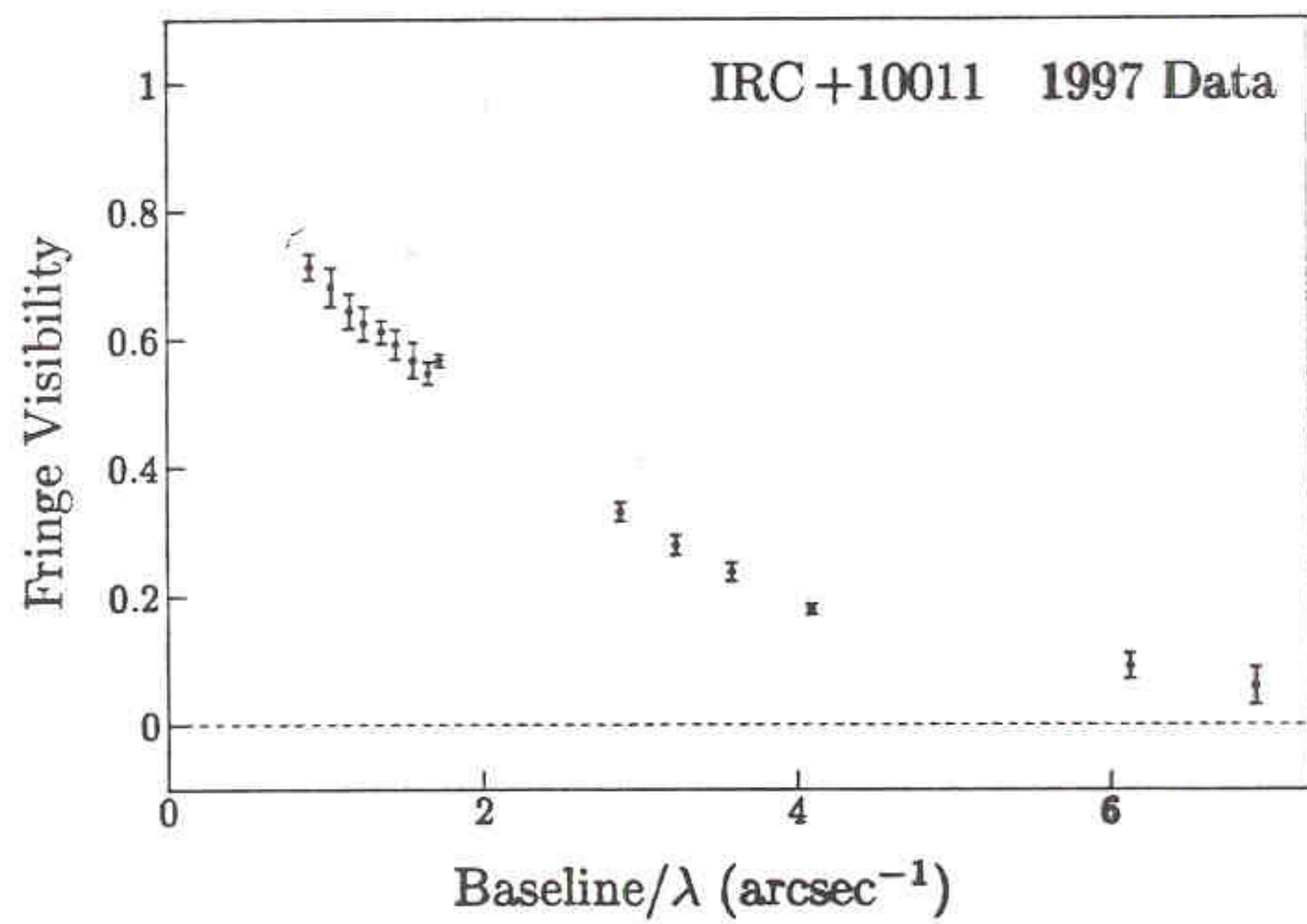
P. Barale
W. Fitelson
J. Hudson
J. Penegor
D. Hale

Collaborators

C. Degiacomi (Cologne)
T. Geballe (UKIRT, now Gemini)
L. Greenhill (CfA)
J. Lefevre (Nice)
B. Lopez (Nice)
D. Mekarnia (Nice)
M. Johnson (LLNL)

INITIAL SITE AT MT. WILSON
U.C. BERKELEY—INFRARED SPATIAL INTERFEROMETER





GOALS OF OBSERVING PROGRAM

MEASURE

- SIZES
- SHAPES
- OPTICAL DEPTHS
- DYNAMICS
- WAVELENGTH DEPENDENCE
- TIME EVOLUTION
- SPECTRAL LINES

MEASUREMENTS TELL US

1. TEST THEORIES OF DUST PRODUCTION
+ MASS LOSS MECHANISMS
2. CONSTRAIN OPTICAL PROPERTIES OF DUST.
3. HELP UNDERSTANDING OF STELLAR
EVOLUTION ON AGB.
4. SPECTRAL LINES PROBE ASTROCHEMISTRY
 - i.e. IMPORTANCE OF GRAINS
 - TEMP. + DENSITY STRUCTURE
OF GAS ENVELOPES.

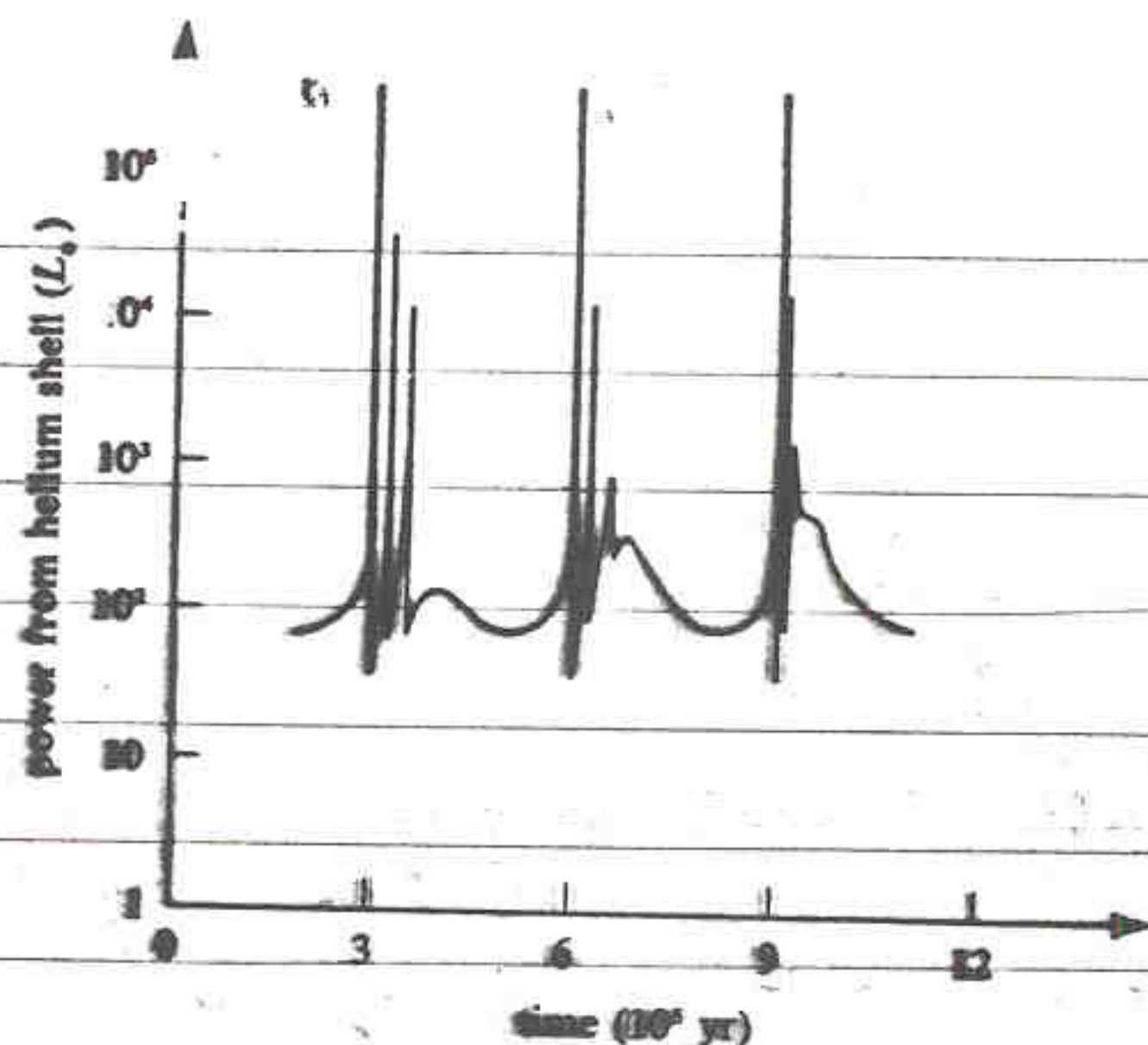


Figure 8.9. Thermal relaxation oscillations associated with helium-shell flashes. (Adapted from M. Schwarzschild and R. Härm, *Ap. J.*, 130, 1967, 961.)

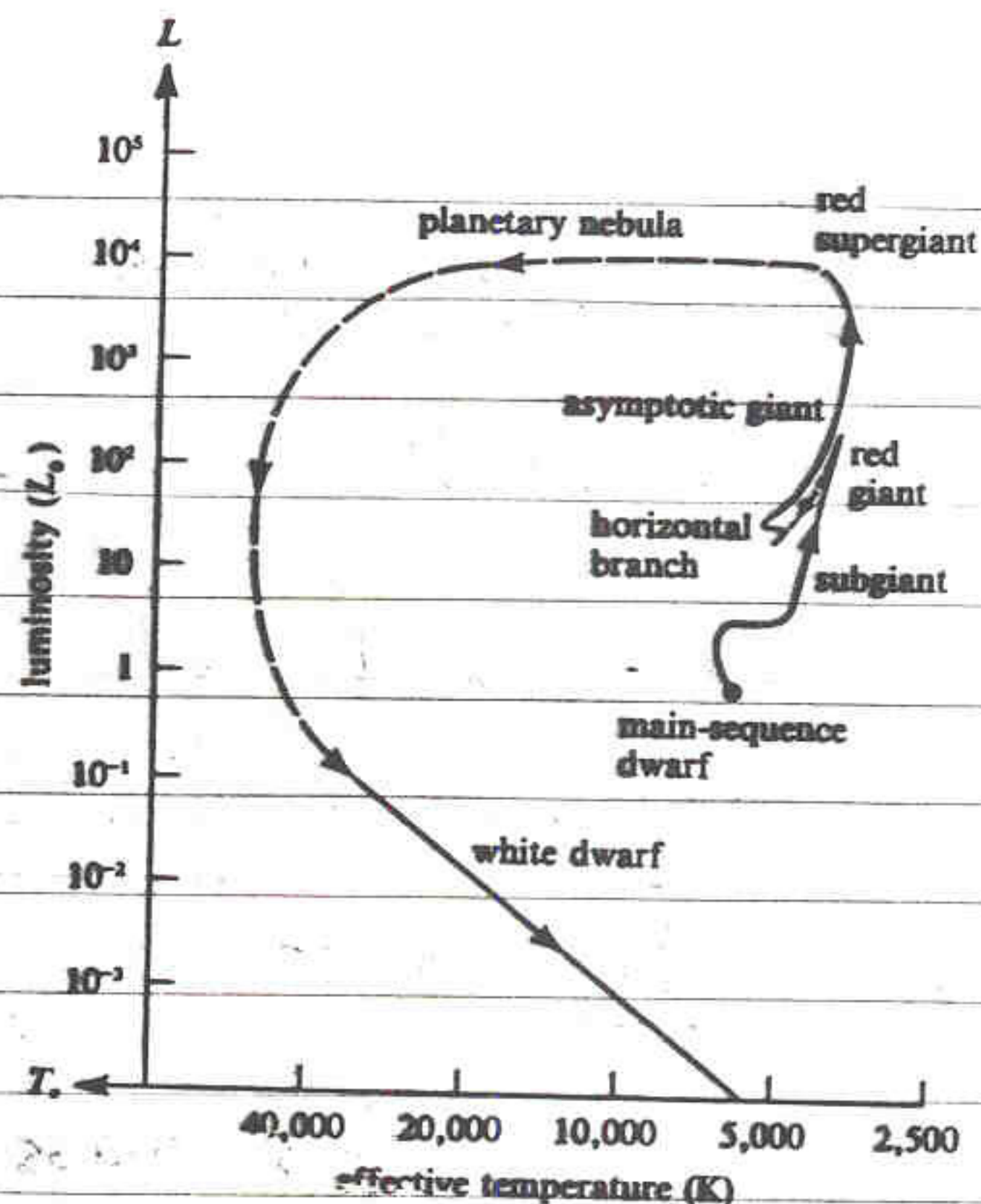


Figure 8.10. The complete evolution of a low-mass star from the main sequence to white dwarf. The track from the asymptotic giant branch to white dwarf (or a planetary nebula) is uncertain and is shown as a dashed curve.

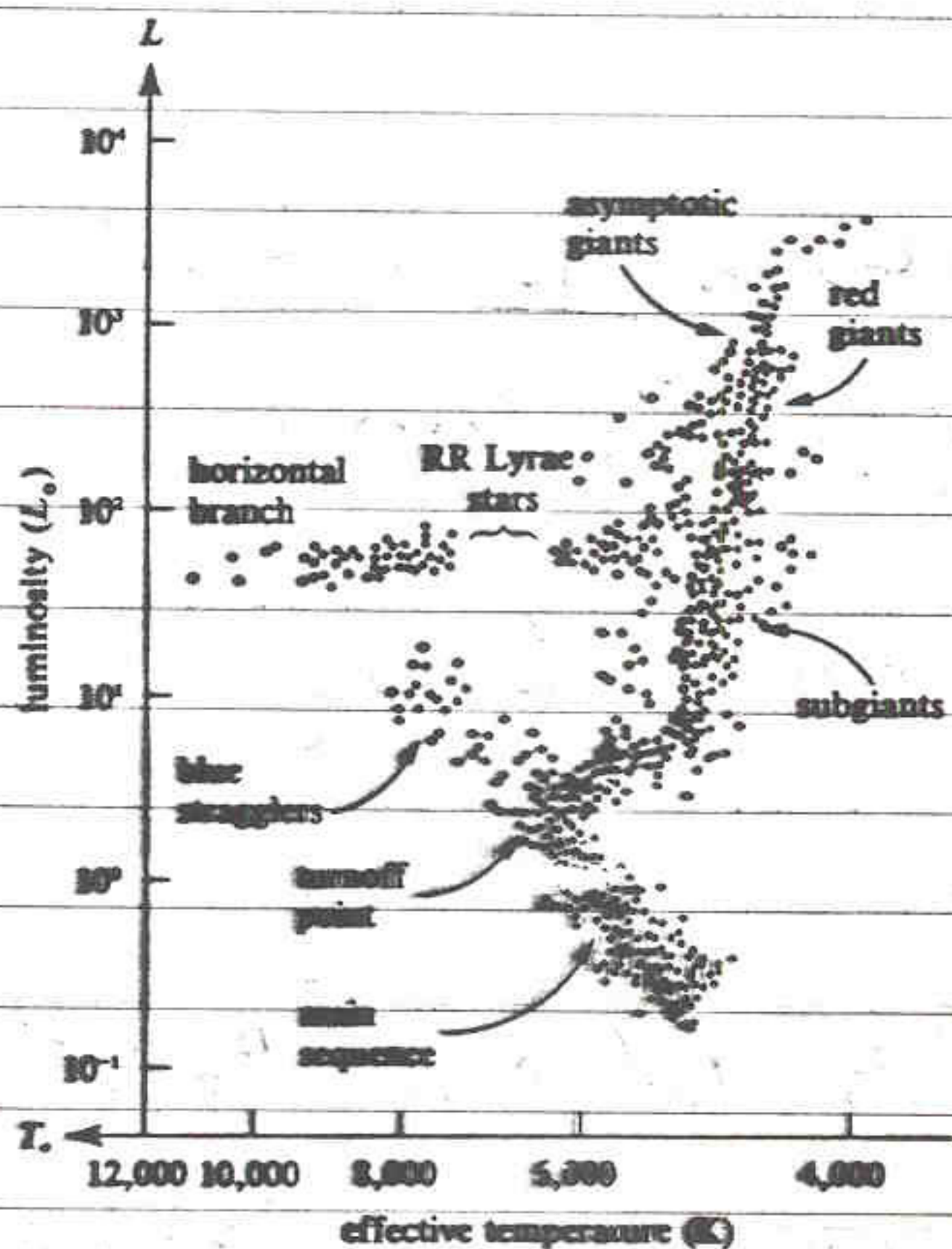


Figure 9.13. Schematic H-R diagram of the globular cluster M3. The distance to the cluster has been derived on the assumption that the luminosity of the RR Lyrae stars is $50L_{\odot}$. The diagram is somewhat schematic, because the conversion from the $B-V$ and V measurements of Johnson and Sandage to T_e and L is somewhat uncertain for Population II stars. (Adapted from H. L. Johnson and A. R. Sandage, *Ap. J.*, 124, 1956, 379.)

HORIZONTAL BRANCH

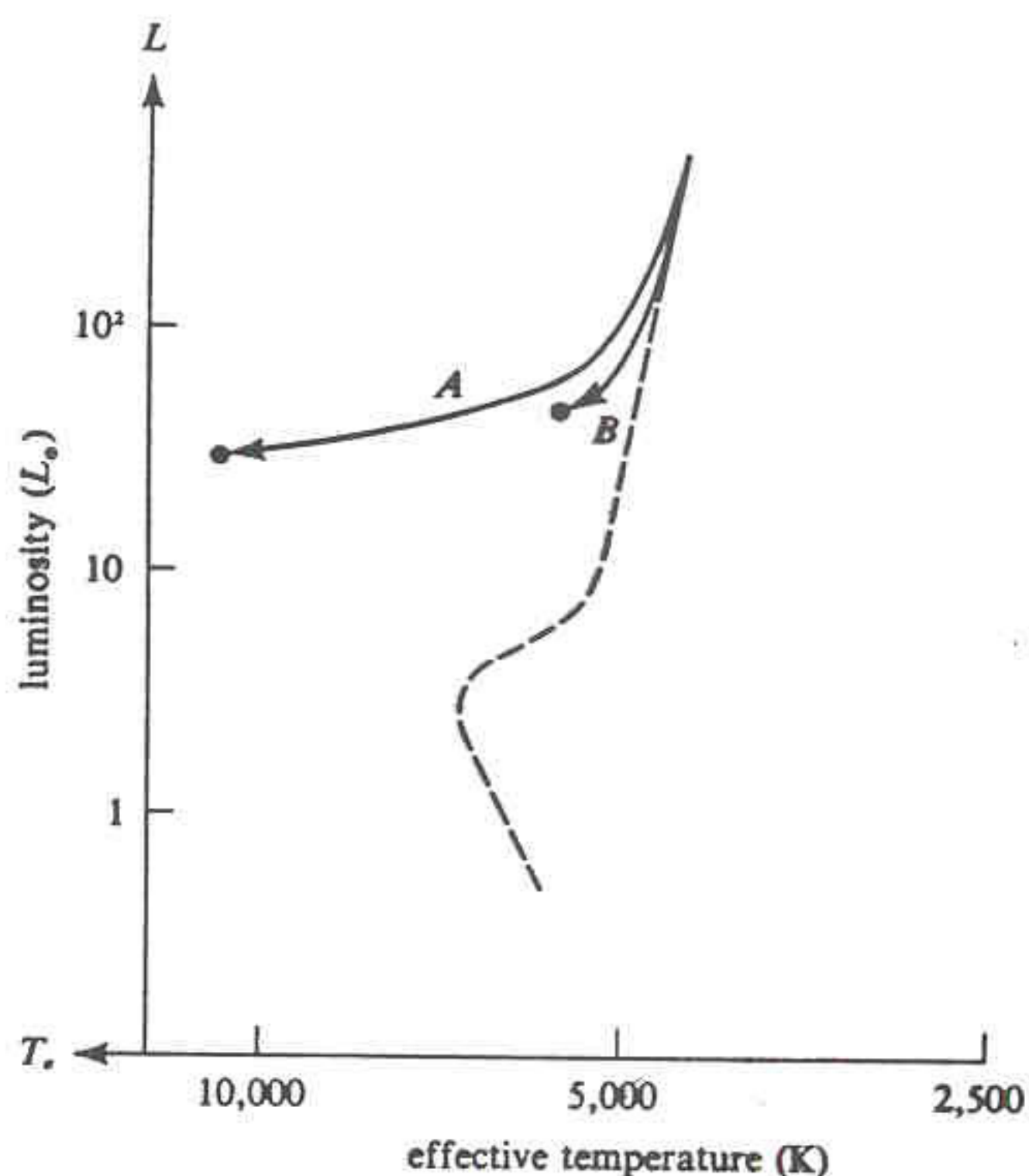


Figure 8.6. Descent of a low-mass star with poor heavy-element abundances (Population II star) from the tip of the red-giant branch to the horizontal branch. Track A corresponds to a star which suffered a relatively large loss of mass during the red-giant phase of stellar evolution. Track B corresponds to a star which suffered relatively little loss of mass. (Adapted from Icko Iben, *Ann. Rev. Astr. Ap.*, 5, 1967, 571.)

ASYMPTOTIC GIANT

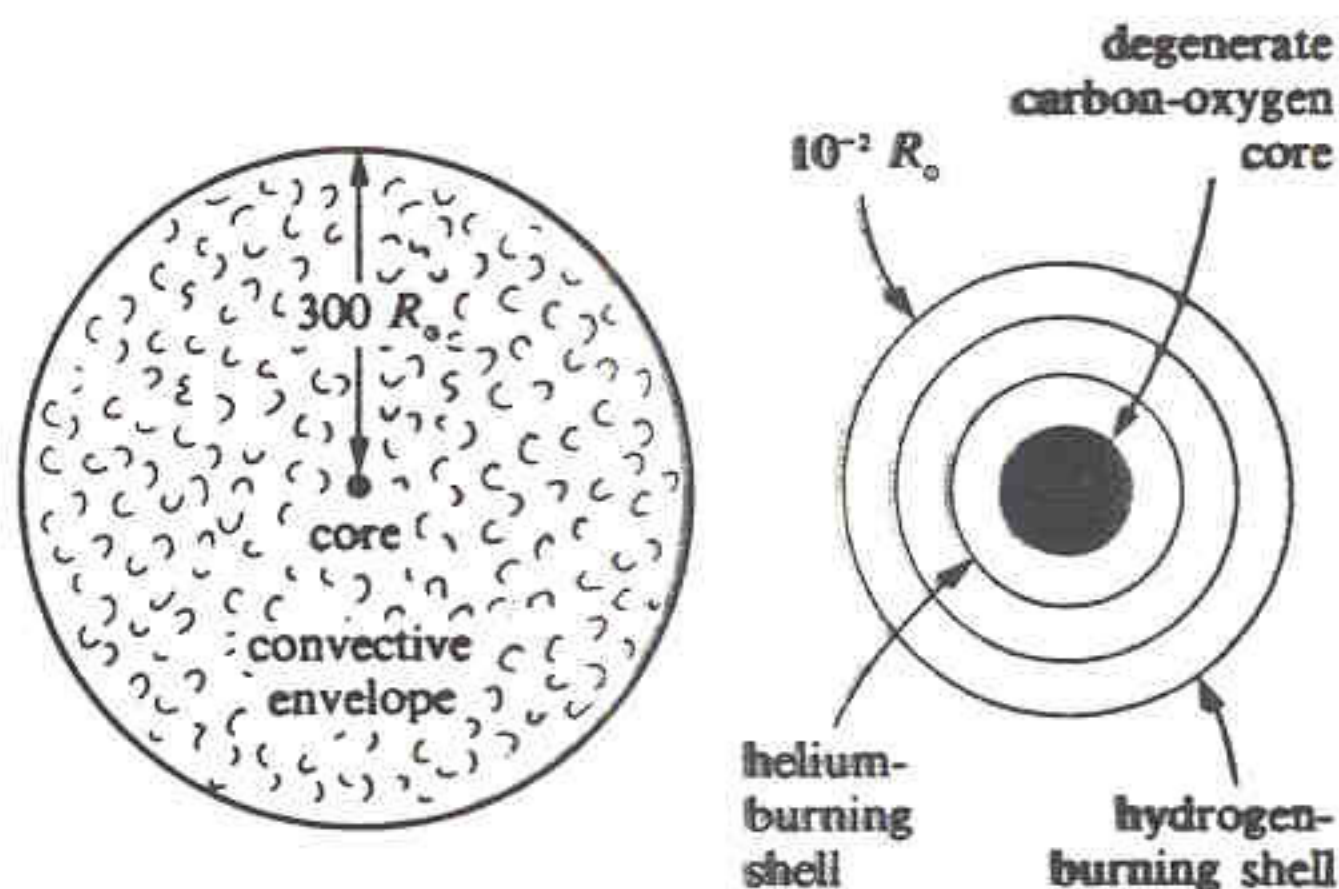


Figure 8.8. The structure of an asymptotic giant. The figure on the left shows the entire star from core to photosphere. The figure on the right shows an enlarged picture of the region near the core.

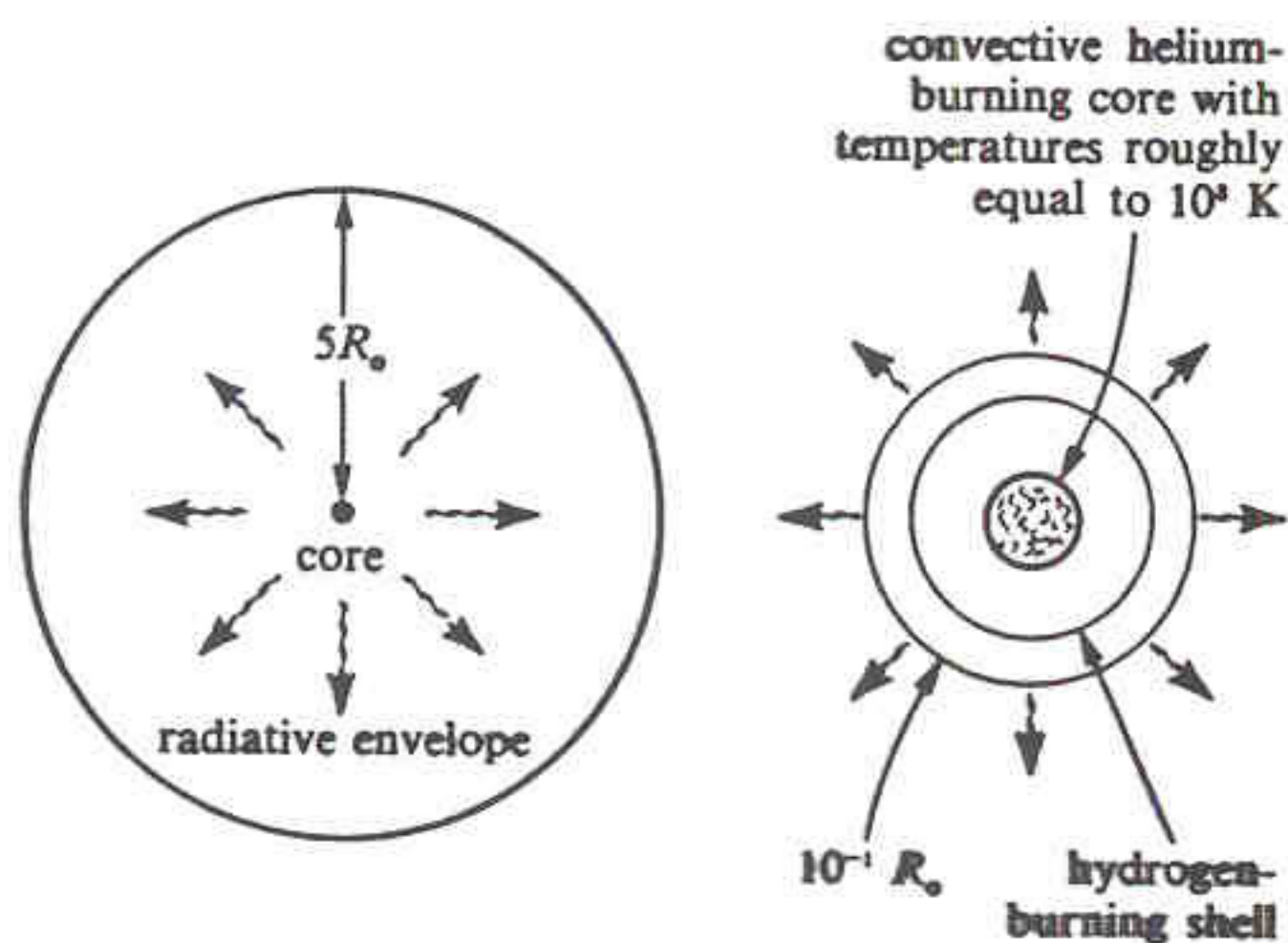


Figure 8.7. The structure of a horizontal-branch star. The left figure shows the entire star from core to photosphere. The right figure shows an enlarged picture of the region near the core.

* OBSERVED A LIST OF ABOUT 20

MIRAS, SUPERGIANTS, C, S STARS
(OBSERVED MANY OVER SEVERAL YEARS.)

* PUBLISHED A NUMBER OF RESULTS
STARTING IN 1990.

* IN THIS TALK I WILL SUMMARIZE

$\frac{1}{2}$ SOME OF THESE RESULTS AND SHOW
SOME NEW ONES.

$\frac{1}{2}$ * DISCUSS NEW & EXCITING APERTURE
MASKING RESULTS.

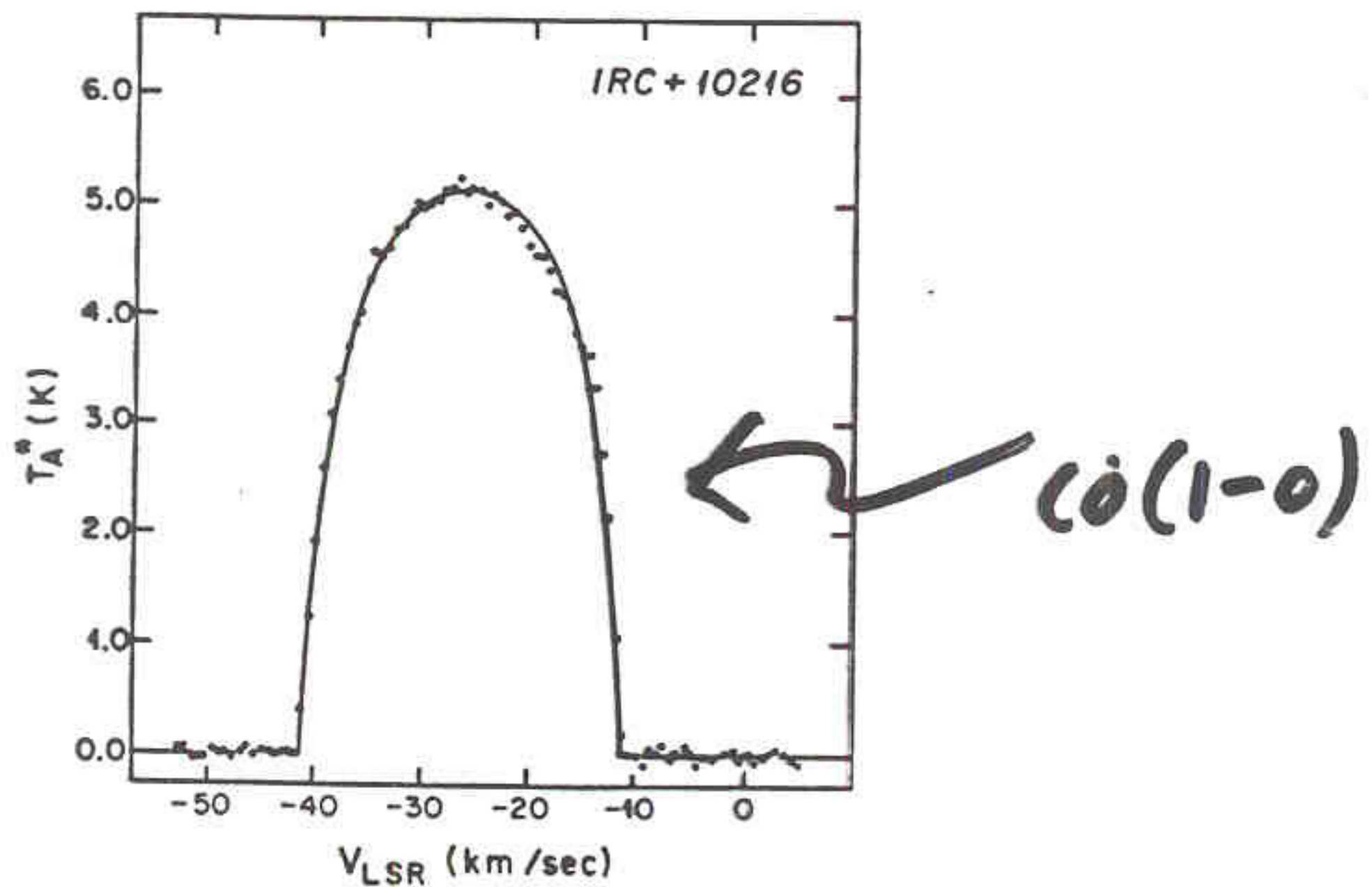


FIG. 2.—The CO(1-0) line profile of IRC + 10216. The fitted curve is a flattened parabola (see text).

KNAPP & MORRIS (1985)

MASS LOSS TRADITIONALLY STUDIED
VIA MOLECULAR TRANSITIONS OF CO
& OTHER MOLECULES, WITH VERY LOW
SPATIAL RESOLUTION, i.e.

ARC SECS \rightarrow ARC MINS

TIME SCALES \rightarrow 100's \rightarrow 1000's OF
YRS.

DUST FORMATION PROCESS

180

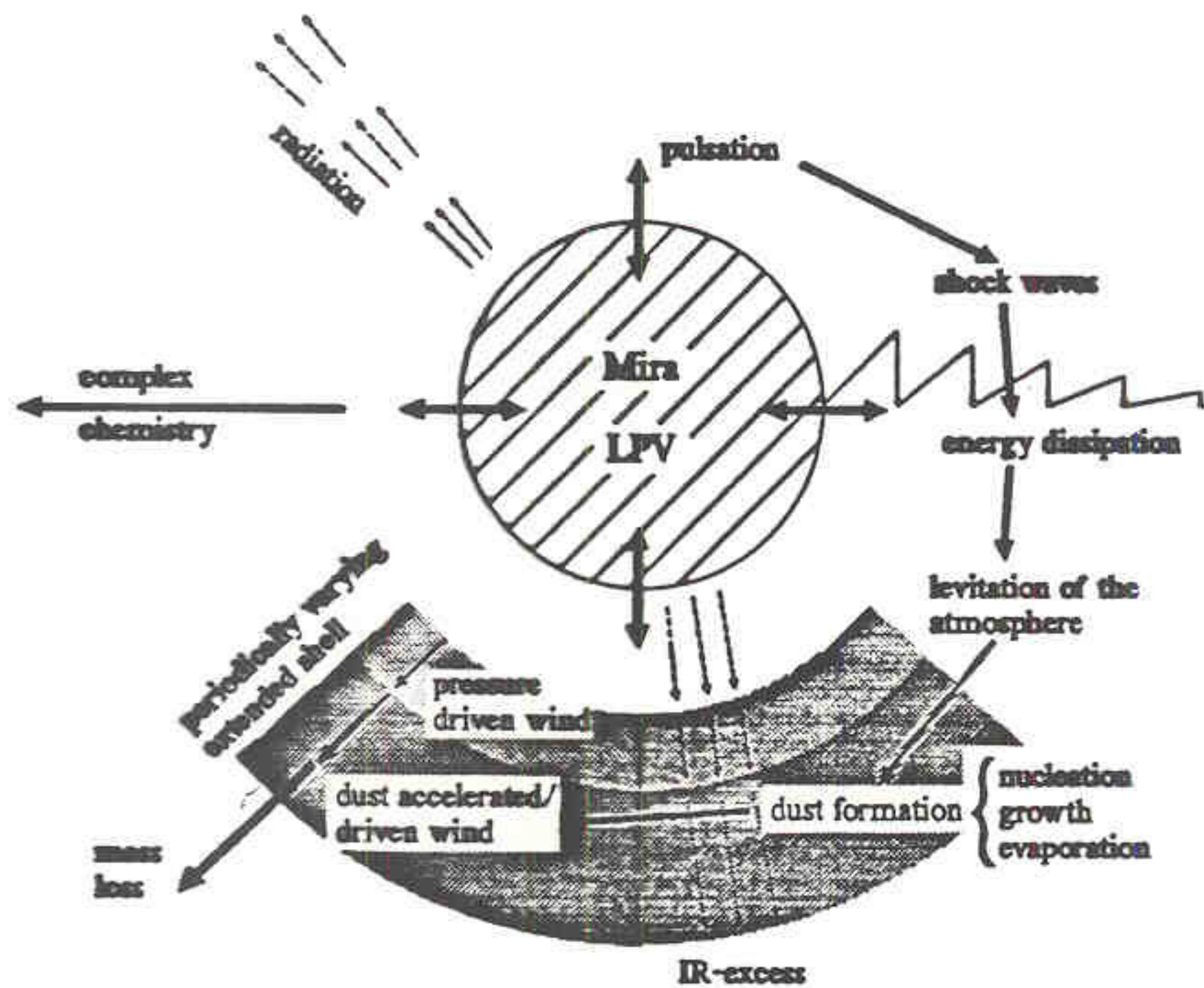
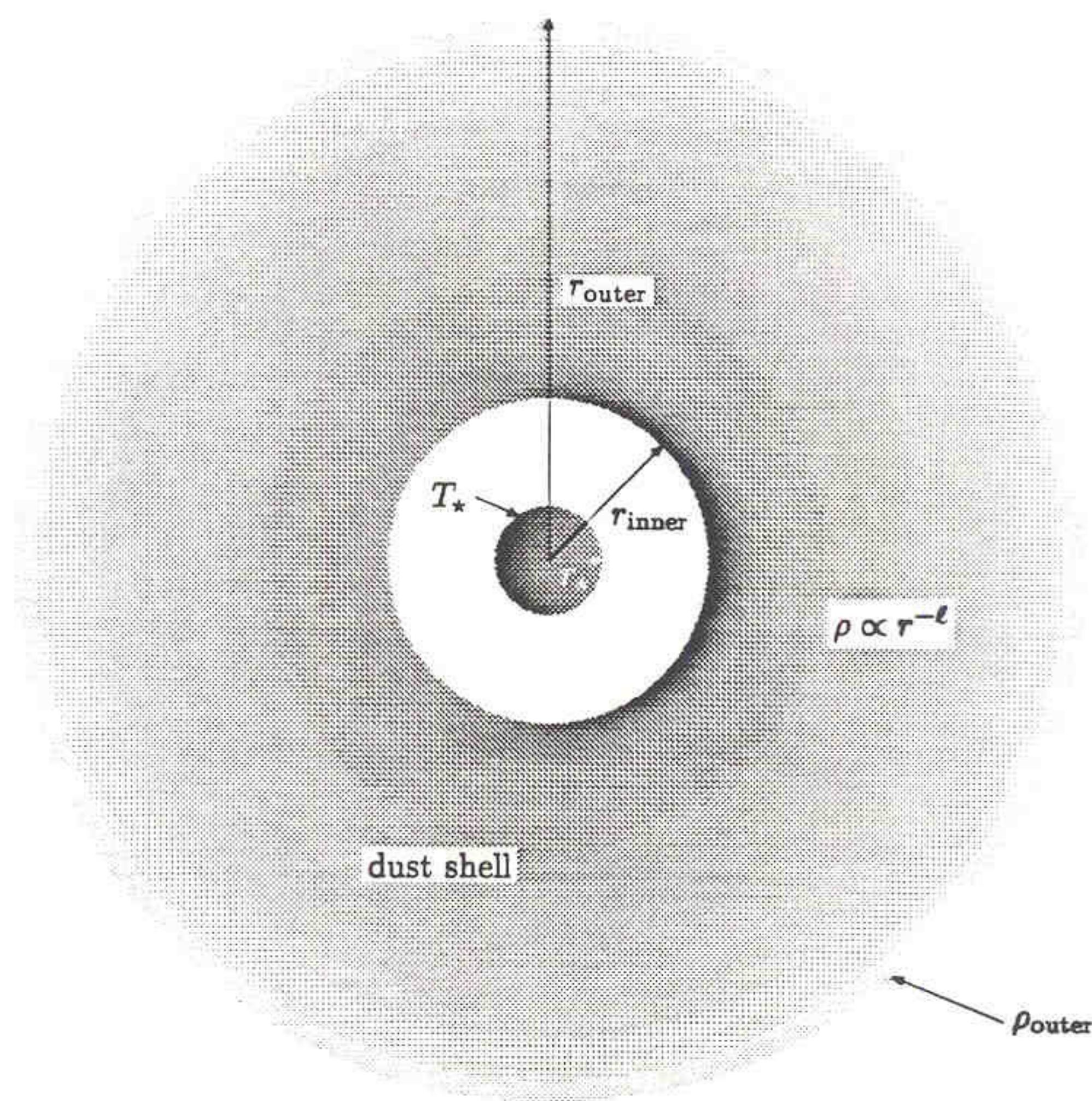


Fig. 1: Scenario of a pulsating variable showing the global shell structure and depicting essential physical "ingredients".

BASIC IDEA:

- 1) SHOCK WAVES LEVITATE ATMOSPHERE
- 2) DENSITY HIGH FAR ENOUGH FROM PHOTOSPHERE TO NUCLEATE DUST
- 3) RADIATION PRESSURE ON DUST CAUSES IT TO ACCELERATE.
- 4) GAS ACCELERATED BY COLLISIONS WITH DUST.



Model Calculations

Radiative Transfer Equation:

$$\frac{dl_v}{ds} = -\alpha_v I_v + j_v$$

where I_v = specific intensity
 α_v = absorption coefficient
 j_v = emission coefficient

with optical depth $d\tau_v = \alpha_v ds$ or $\tau_v = \int_{s_0}^s \alpha_v ds'$

and source function $S_v = \frac{j_v}{\alpha_v}$ we get:

$$I_v(\tau_v) = I_v(0) e^{-\tau_v} + \int_0^{\tau_v} S_v(\tau_v') e^{-(\tau_v - \tau_v')} d\tau_v' \quad (*)$$

we assume: • thermal equilibrium ($\rightarrow S_v = B_v(T)$) Planck law
 • spherical symmetry
 • temperature profile $T \propto r^{-\alpha}$ ($\alpha = 0.4$) ✓
 • density profile of dust $\rho \propto r^{-\beta}$ ($\beta = 2$) ✓

by integrating (*) for each ray and calculating the Fourier Transform one gets the **visibility**

comparison with our observations \rightarrow temperature and radius of dust shell

Modelling Basics:

[Based on work of Wolfire and Cassinelli (1986)]

FULL RADIATIVE TRANSFER CODE:

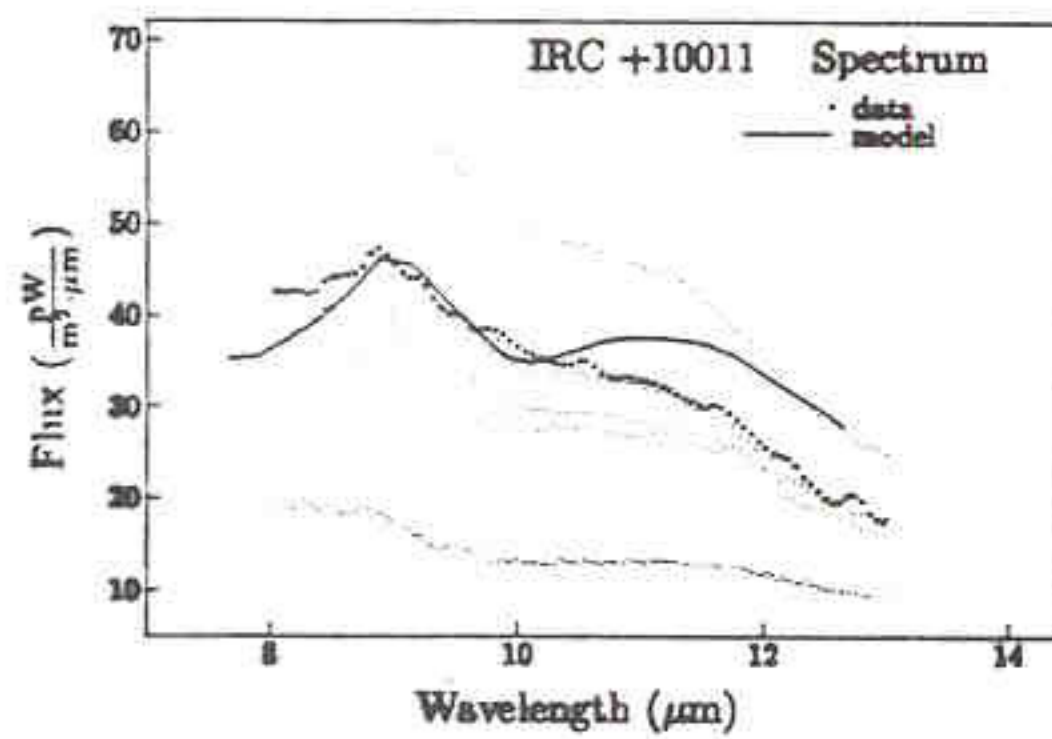
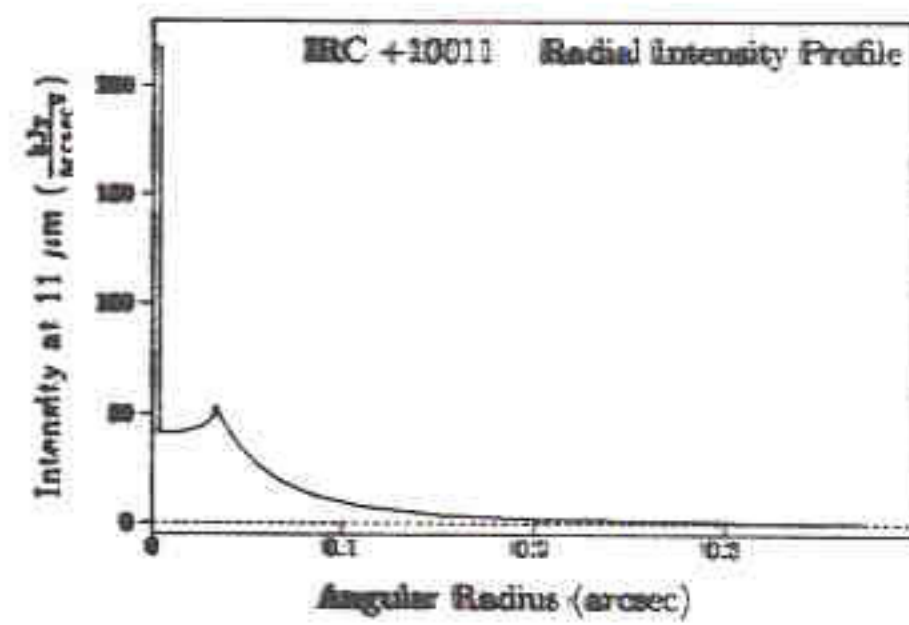
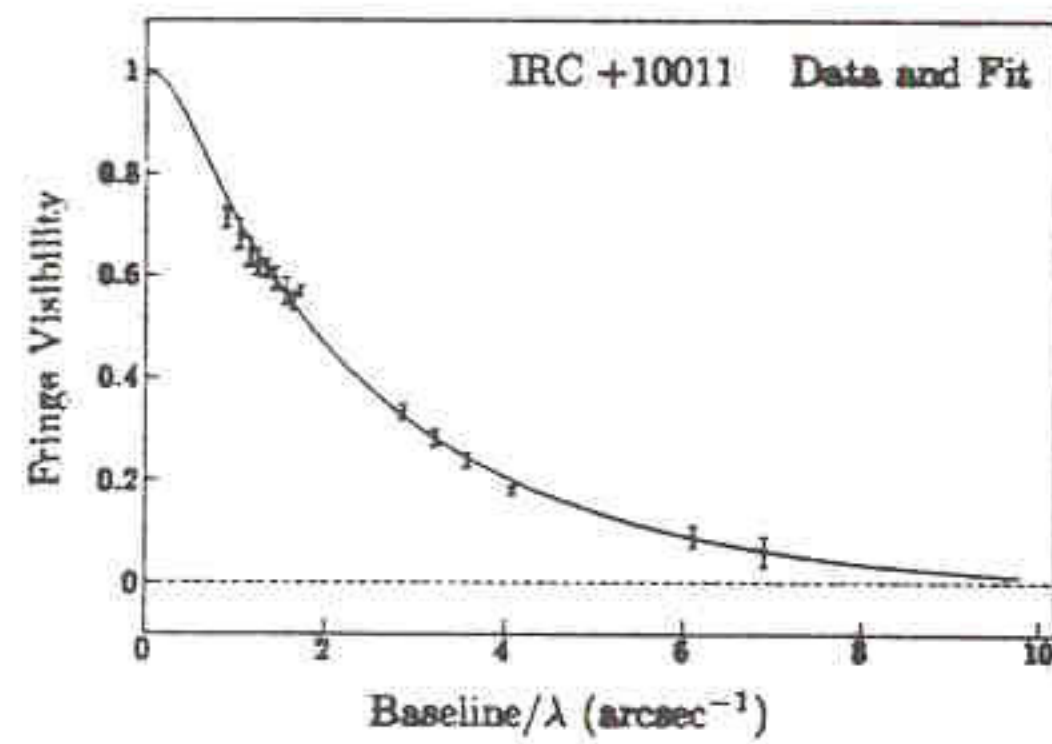
- 1. Spherical Code**
- 2. Temperature calculated self consistently**
- 3. Grain size distribution $\sim a^{-3.5}$**
- 4. Grain types: Silicates, Graphite, (AC, BE)
Amorphous Carbon, or Mixtures**

YIELDS:

- 1. Intensity as a function of impact parameter**
- 2. Spectrum**

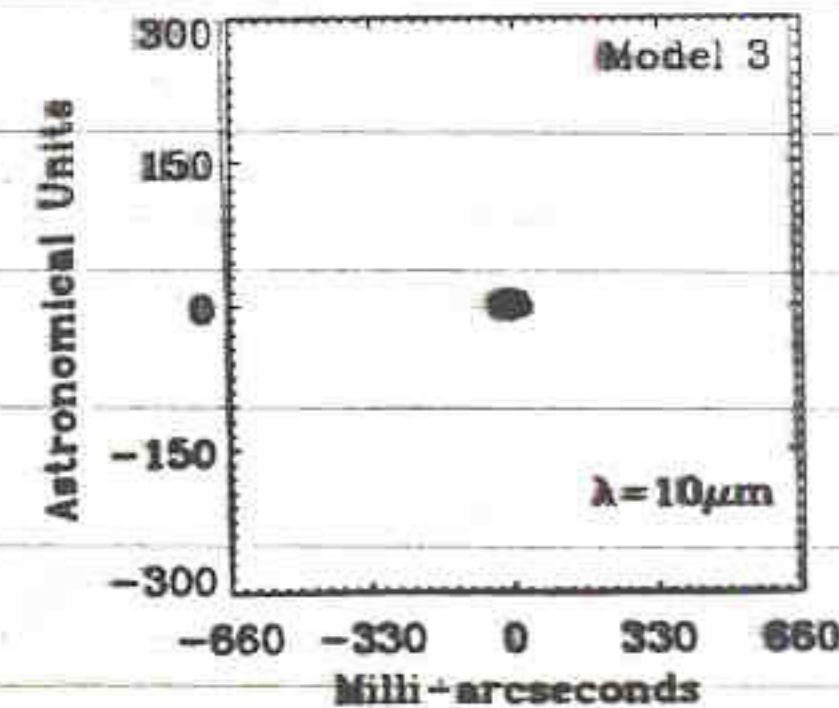
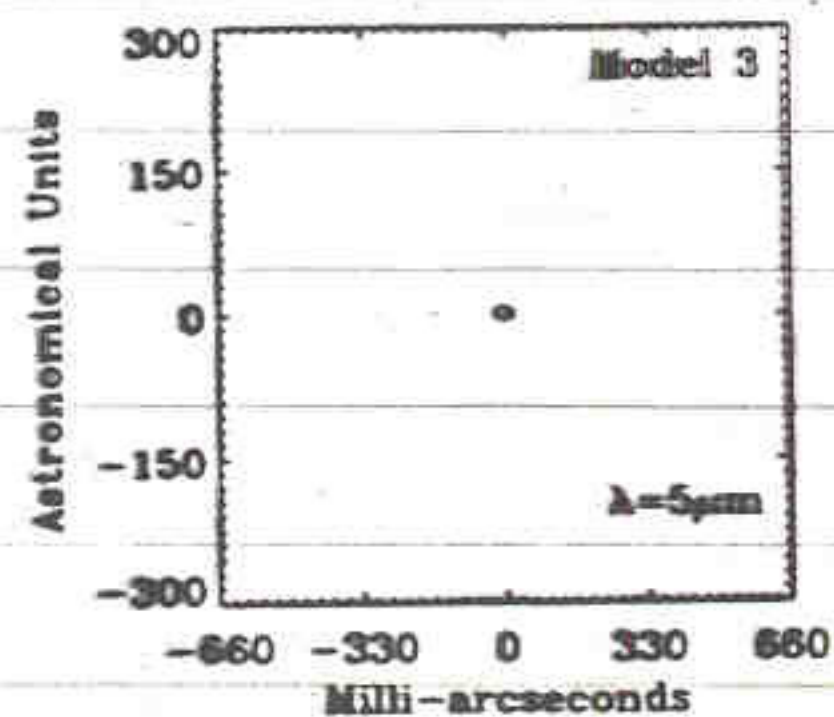
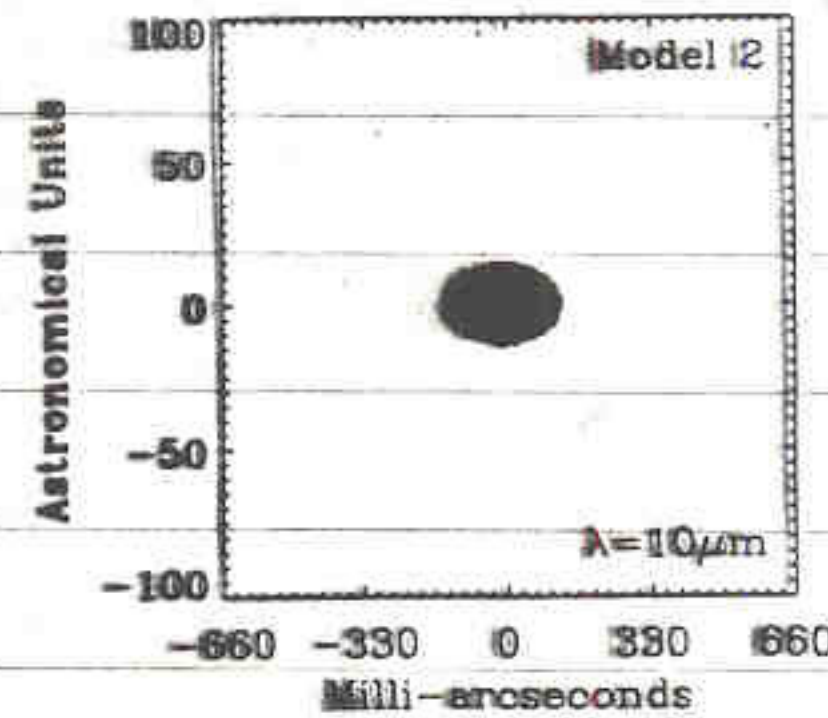
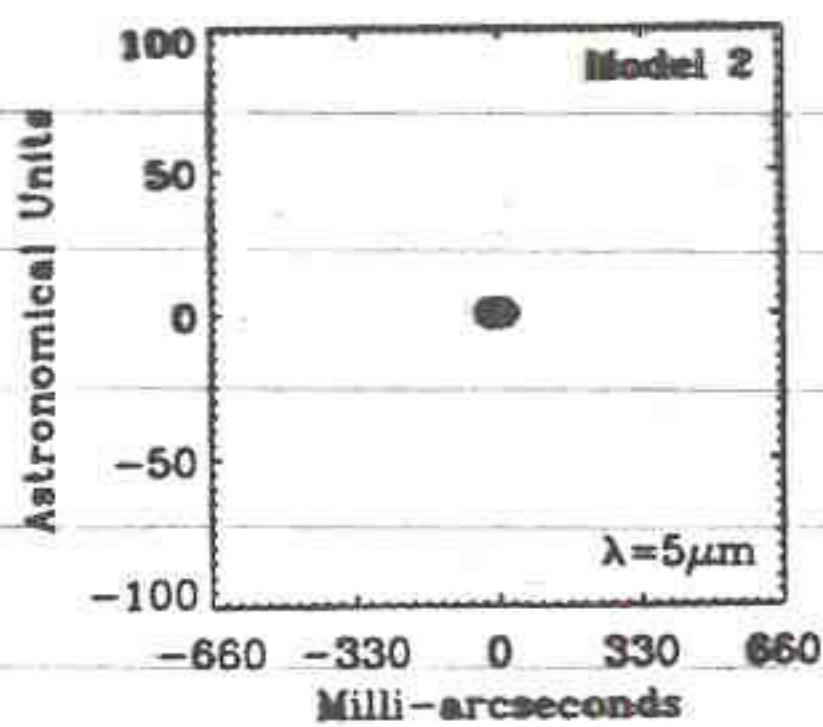
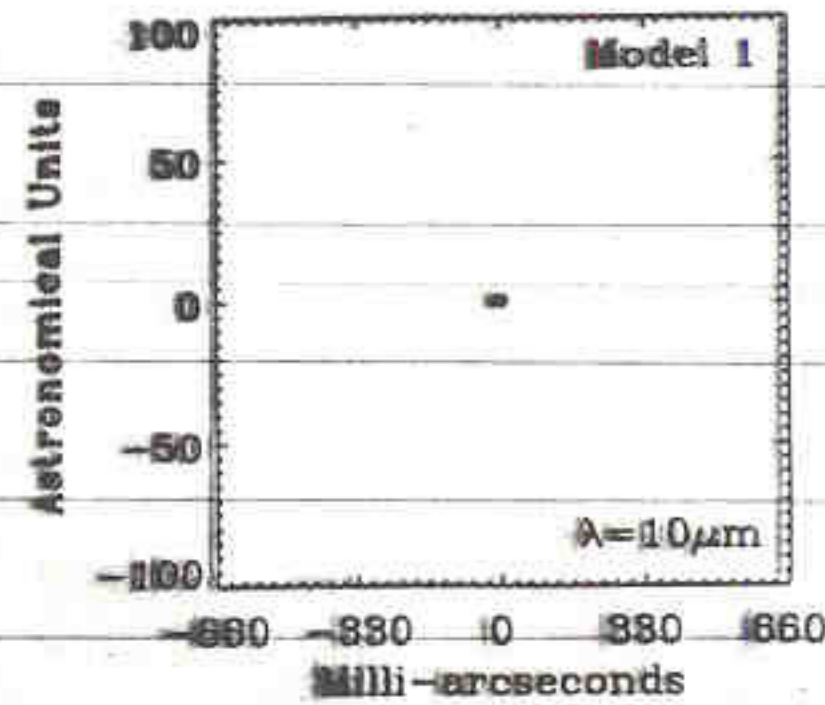
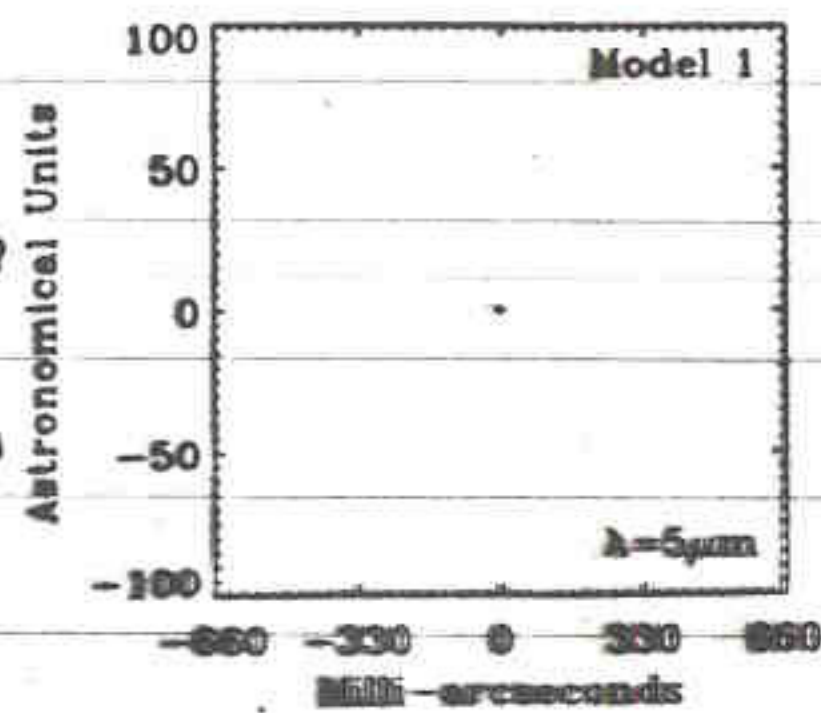
TO COMPARE WITH DATA:

- 1. Compute Visibility from Intensity Distribution**
- 2. Fit model parameters: Inner radius, Optical
depth at 11 microns**
- 3. Constraints are total luminosity and 11 um flux
density**
- 4. Also get mid-IR spectrum but don't explicitly fit
that.**



$$\begin{aligned} \chi^2 &= 33.1 \\ \tau &= 1.75 \\ D &= 500 \text{ parsec} \\ T_* &= 2700 \text{ K} \\ r_* &= 0.0036'' \\ r_{\text{inner}} &= 0.033'' \\ r_{\text{outer}} &= 3'' \\ \rho_{\text{outer}} &= 1.4 \times 10^{-18} \text{ g/cm}^3 \\ \rho &\propto r^{-1.5} \end{aligned}$$

Accretion
Rate:
 $10^{-7} M_{\odot}/yr$
Classical
T Tauri
 $T(r) \propto r^{-3/4}$
(150 pc)



"Flat Spectra"
 $T(r) \propto r^{-1/2}$
(150 pc)
 $10^{-6} M_{\odot}/yr$

FU Ori
 $r^{-3/4}$
(950 pc)
 $10^{-4} M_{\odot}/yr$

Fig. 1. Synthetic thermal images of circumstellar disks at $\lambda = 5 \mu m$ and $\lambda = 10 \mu m$ (logarithmic scale). Model 1 (classical T Tauri star) is displayed in top panels, model 2 (flat infrared spectrum T Tauri star) in middle panels and model 3 (FU Orionis star) in bottom panels. Left panels are images at $5 \mu m$, and right panels are images at $10 \mu m$.

The radial temperature law is then given by $T \propto r^{-q}$, with q in the range $1/2$ (flat infrared SED) to $3/4$ ("classical" accretion disk infrared SED). With this approach and an assumed disk radius of 100 AU, one derives typical disk masses of a few percent of one solar mass, with considerable uncertainty.

3. Synthetic thermal images and visibilities of circumstellar disks

Work presented in this paper is part of a wider effort to obtain synthetic images of T Tauri disks in order to compare them with future observations (Bertout & Bouvier 1988; Malbet et al. 1992; Bouvier et al. 1992; Monin et al.

1993). Earlier studies concentrated on vertical structure and scattering processes in T Tauri disk. Here we focus our attention on the output images and on their transformation to interferometric visibilities.

A first disk model used for computing images is based on the work of Bertout, Basri & Bouvier (1988). The disk is supposed to be flat and has a radial structure derived from Lynden-Bell & Pringle (1974) with temperature law proportional to $r^{-3/4}$. We did not take into account the flux coming from the interaction region between disk and star, since it emits mainly in the ultraviolet and is located very close to the surface of the star. The boundary layer is not resolved except perhaps in the ultraviolet range which is beyond current interferometry. The flux

Table 1. Disk model parameters

	Model 1	Model 2	Model 3
Inner Radius	$1.1 R_*$	$1.1 R_*$	$1.1 R_*$
Outer Radius	50 AU	50 AU	150 AU
Distance	150 pc	150 pc	450 pc
Temperature	$\propto r^{-3/4}$	$\propto r^{-1/2}$	$\propto r^{-3/4}$
Accretion rate	$10^{-7} M_{\odot}/\text{yr}$	$10^{-6} M_{\odot}/\text{yr}$	$10^{-4} M_{\odot}/\text{yr}$

Table 2. Visibilities for 50 m and 100 m baselines

	Model 1		Model 2		Model 3	
Baseline	50 m	100 m	50 m	100 m	50 m	100 m
$\lambda = 0.5 \mu\text{m}$	1.0	1.0	1.00	0.99	0.96	0.87
$\lambda = 1 \mu\text{m}$	1.0	1.0	0.99	0.98	0.96	0.87
$\lambda = 2.2 \mu\text{m}$	0.99	0.98	0.96	0.88	0.94	0.81
$\lambda = 5 \mu\text{m}$	0.99	0.96	0.86	0.77	0.92	0.74
$\lambda = 10 \mu\text{m}$	0.99	0.95	0.66	0.40	0.87	0.65
$\lambda = 20 \mu\text{m}$	0.97	0.90	0.41	0.21	0.82	0.56

Table 3. Disk sizes vs. resolution of a $B = 100$ m interferometer at the 0.9 level

Wavelength	Model 1		Model 2		Model 3		0.08 B/λ
	AU	mas	AU	mas	AU	mas	
$\lambda = 0.5 \mu\text{m}$	—	—	—	—	0.06	0.1	0.08
$\lambda = 1 \mu\text{m}$	—	—	—	—	0.15	0.4	0.16
$\lambda = 2.2 \mu\text{m}$	0.05	0.3	0.07	0.5	0.5	1	0.4
$\lambda = 5 \mu\text{m}$	0.15	1	0.4	3	1.5	3	0.8
$\lambda = 10 \mu\text{m}$	0.4	3	1.5	10	4	9	1.6
$\lambda = 20 \mu\text{m}$	1	7	6	40	10	20	3.3

Table 4. T Tauri accretion disks predicted fluxes compared to VISA expected sensitivity

Wavelength	T Tauri disk fluxes			VISA Sensitivity	
	Model 1	Model 2	Model 3	conservative case	long-term case
0.5 μm	0.13 Jy	0.13 Jy	9.1 Jy	4.2 Jy	21 mJy
1 μm	0.73 Jy	0.83 Jy	15 Jy	1.4 Jy	21 mJy
2.2 μm	1.2 Jy	2.1 Jy	16 Jy	0.4 Jy	8 mJy
5 μm	1.2 Jy	4.7 Jy	14 Jy	0.5 Jy	0.1 Jy
10 μm	1.1 Jy	9.3 Jy	12 Jy	1.6 Jy	0.3 Jy
20 μm	1.0 Jy	19 Jy	9.9 Jy	5.6 Jy	1.1 Jy

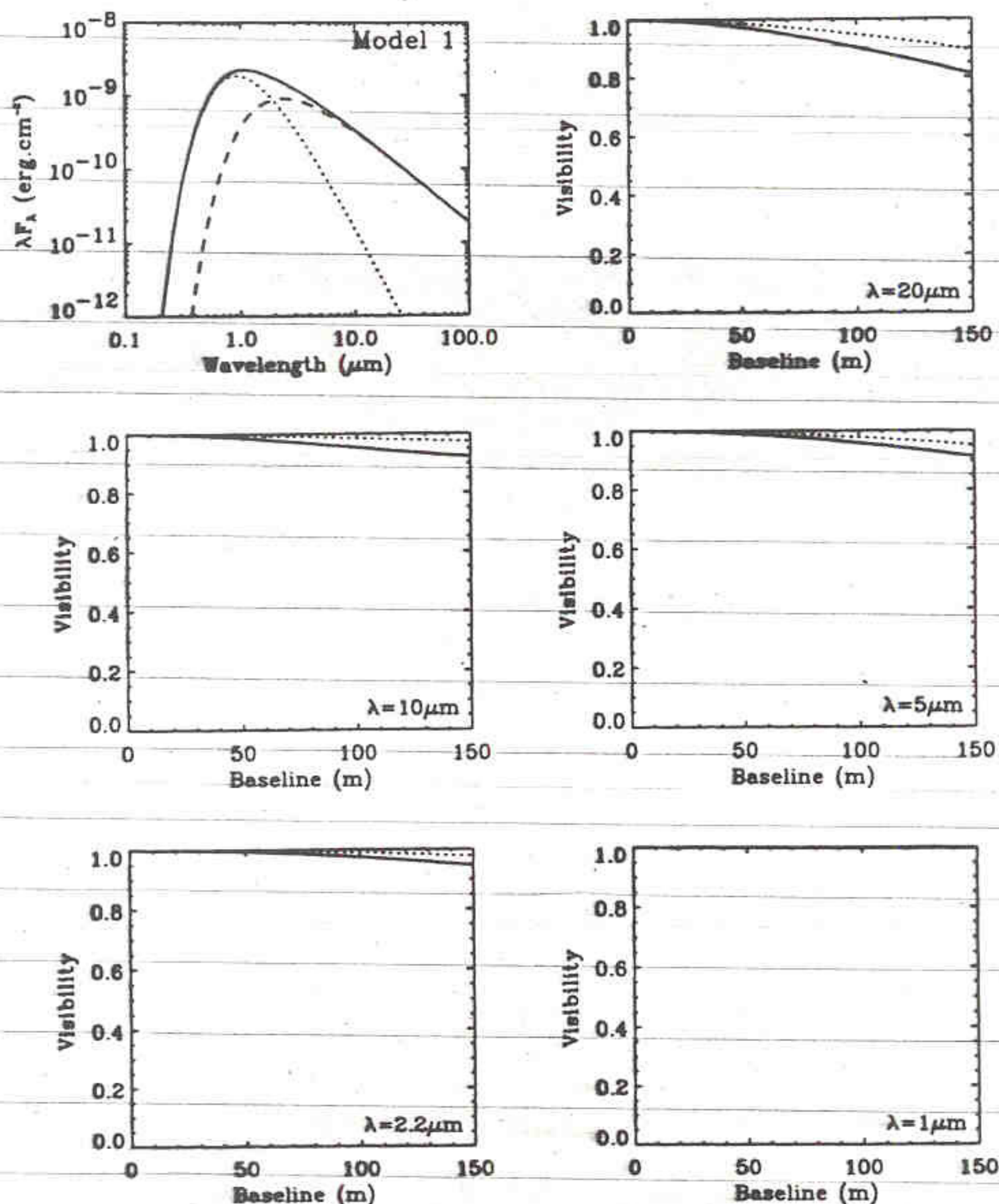


Fig. 2. Interferometric visibilities of a classical T Tauri star (model 1). Top left panel: global spectral energy distribution in solid line, star contribution in dotted line and disk contribution in dashed line. Top right panel: visibility at 20 μm . Middle left panel: visibility at 10 μm . Middle right panel: visibility at 5 μm . Bottom left panel: visibility at 2.2 μm . Bottom right panel: visibility at 1 μm . Solid line corresponds to the major axis of the disk, and dotted line to the minor axis

from the boundary layer is negligible at visible and infrared wavelengths. The effect of shadowing of the inner part of the disk by the star has been taken into account for the central pixel. The disk is supposed to be optically thick even in the outer part of the disk. The star is an unresolved black body.

A second model used to compute images assumes the disk has a temperature radial distribution proportional to $r^{-1/2}$. The total flux from the disk is parameterized by the accretion rate which is needed to get the same total flux with a classical disk model.

Most of the difficulty involved in building an image comes from the linear sampling on the sky. The original

model sampling is polar, linear in angle from the star, and logarithmic in radius. We have to transform this in a square linear sampling on the sky without losing or creating any flux. We do this by building a linear regular grid on the sky with a cell size such that several points from the original grid are found inside this cell. Then the solid angle of the original cells is computed in order to conserve the flux. The computation leads to a data cube with two spatial dimensions and a spectral dimension. The spectral energy distribution is calculated with the original sampling and with the regular grid, and we check that the two spectral distributions are identical. The star flux contribution is added in the central pixel.

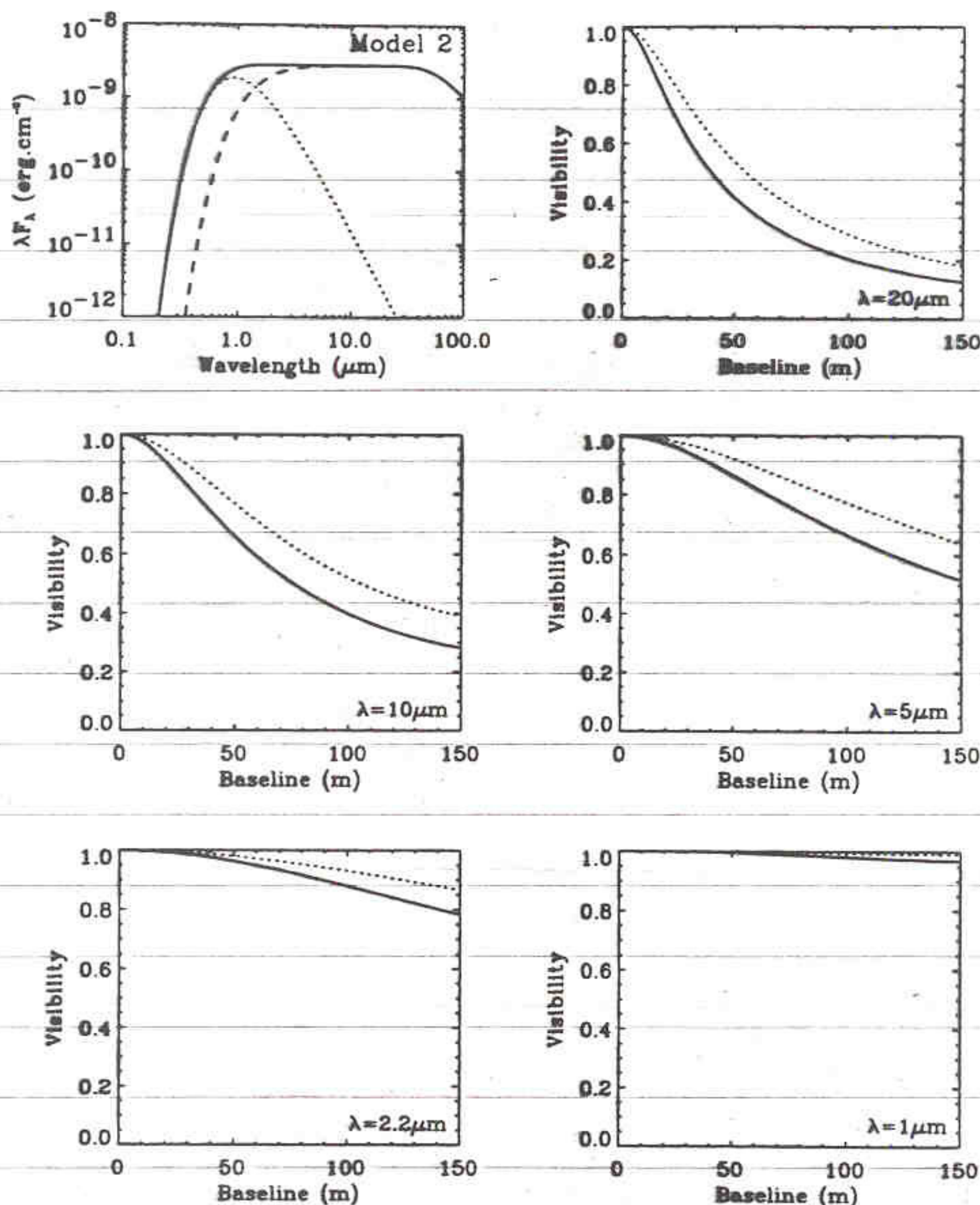


Fig. 3. Interferometric visibilities of a T Tauri star with a flat infrared spectral energy distribution (Model 2). Top left panel: global spectral energy distribution in solid line, star contribution in dotted line and disk contribution in dashed line. Top right panel: visibility at 20 μm . Middle left panel: visibility at 10 μm . Middle right panel: visibility at 5 μm . Bottom left panel: visibility at 2.2 μm . Bottom right panel: visibility at 1 μm . Solid line corresponds to the major axis of the disk, and dotted line to the minor axis

We simulated 3 different models of circumstellar disks around the same star. The star has radius $3 R_{\odot}$, mass $1 M_{\odot}$ and 4000 K effective temperature. A 45° disk inclination is assumed.

- Model 1 is a “classical” accretion disk with $10^{-7} M_{\odot}/\text{yr}$ accretion rate located in the Taurus-Auriga cloud at 150 pc.
- Model 2 is a disk of same luminosity as Model 1 with a flat infrared spectrum located at the same distance as Model 1.

– Model 3 is a FU Orionis disk located in the Orion molecular cloud located at 450 pc with a $10^{-4} M_{\odot}/\text{yr}$ accretion rate.

Disk parameters used in these models are summarized in Table 1. Images obtained at 5 μm and 10 μm are displayed in Fig. 1. The x -axis gives the spatial scale on the sky in milli-arcseconds and the y -axis the absolute spatial scale in Astronomical Units. The emergent spectral energy distributions are presented for each model respectively in the top left panel of Figs. 2-4.

In order to obtain 2-D visibilities, we Fourier transformed the synthetic images. We extracted 2 different

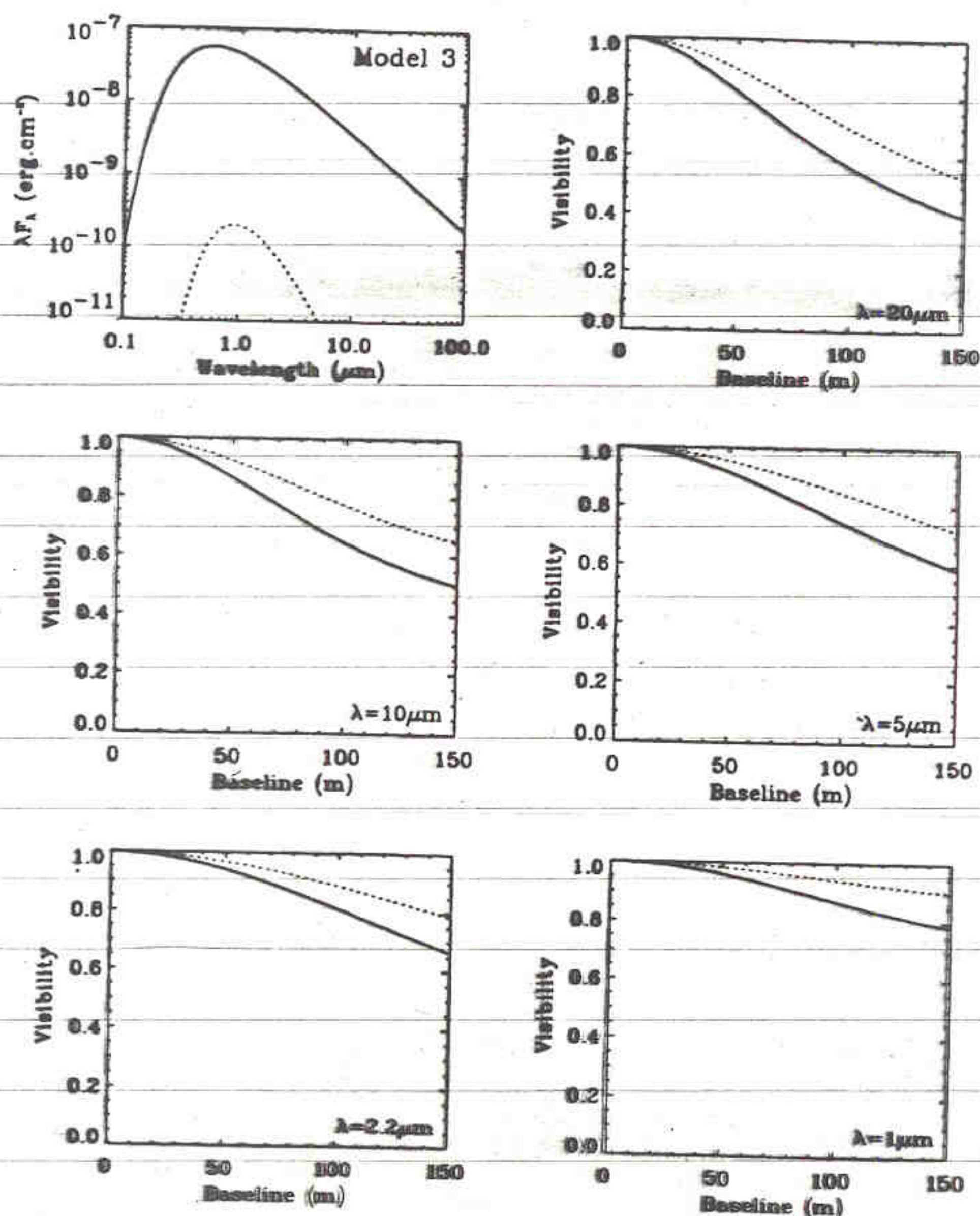


Fig. 4. Interferometric visibilities of a FU Orionis star (Model 3). Top left panel: global spectral energy distribution in solid line, star contribution in dotted line and disk contribution in dashed line. Top right panel: visibility at 20 μm . Middle left panel: visibility at 10 μm . Middle right panel: visibility at 5 μm . Bottom left panel: visibility at 2.2 μm . Bottom right panel: visibility at 1 μm . Solid line corresponds to the major axis of the disk, and dotted line to the minor axis

baselines corresponding to the major and minor axis of the projected disk to provide the minimum and maximum visibility levels due to disk inclination. Interferometric visibilities obtained at 1 μm , 2.2 μm , 5 μm , 10 μm and 20 μm are presented respectively in Figs. 2-4 for each model. The x-axis gives the projected baseline and the y-axis the normalized intensity. Values of visibilities corresponding to the disk major axis are given in Table 2 for projected baselines of 50 m and 100 m. We did not include visibilities at 0.5 μm since spectral energy distributions show that at this wavelength the star flux is dominant and therefore the disk is not resolved.

4. Discussion

4.1. Dynamic range issues

One of the main problems for detecting circumstellar disks by classical imaging techniques is usually the contrast in intensity between the star and the disk. How large is this problem for visibilities? The visibility of an unresolved object is a constant equal to one. An object is resolved if one can detect a slight decrease in the visibility curve. The diameter of a T Tauri star at 150 pc is 0.1 mas. The resolution of a 100-m baseline interferometer at $\lambda = 0.5 \mu\text{m}$ is 1 mas. Therefore the star is always unresolved and the contribution to the visibility is a fixed level

corresponding basically to the flux ratio of the star compared to the total flux of the T Tauri system. This ratio at different wavelengths is given by the SEDs where we can compute contributions from the star and from the disk. The position of line crossings gives the wavelength where the star and the disk fluxes are similar: at about $\lambda = 2 \mu\text{m}$ for Model 1 and at about $\lambda = 1.4 \mu\text{m}$ for Model 2. The stellar flux is completely embedded in Model 3. Therefore there is no dynamic range problem between the respective disk and star fluxes at wavelengths greater than $2 \mu\text{m}$.

4.2. Resolution issues

In order to estimate at which wavelength one can start detecting circumstellar disk, one needs to know the accuracy of the visibility measurements. Thanks to careful calibration of the null spatial frequency, the precision of current interferometers is of order 1–5% for the visibility curves (cf. Pan et al. 1990 and Mozurkewich et al. 1991 for *Mark III* stellar interferometer; Condé du Foresto 1992 for *FLUOR* interferometer). From values reported in Table 2, T Tauri disk thermal emission is barely resolved for wavelengths shorter than $2.2 \mu\text{m}$ with a 100-m baseline in Model 1 and Model 2. However for Models 2 and 3, the detection of disk thermal emission is well within the range of optical interferometers at wavelengths longer than $1 \mu\text{m}$.

Concerning the disk radial distribution of intensity, Figs. 2–4 show that the longer the wavelength, the better T Tauri disks are resolved. The radial distribution of intensity at different wavelengths is displayed in Fig. 5 for Model 1, 2 and 3 in normalized units for the intensity and in milli-arcseconds for the distance to the star. The dotted lines represent the radial distribution of temperature in normalized units. The shapes of the solid curves can be separated into two asymptotic regimes. The first one corresponds to the Wien regime (inner radii) and the second one to the Rayleigh-Jeans regime (outer radii). The transition occurs at the maximum of the black-body emission when $\lambda T \approx 3000 \mu\text{m K}$. These transitions are marked by diamonds on the curves. The distribution of intensity is proportional to the distribution of temperature in the inner disk and decreases exponentially in the outer part of the disk. In the following we will call “disk size” the radius where the transition occurs.

It is useful to make a connection between the disk size and the required interferometric resolution. A simple calculation shows that an interferometer of baseline B can resolve at the 0.9 level a Gaussian disk of radius at half maximum given by the relation

$$R_d \geq 0.08 \frac{\lambda}{B}. \quad (1)$$

This criterion is not strictly valid for computed circumstellar disk models, but gives a useful first approximation of the needed resolution. Since the distribution of temperature is usually proportional to R^{-q} with q ranging

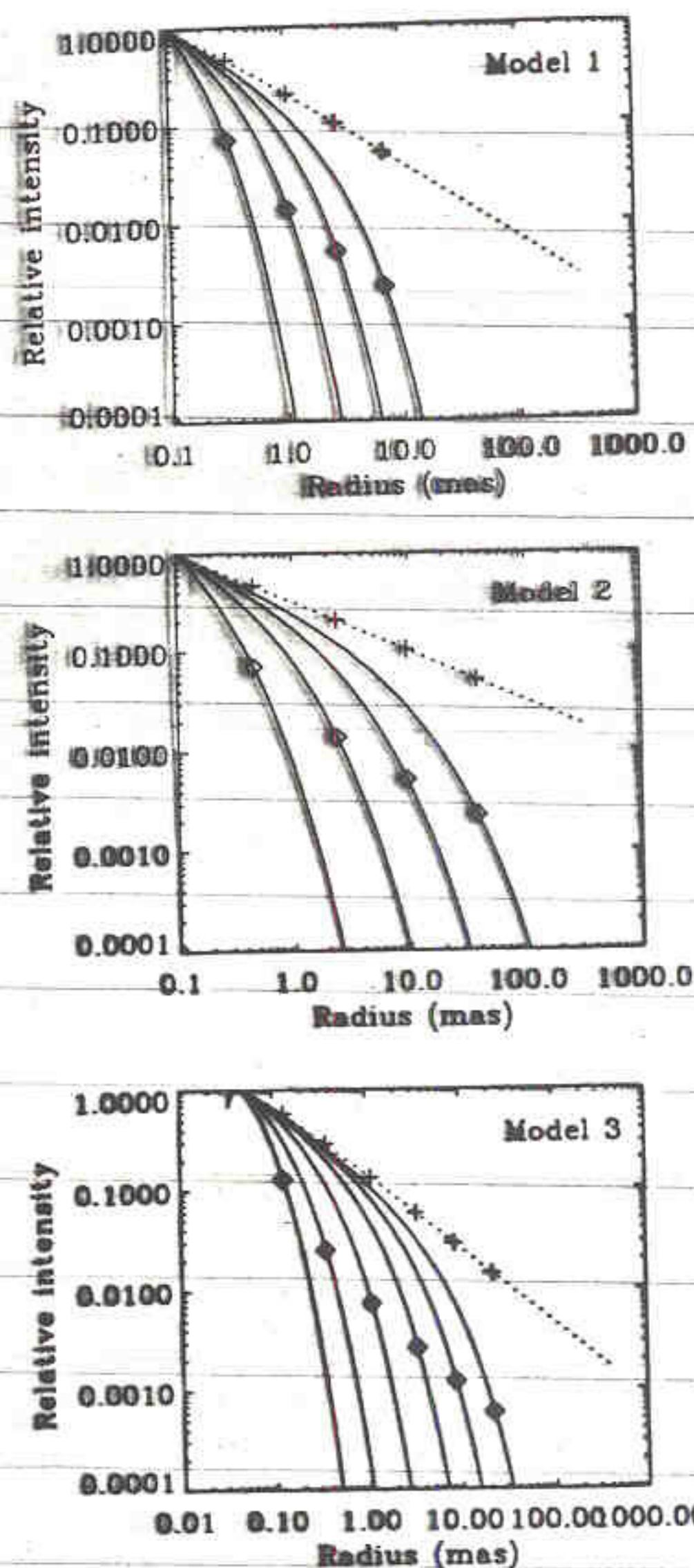
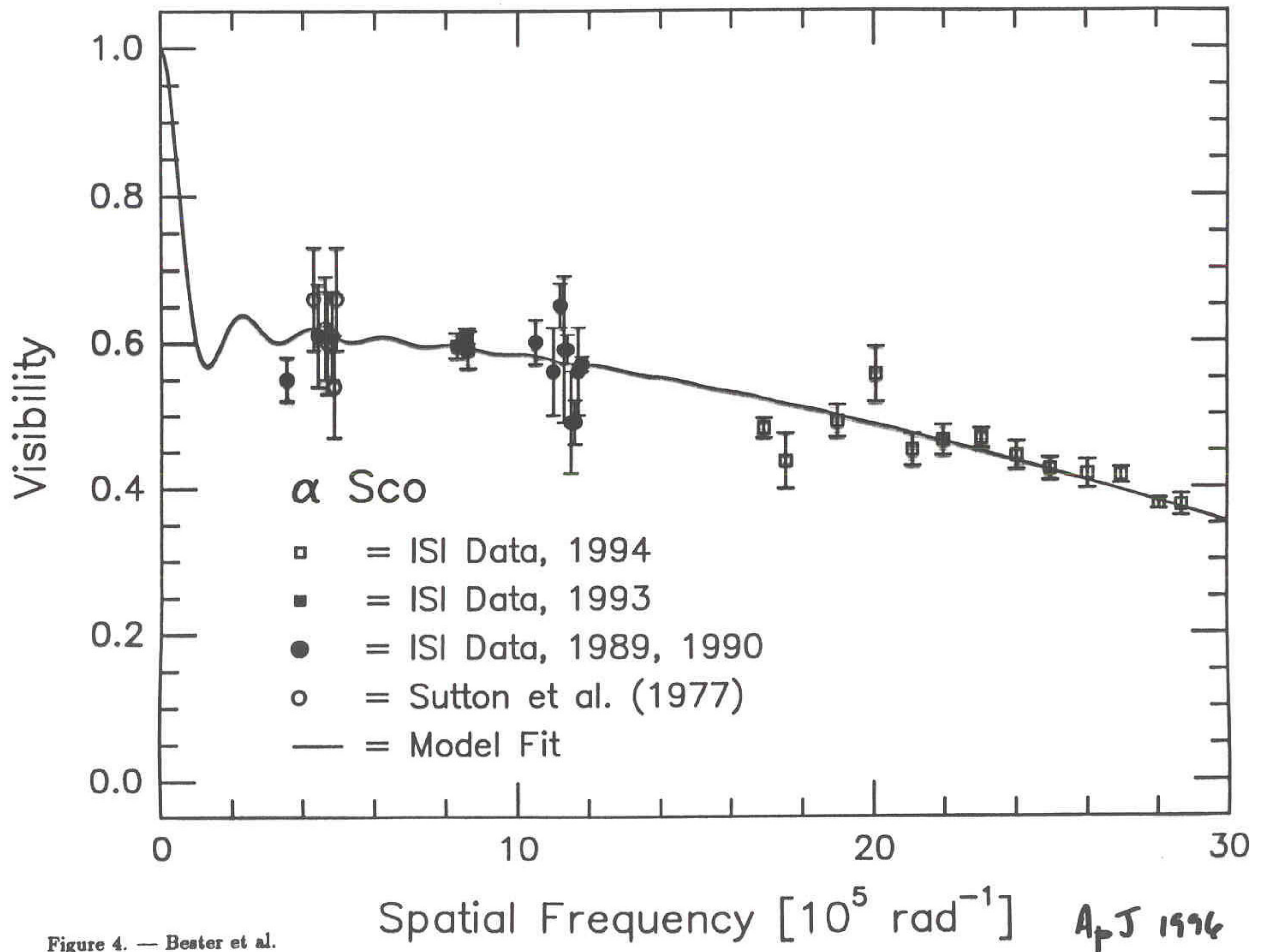


Fig. 5. Radial distribution of intensity in the disk of a classical T Tauri star (Model 1, top), a T Tauri star with a flat infrared spectral energy distribution (Model 2, middle) and a FU Orionis star (Model 3, bottom). Solid lines from right to left: radial distributions of intensity at $\lambda = 20 \mu\text{m}$, $\lambda = 10 \mu\text{m}$, $\lambda = 5 \mu\text{m}$, $\lambda = 2.2 \mu\text{m}$, $\lambda = 1 \mu\text{m}$ (Model 3 only) and $\lambda = 0.5 \mu\text{m}$ (Model 3 only) normalized to unity at the inner radius of the disk. Diamond and plus marks correspond to the transition between the Wien and Rayleigh-Jeans regimes. Dotted line: radial distribution of temperature, normalized to unity at the inner radius of the disk.

between 0.5 and 0.75 (cf. Sect. 2), the exponential behavior of the distribution of intensity is smoother than a Gaussian (e^{-r^2} compared to e^{-r}) and the resolution criterion is somewhat pessimistic for circumstellar disk models. Table 3 gives the corresponding size of the disk (defined by the size of transition zone) at $0.5 \mu\text{m}$, $1 \mu\text{m}$, $2.2 \mu\text{m}$, $5 \mu\text{m}$, $10 \mu\text{m}$ and $20 \mu\text{m}$ for the three models and the corresponding resolution of a 100-m baseline interferometer at the 0.9 level (cf. Eq. (1)). The resolution is marginal

$\theta_{11} = 44 \text{ mas}$



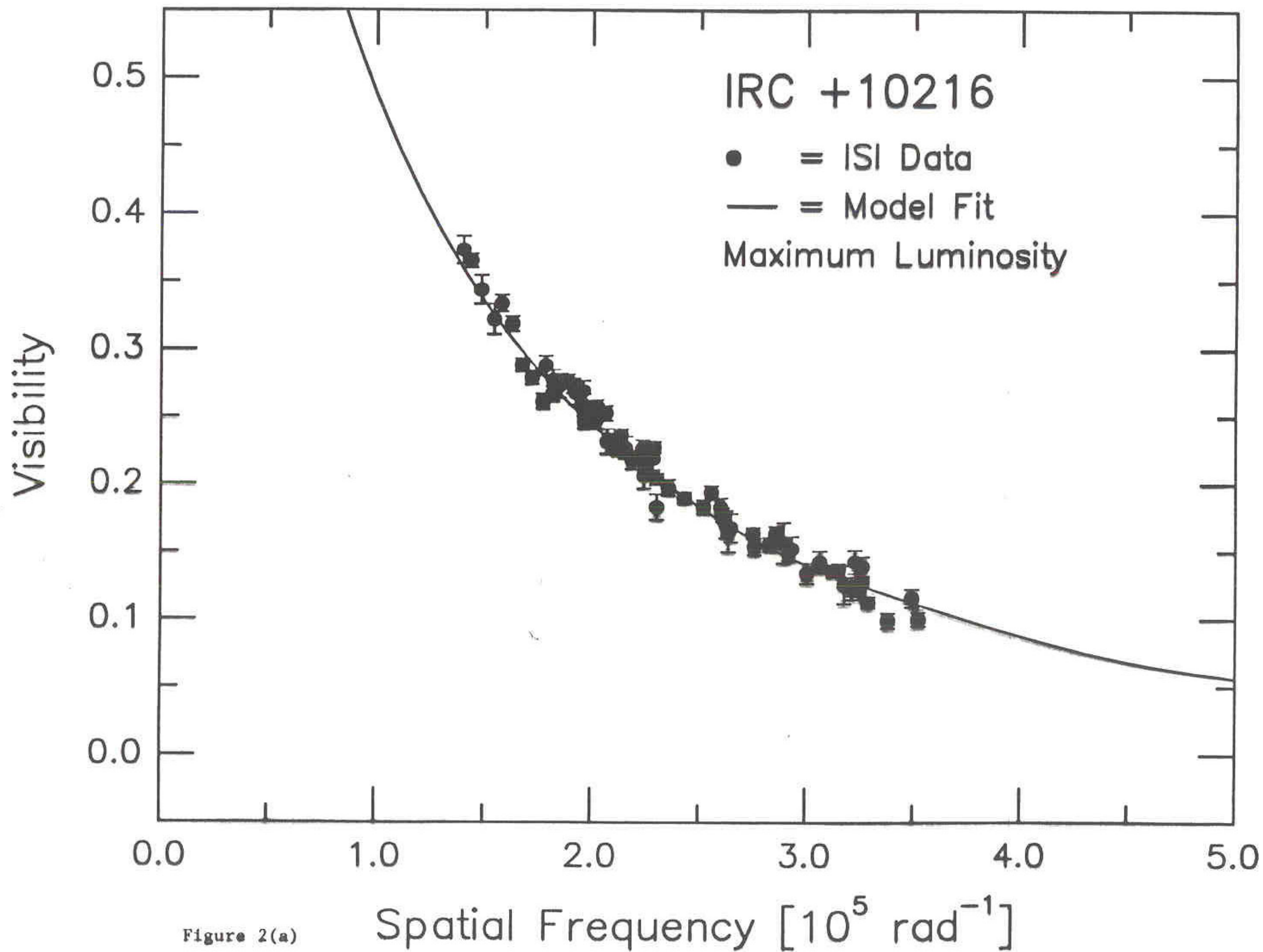


Figure 2(a)

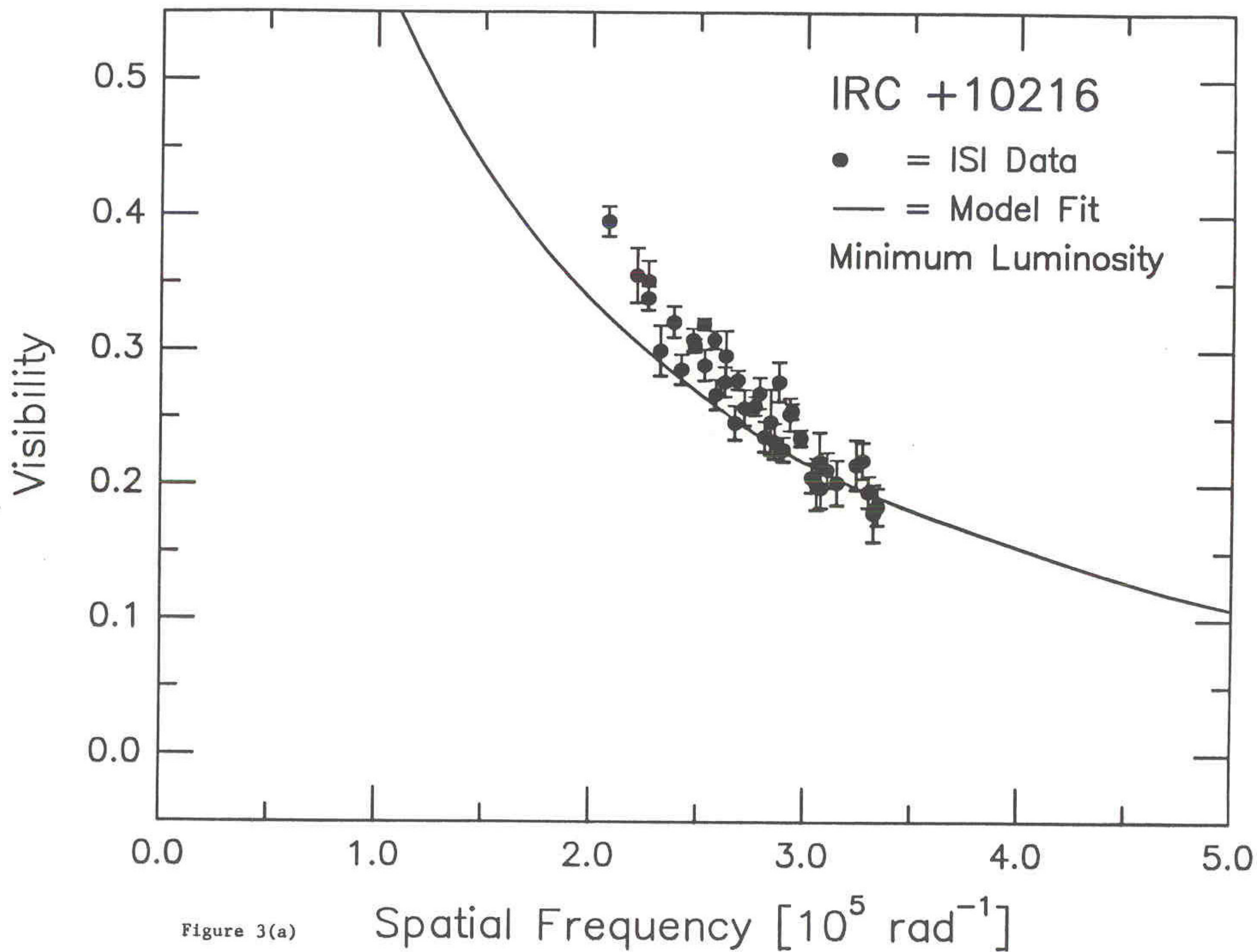
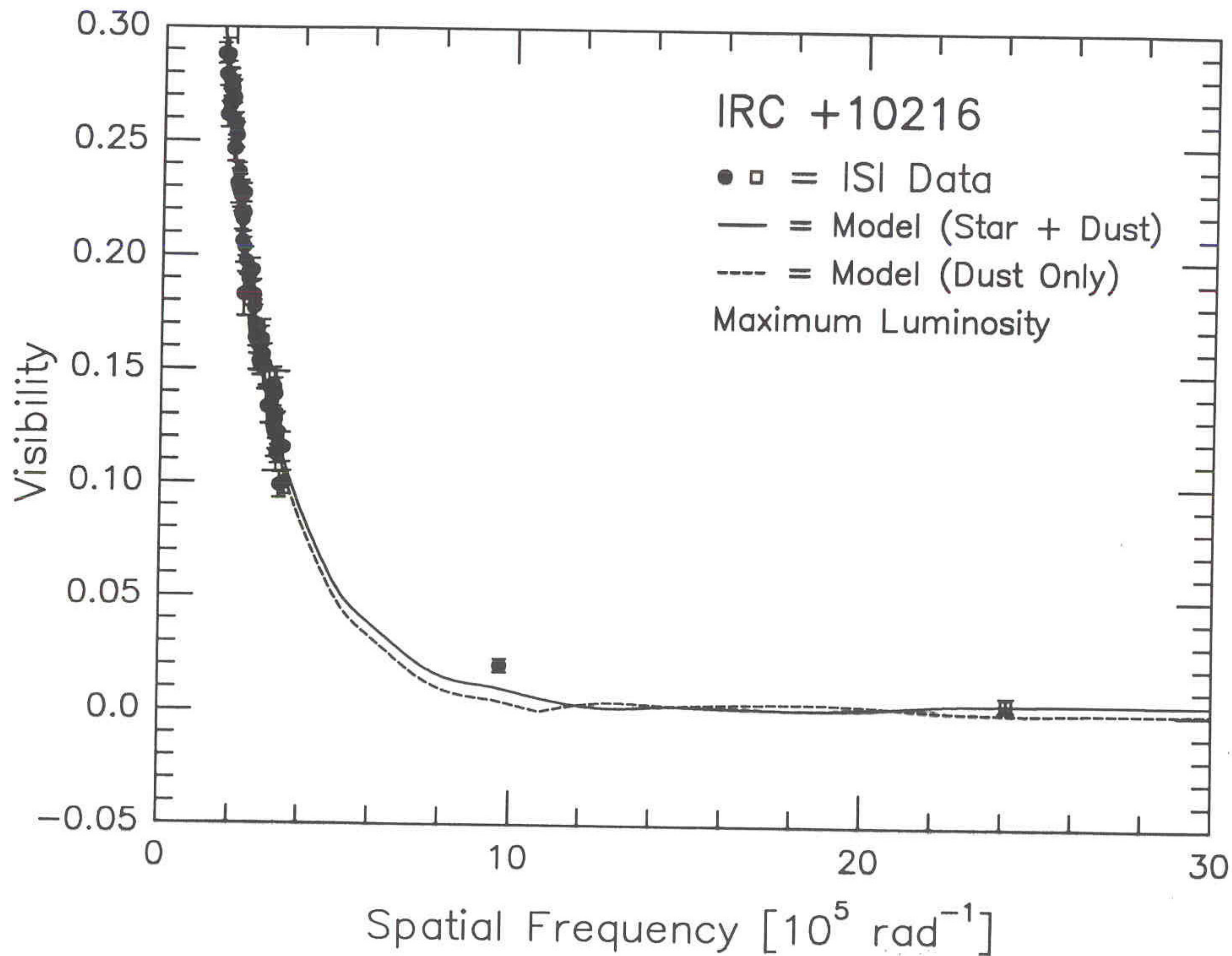


Figure 3(a)



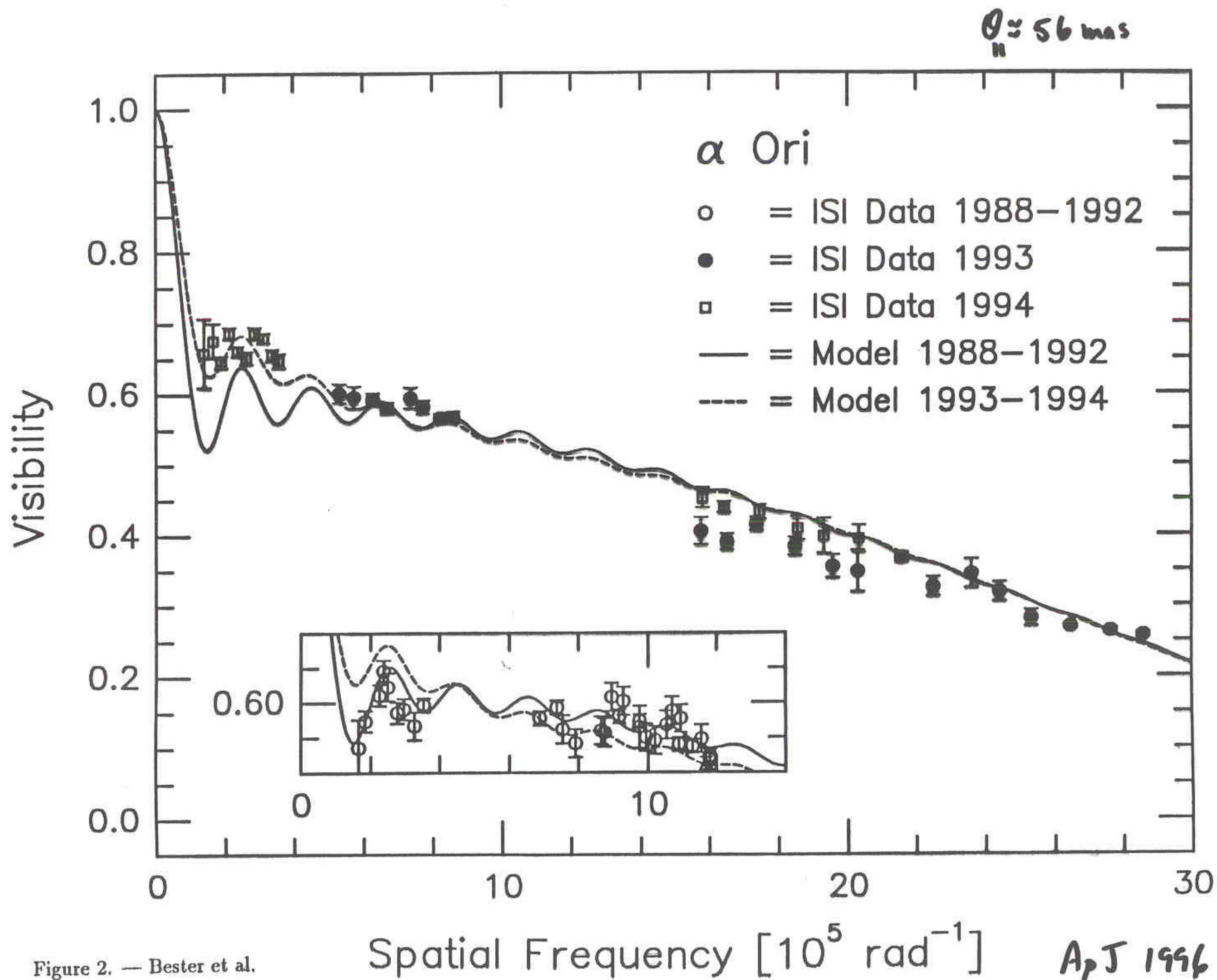


Figure 2. — Bester et al.

A, J 1996

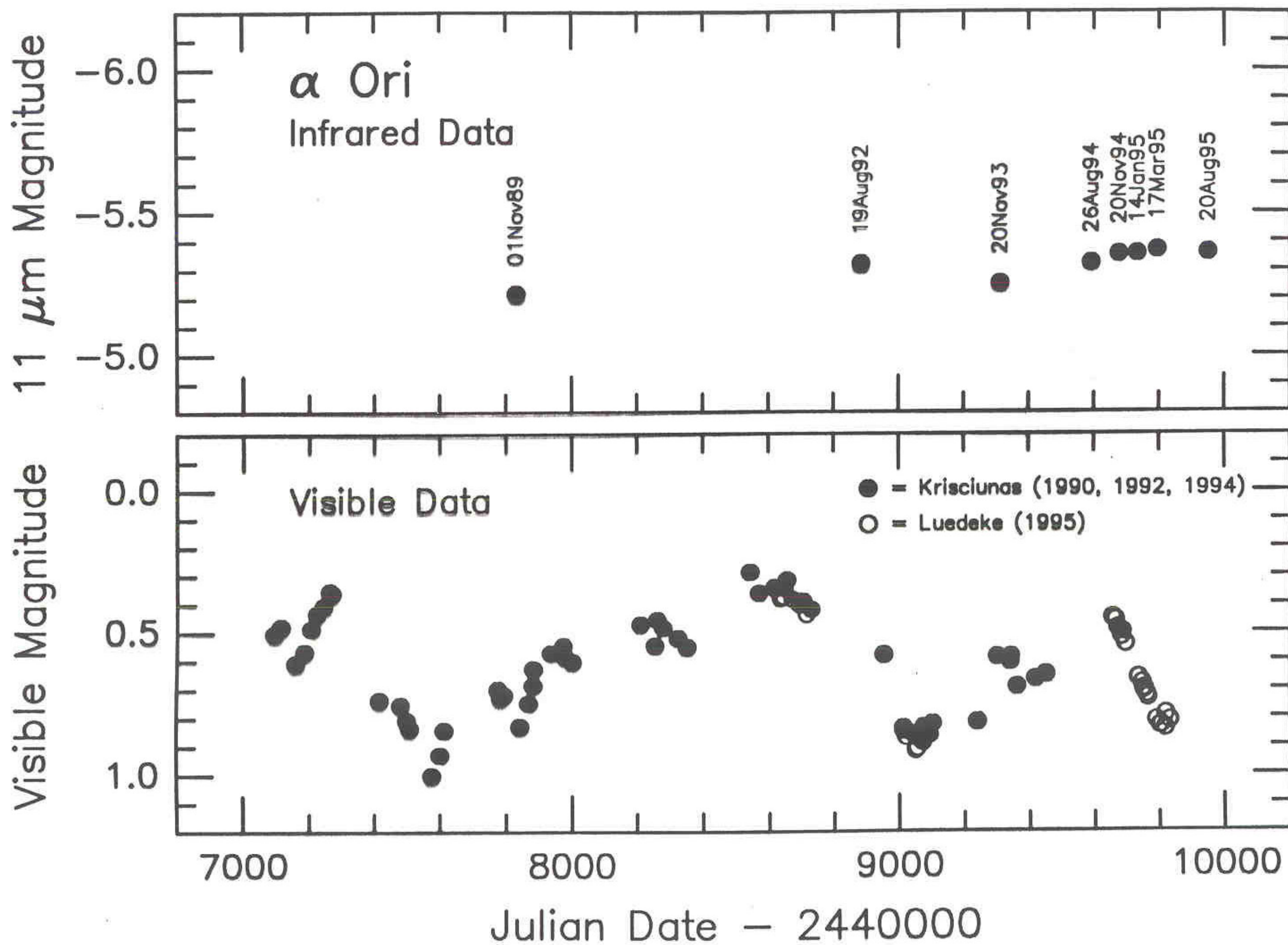
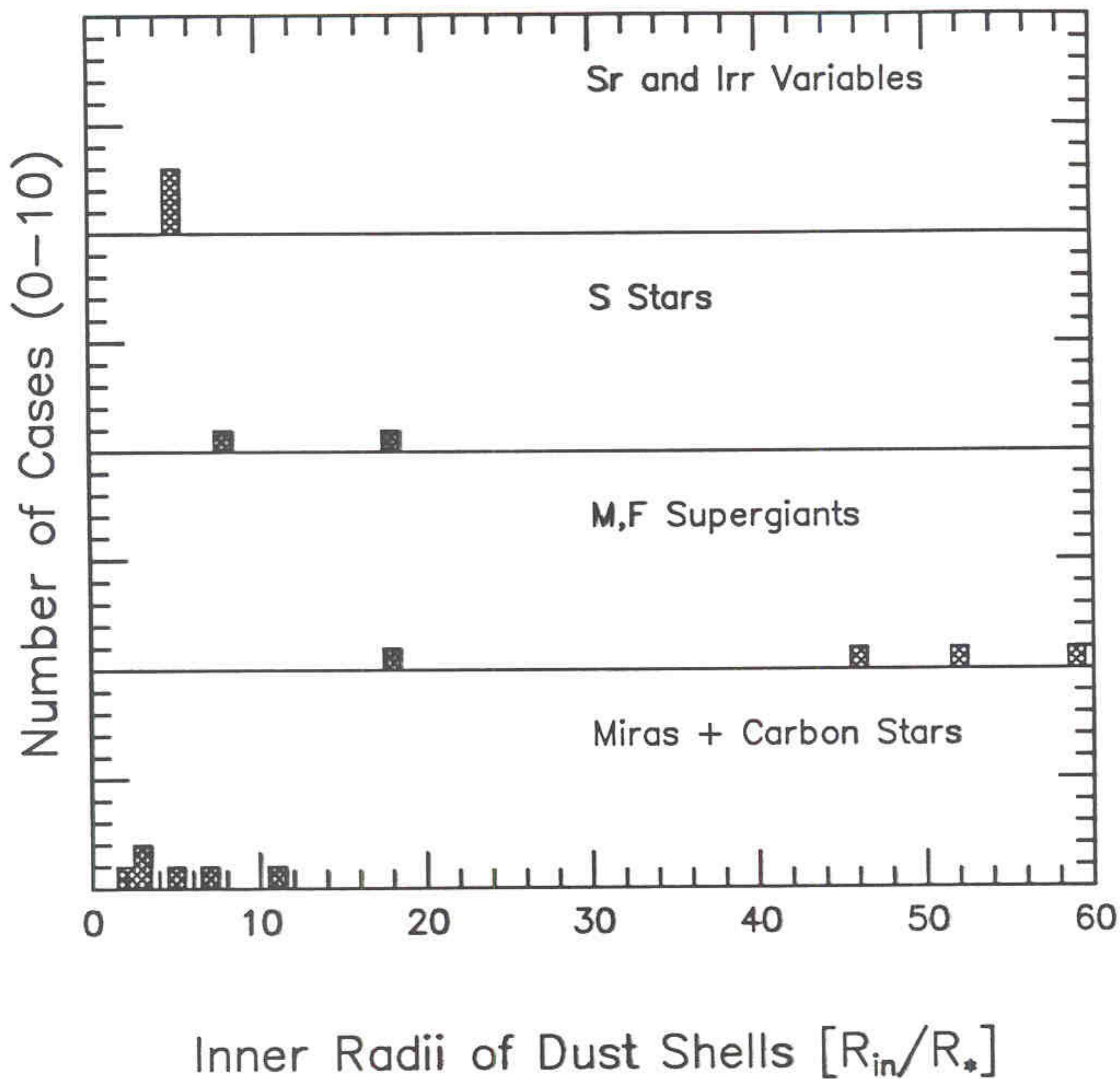


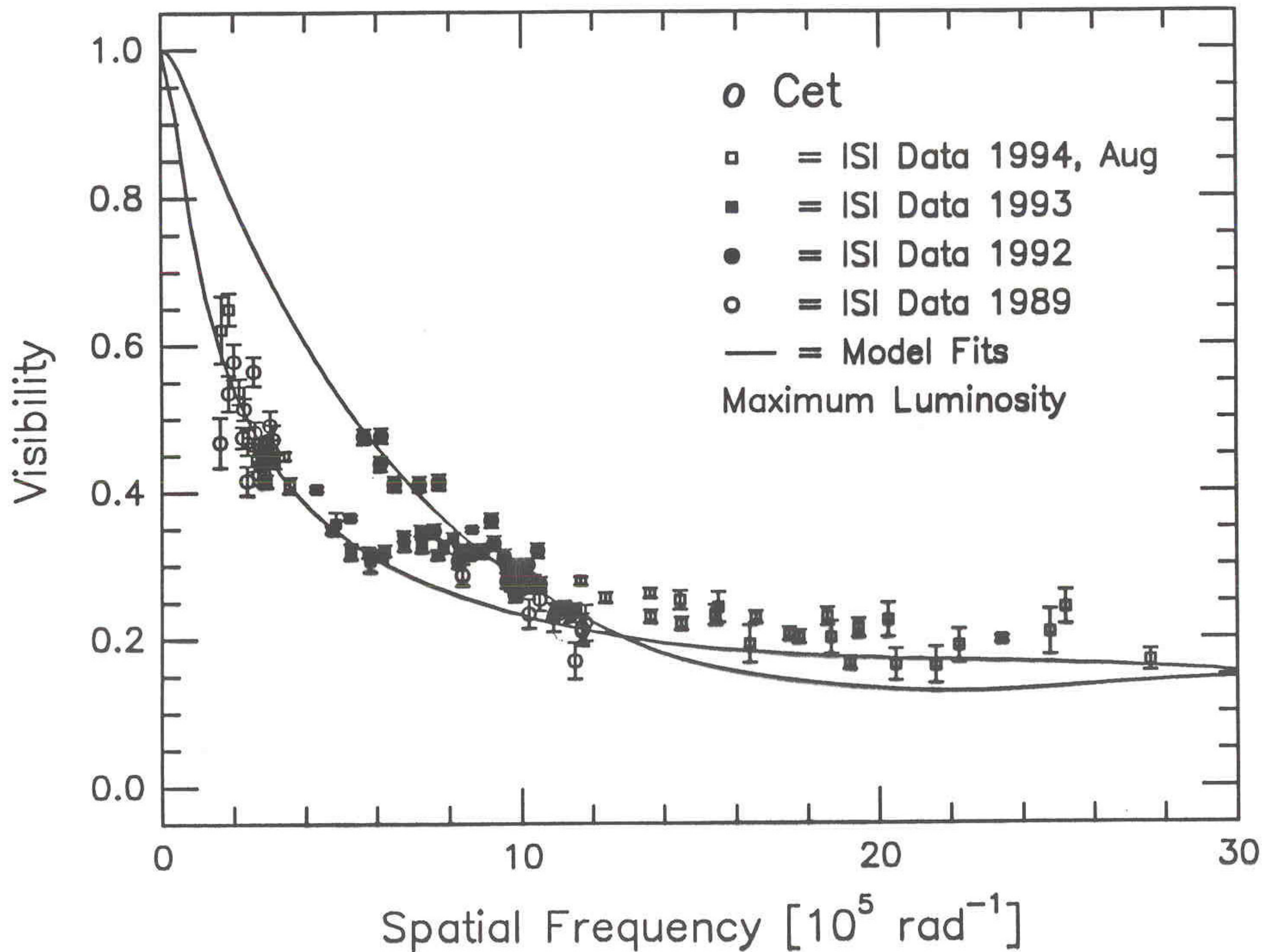
Figure 1. — Bester et al.



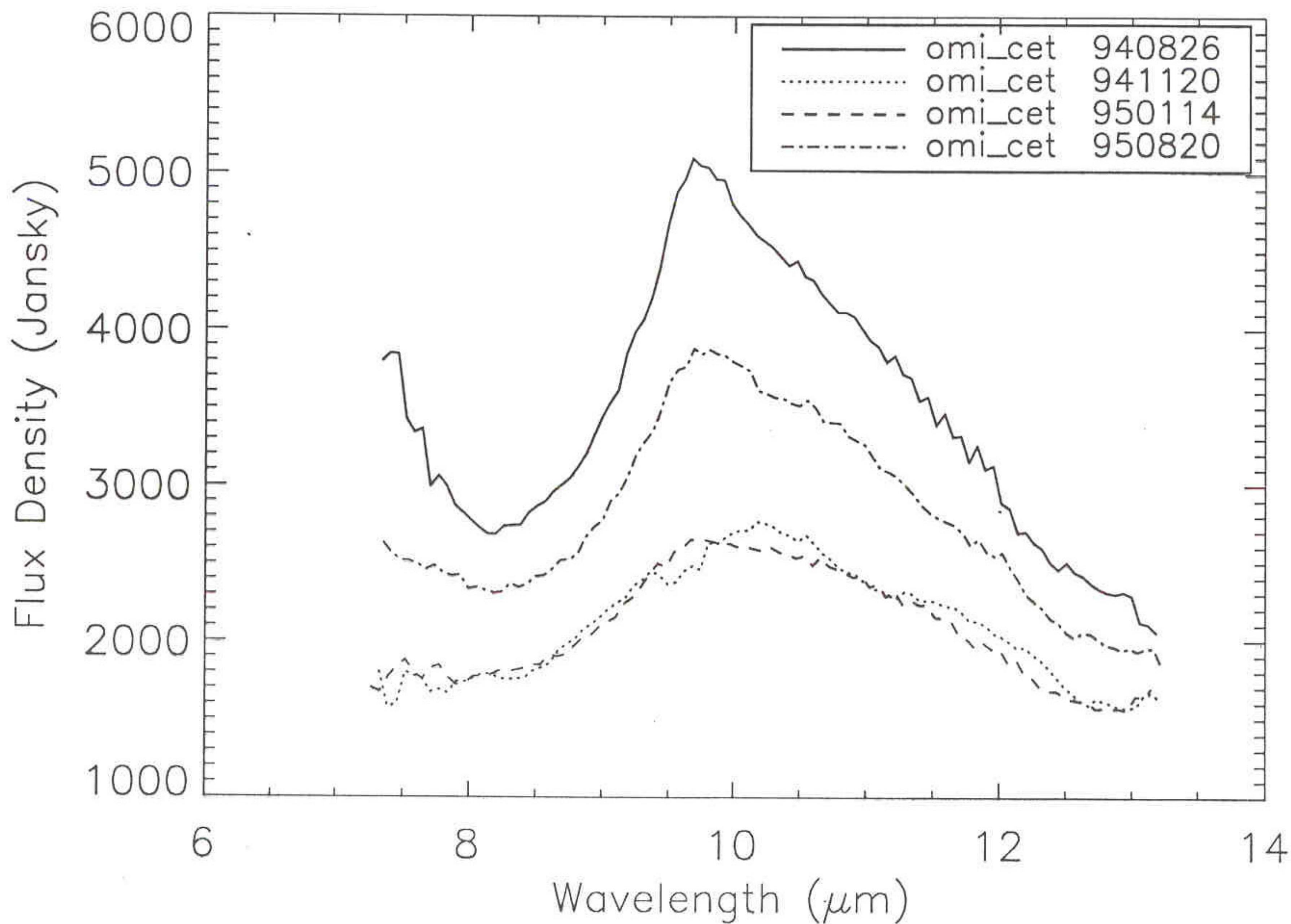
BESTER & DANCHU
(1995)

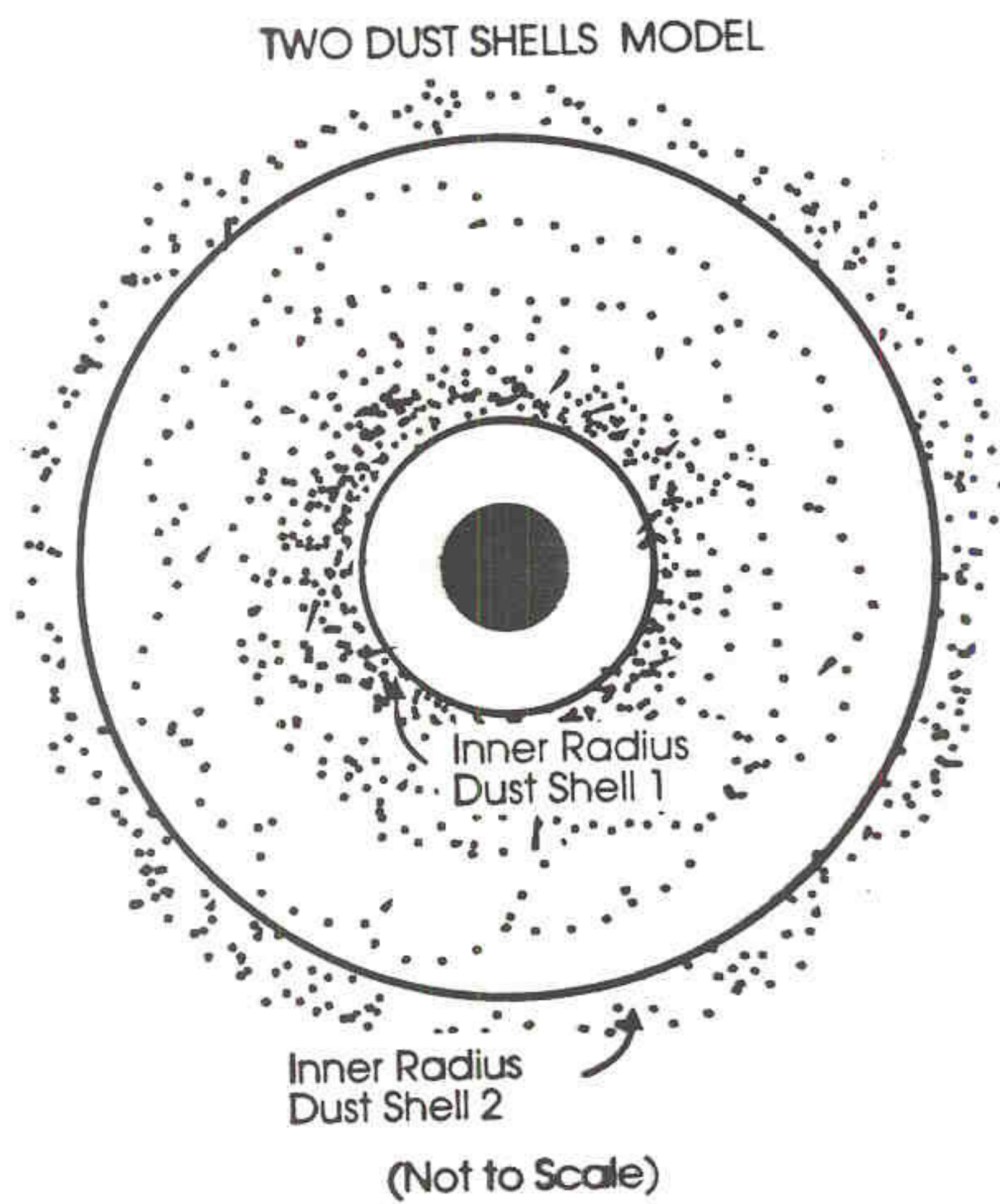
ASTRO. & SPACE SCIENCES.

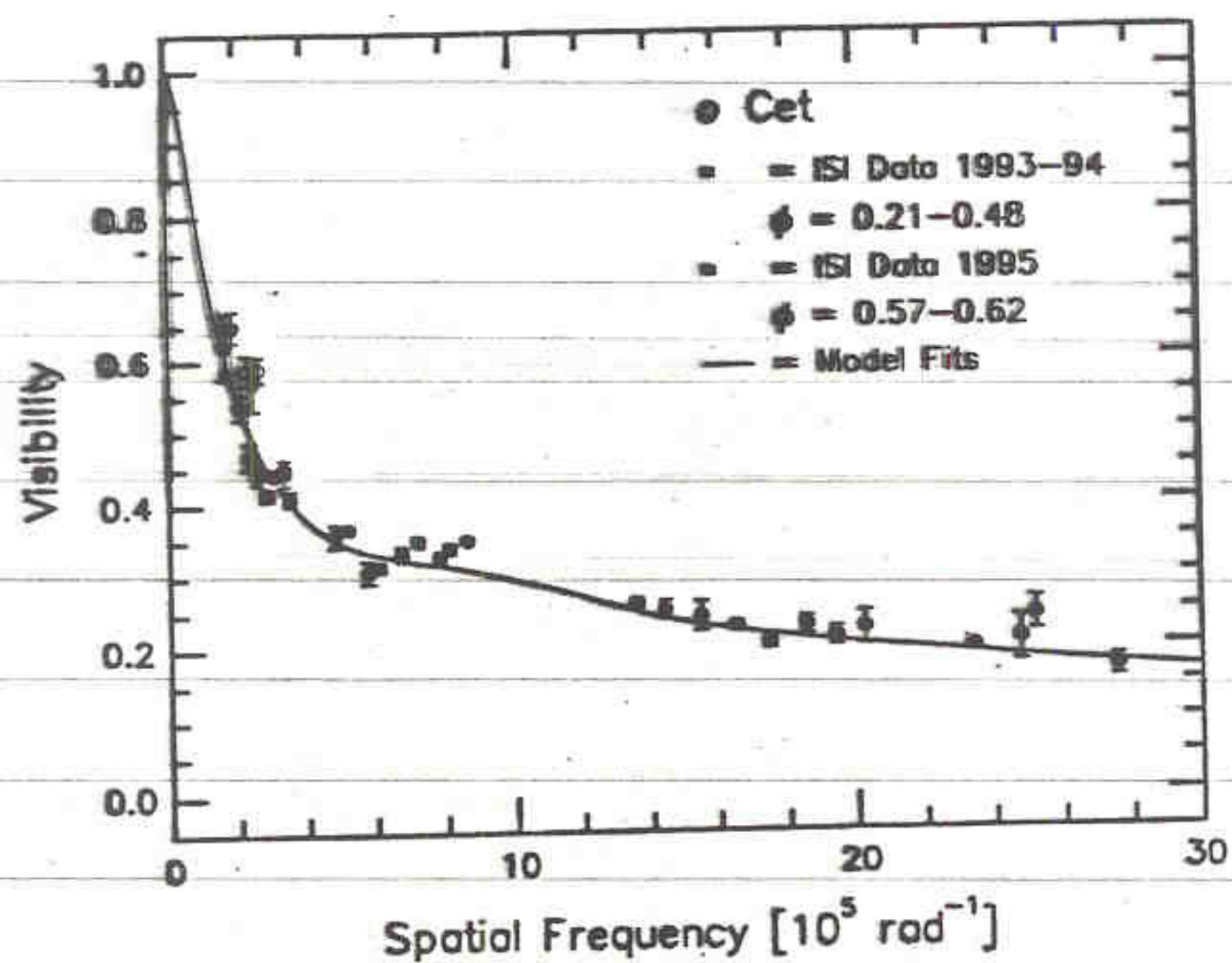
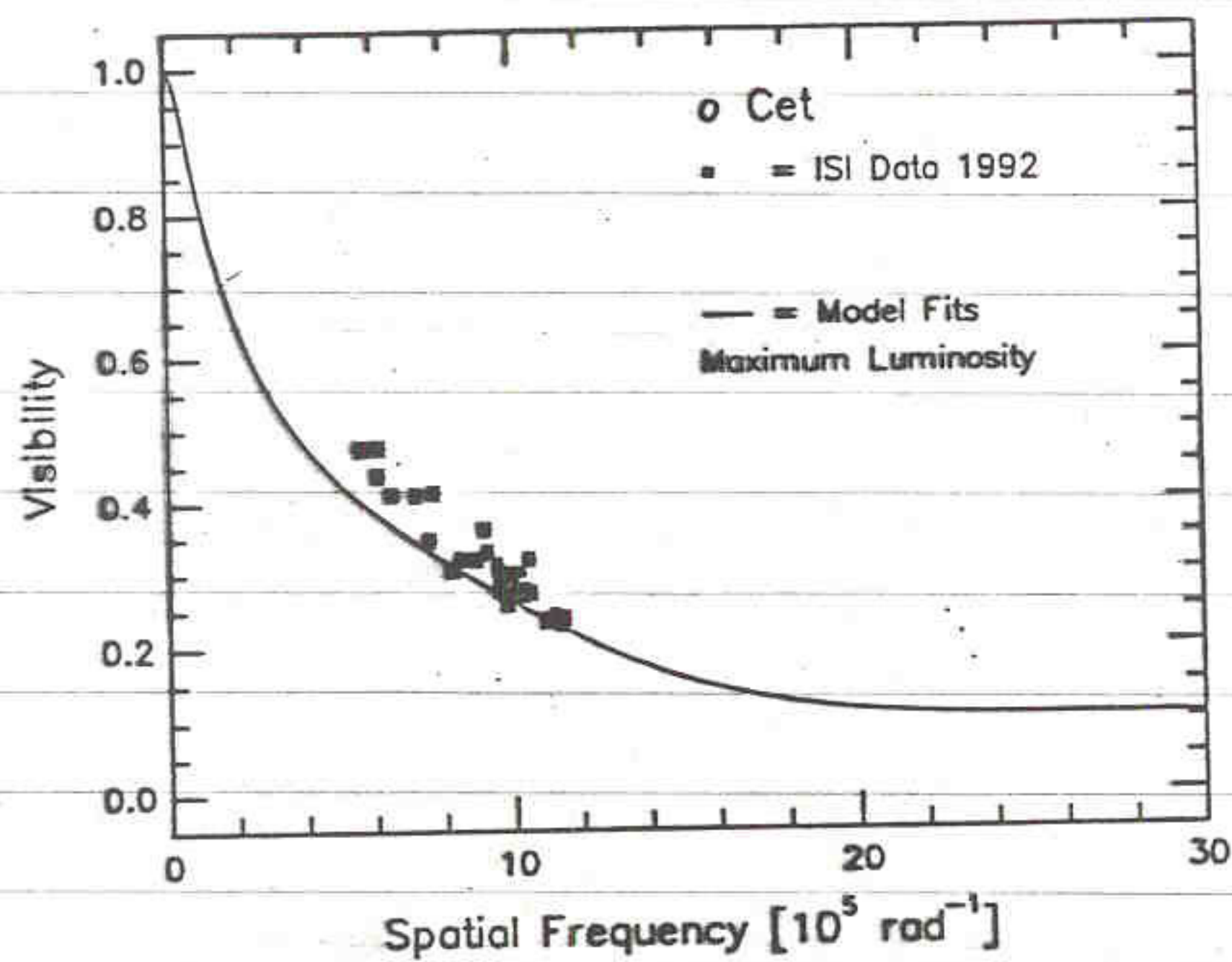
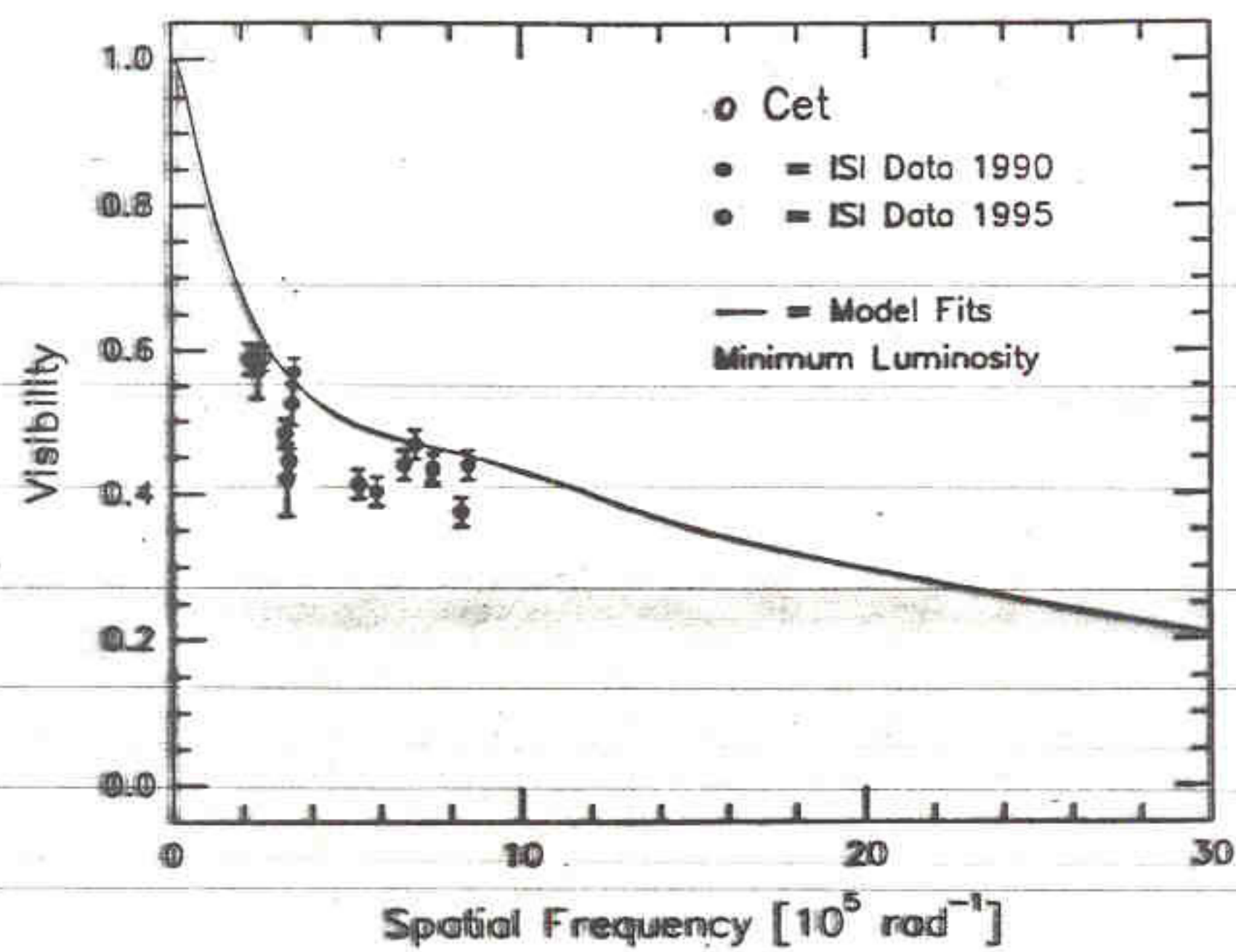
224, 339.



UKIRT Geballe

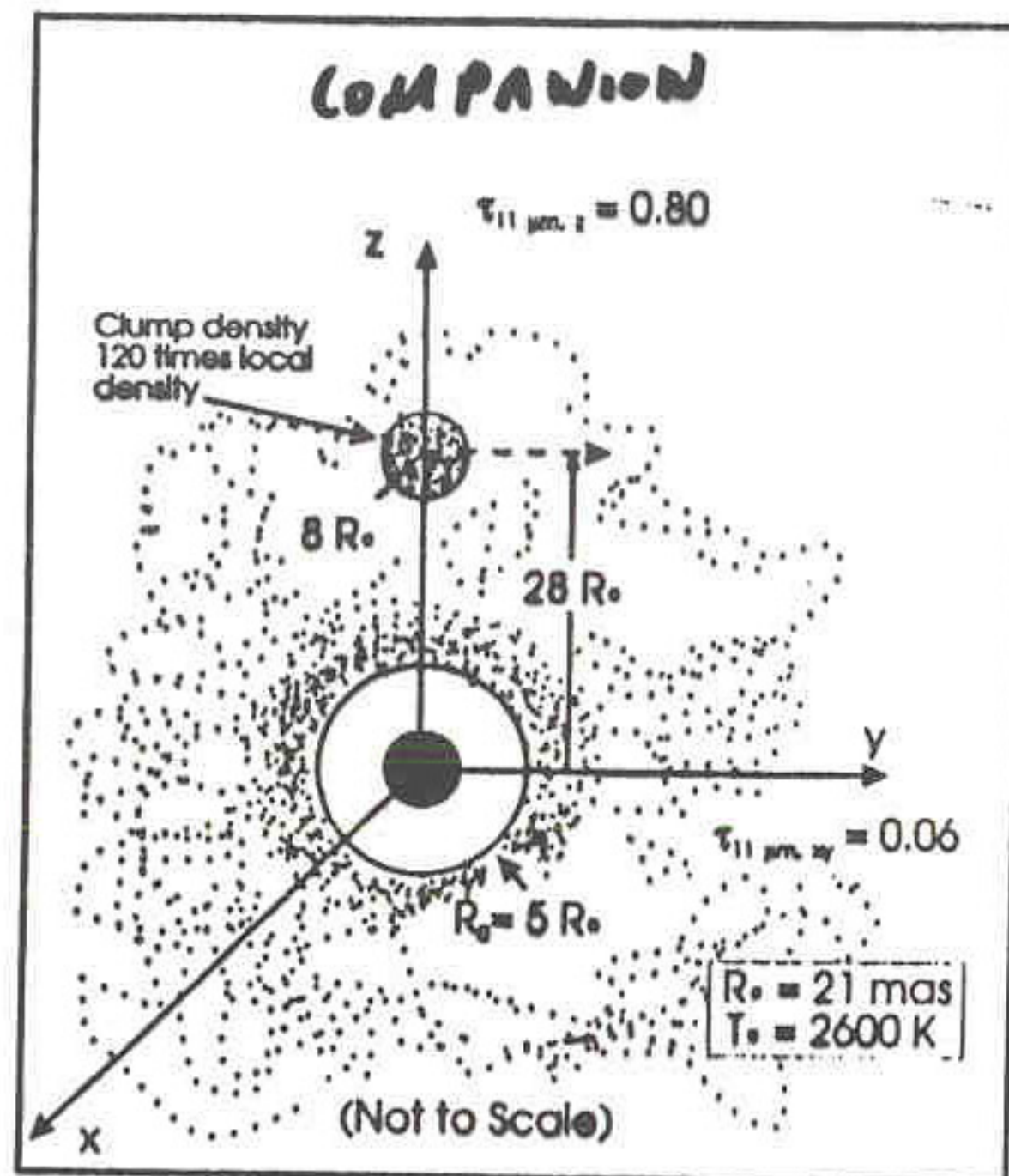




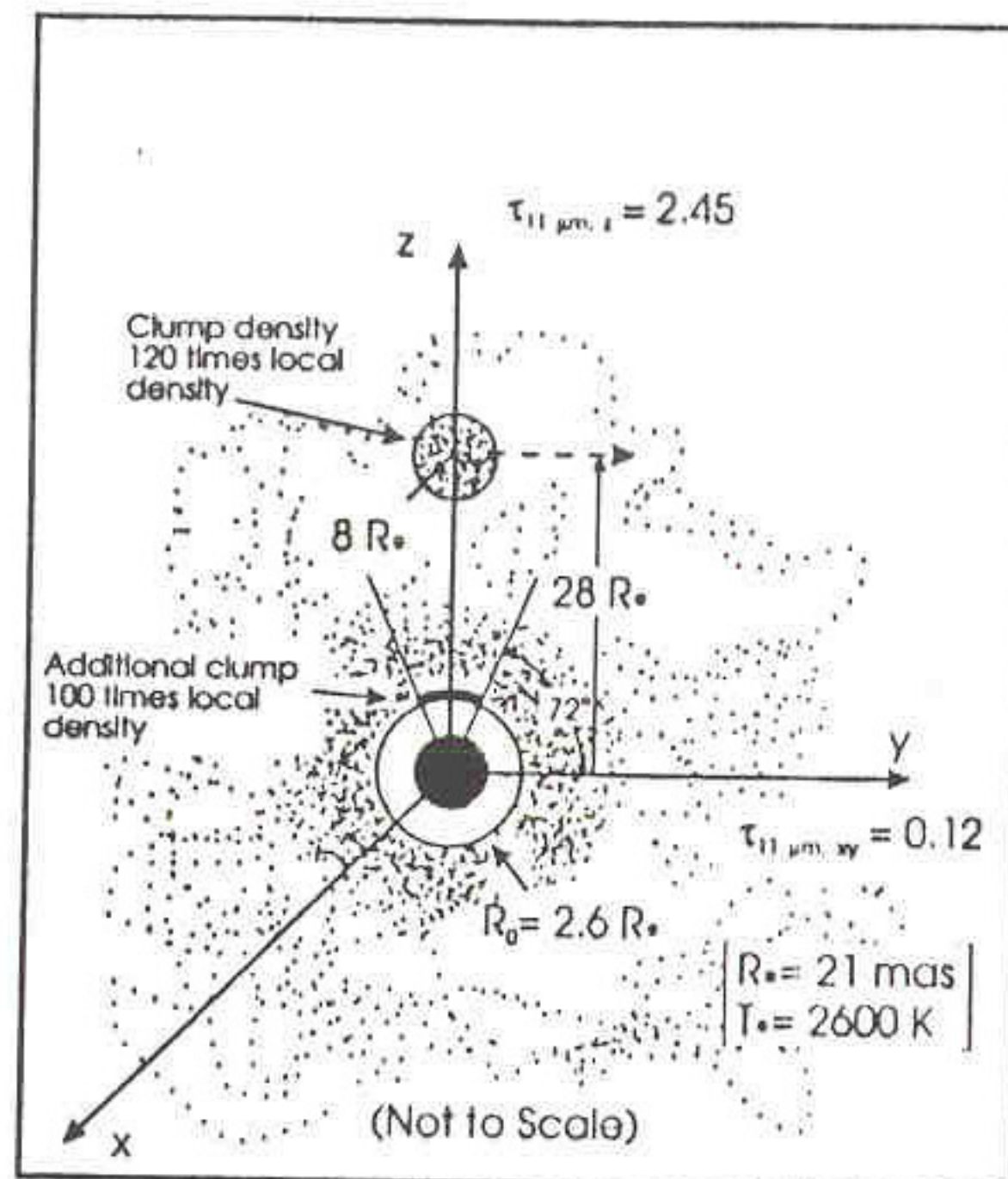


o Ceti Clump 1 Type Models

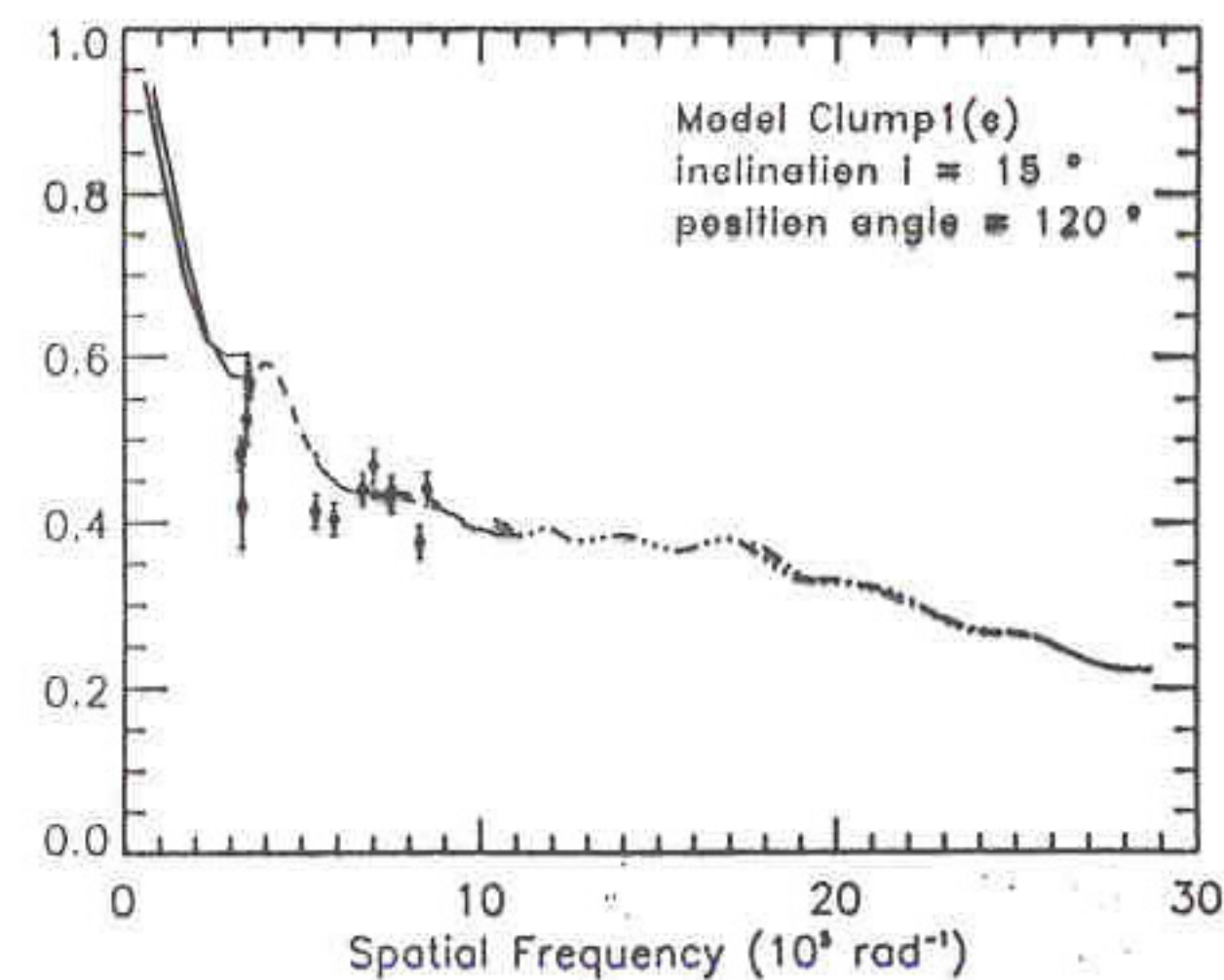
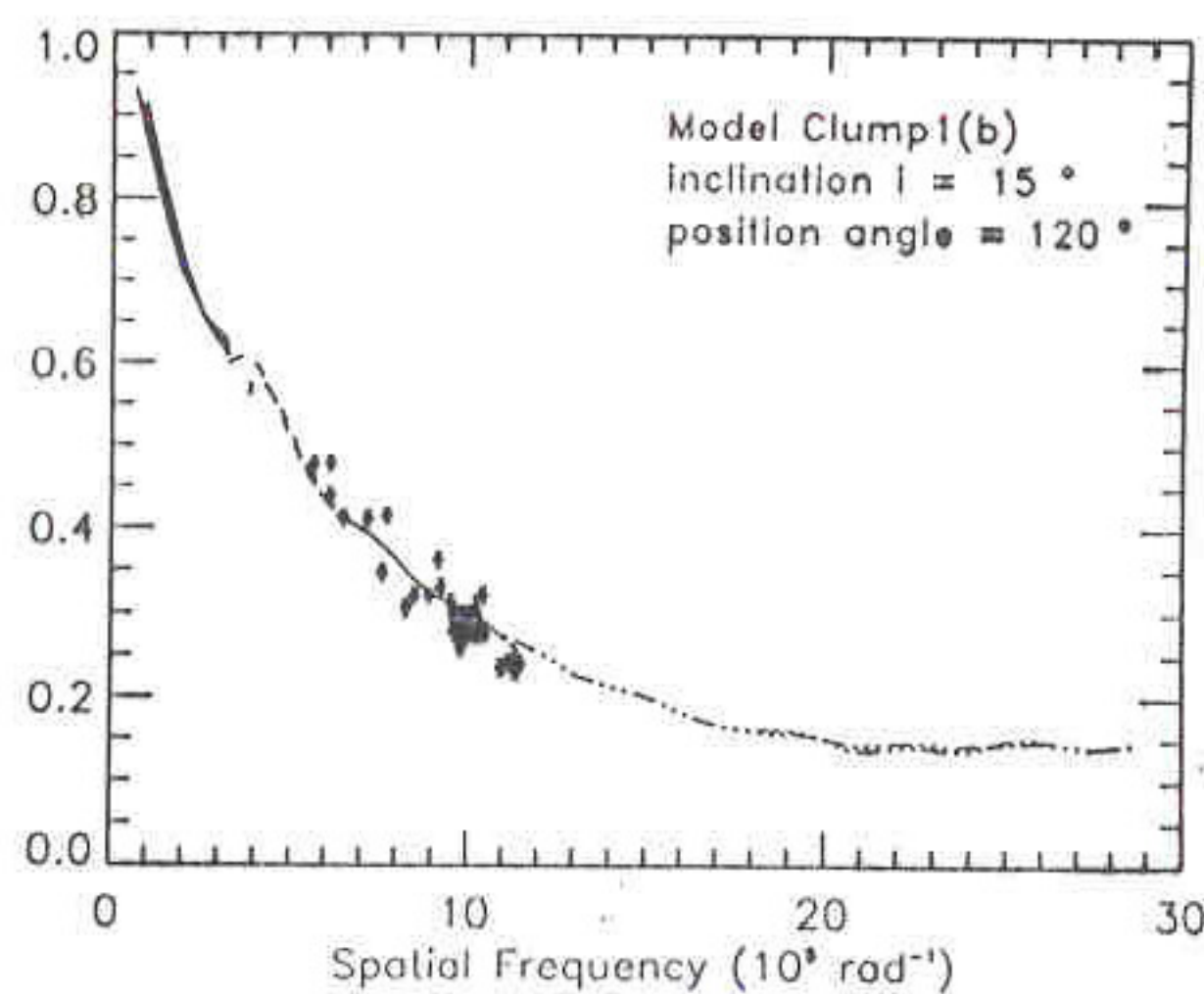
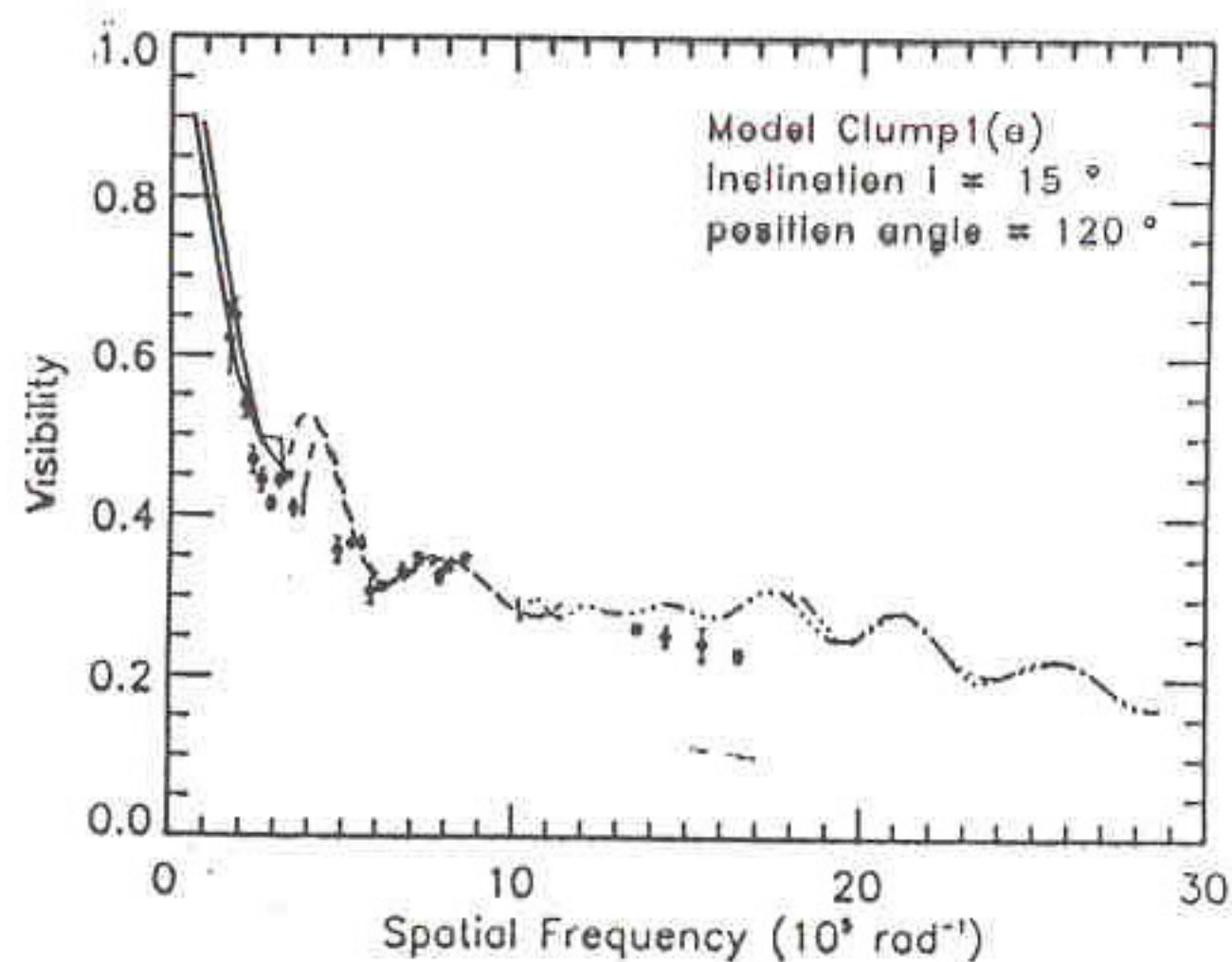
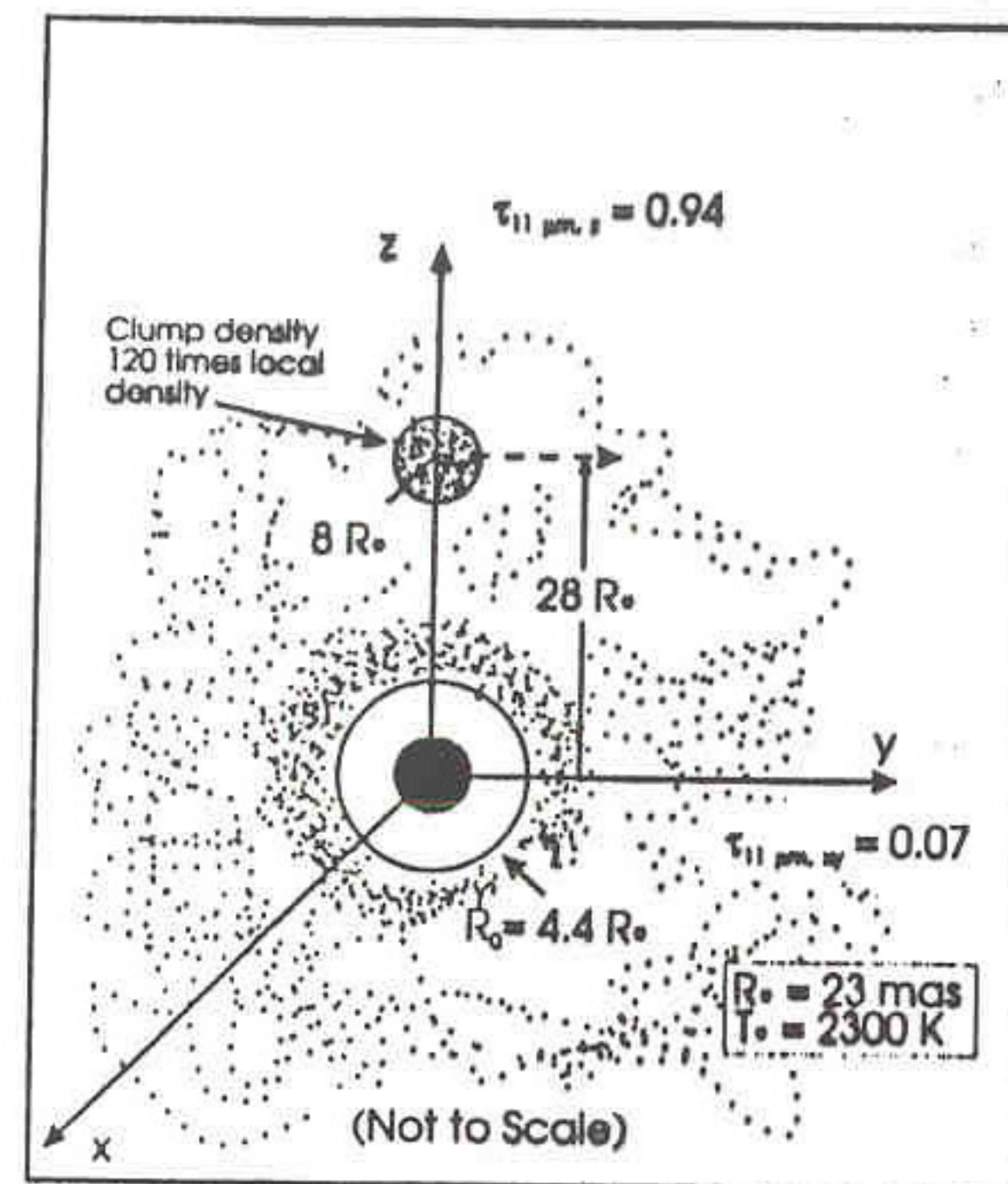
Model Clump 1(a) for
1989, 1993, 1994 Maxima



Model Clump 1(b) for
1992 Maximum



Model Clump 1(c) for
1990, 1995 Minima



NML Tan

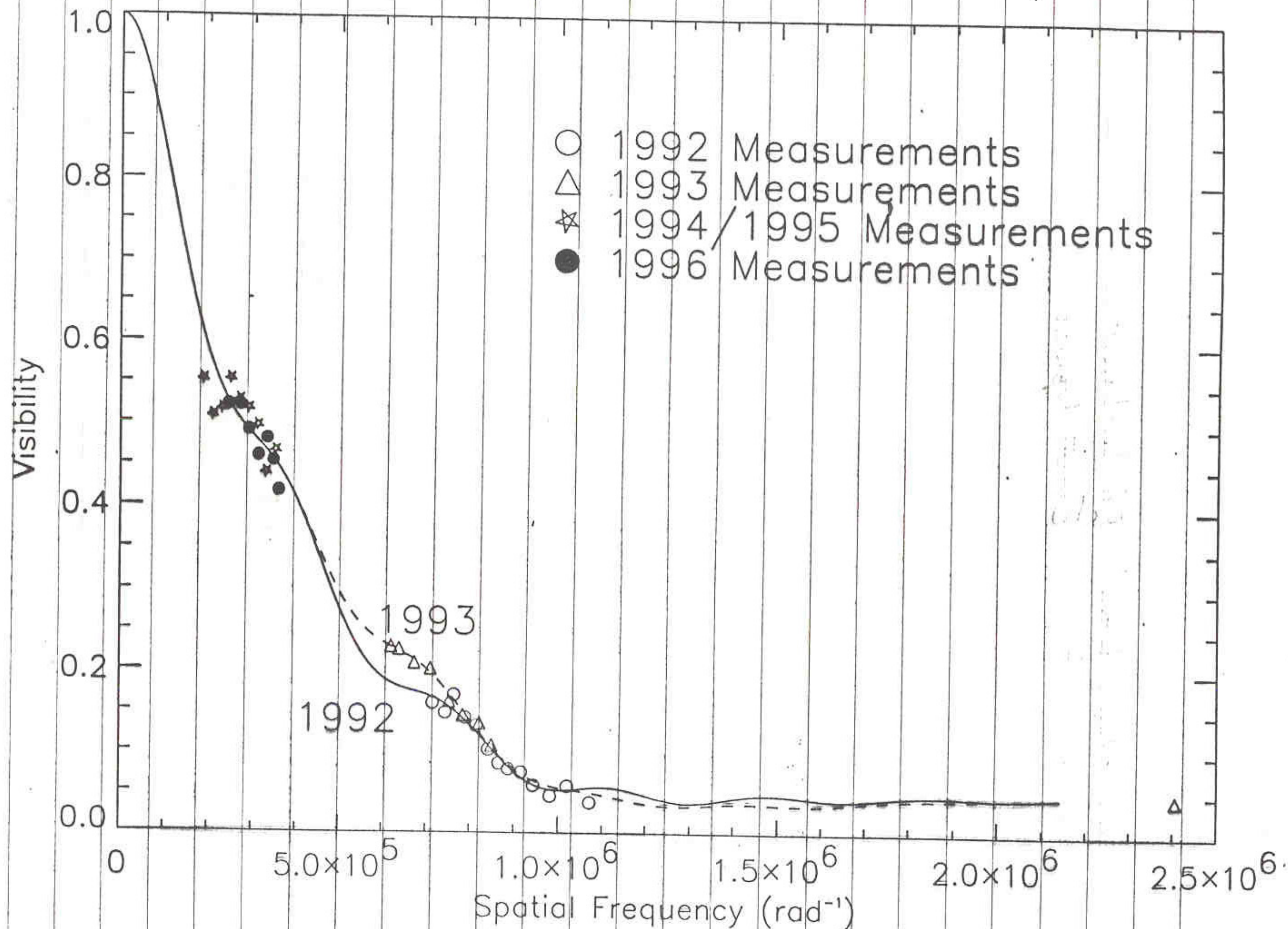


Figure 2

NML Tau

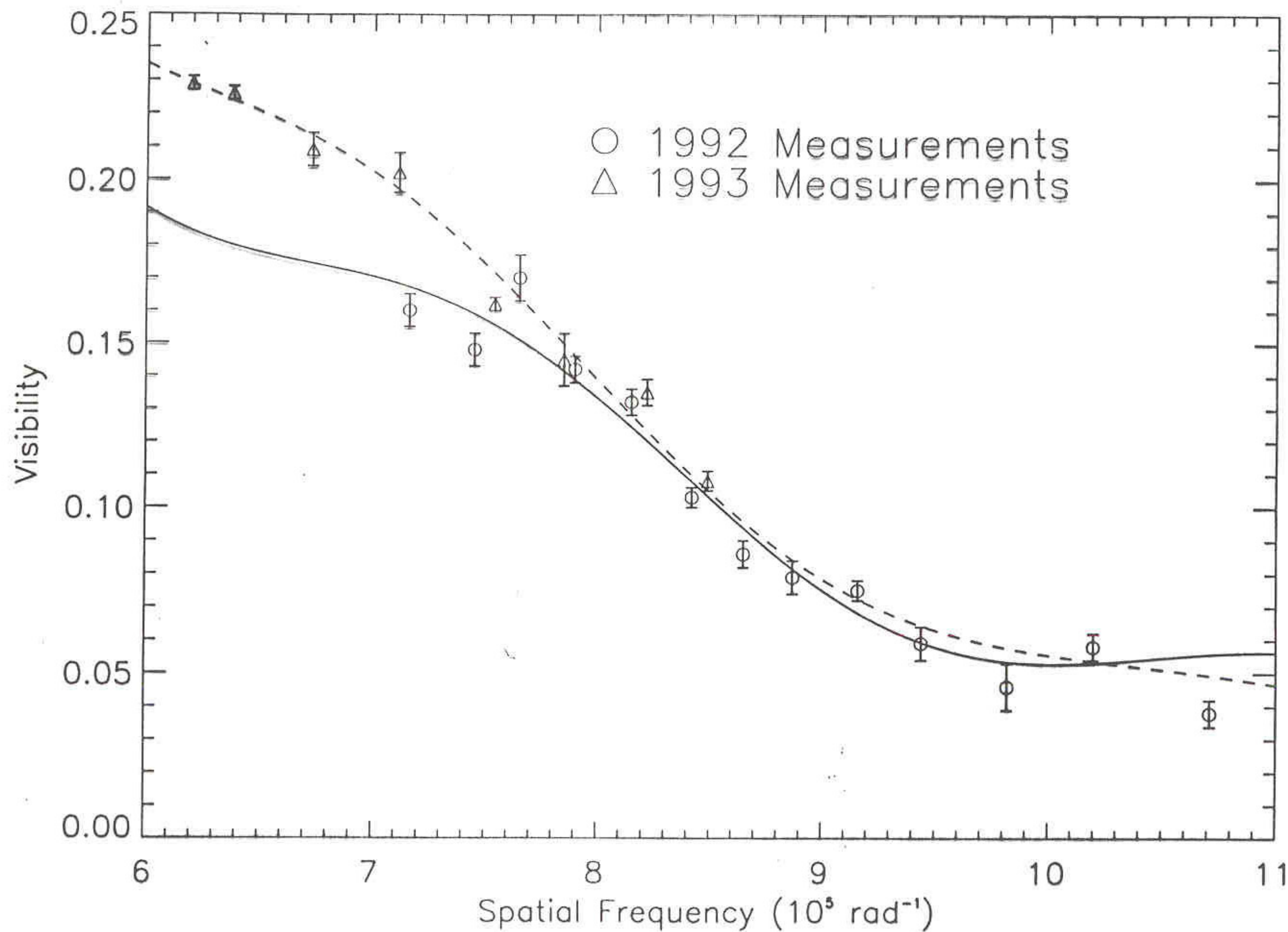


Figure 3

Hale et al. *ApJ* 1997,
450, 407

NML Tau

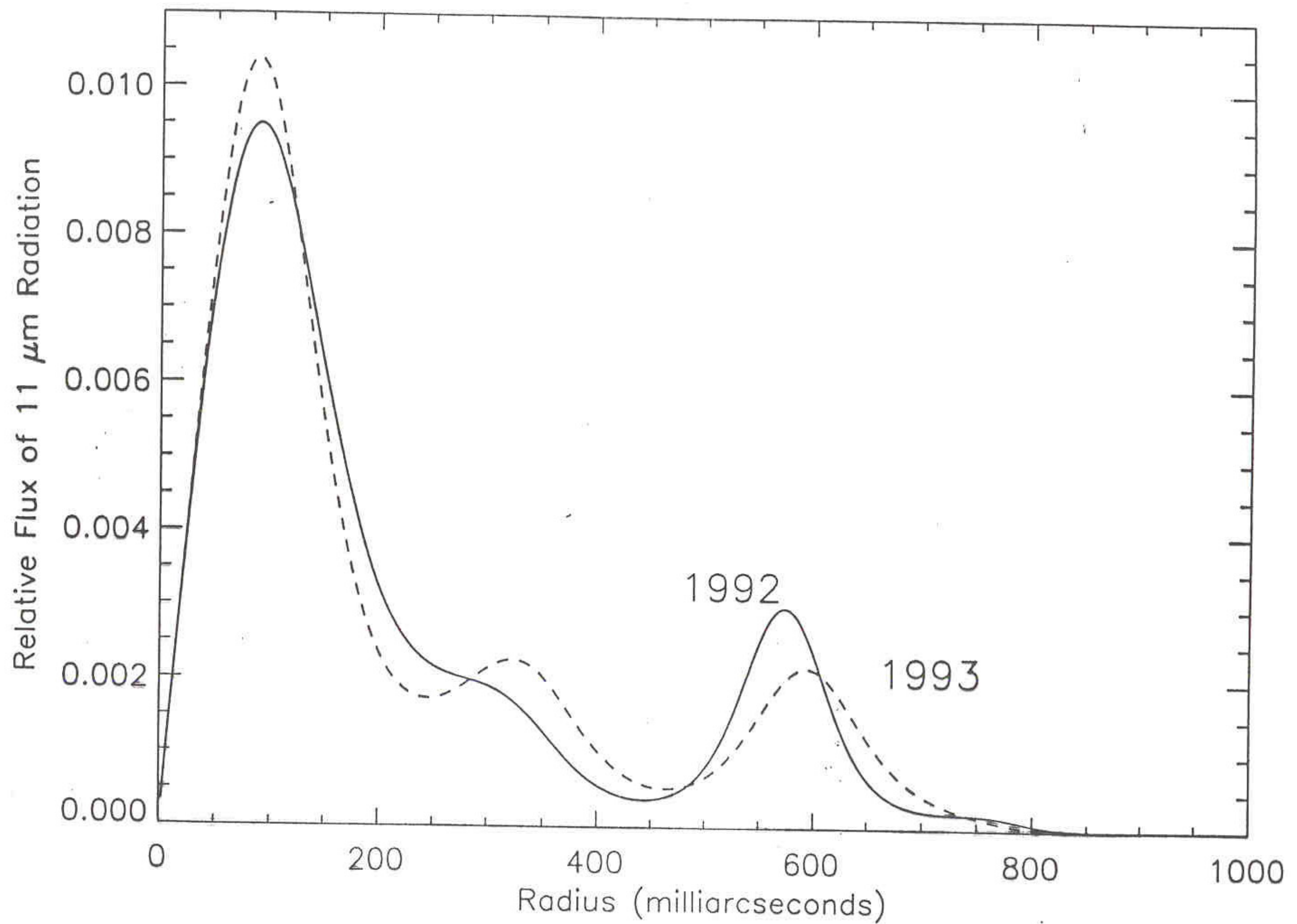


Figure 4

CONCLUSIONS:

- 1. Inner radii within a few stellar radii for Miras and Carbon stars.**
- 2. Wider variation for other spectral types**
- 3. Implies if dust always forms close to star, time scale for dust emission varies depending on spectral class**
- 4. Atmospheric scale height for VX Sgr in rough agreement with theory**
- 5. Diameters at 11 um consistent with optical diameters for supergiants Alpha Orionis and Alpha Scorpii.**
- 6. Alpha Orionis had a recent burst of dust formation.**
- 7. Dust is created and destroyed in complex environment of Omicron Ceti.**
- 8. Complex dust patterns exist for NML Tau and NML Cyg, not simple uniform outflows**
- 9. MANY INTERESTING RESULTS AND MORE TO COME!!!**

LONG BASELINE INTERFEROMETRY IN THE MID-IR HAS ALREADY PRODUCED IMPORTANT RESULTS AND HAS GREAT POTENTIAL FOR THE FUTURE.

High angular resolution on spectral lines:

- Study distribution of gas and dust separately
- High spatial and spectral resolution simultaneously
- Molecules:
NH₃, SiH₄, C₂H₄ in various excited states
- Sources:
IRC +10216, VY CMa, NML Cyg, NML Tau,
IRC +10011, IRC +10420, R Leo, α Her

Problems:

- Find CO₂ local oscillator lines close by using various isotopes like ¹²C, ¹³C, ¹⁴C, ¹⁶O, ¹⁸O
- Take into account LSR velocity of the source
- Need a more complex correlator

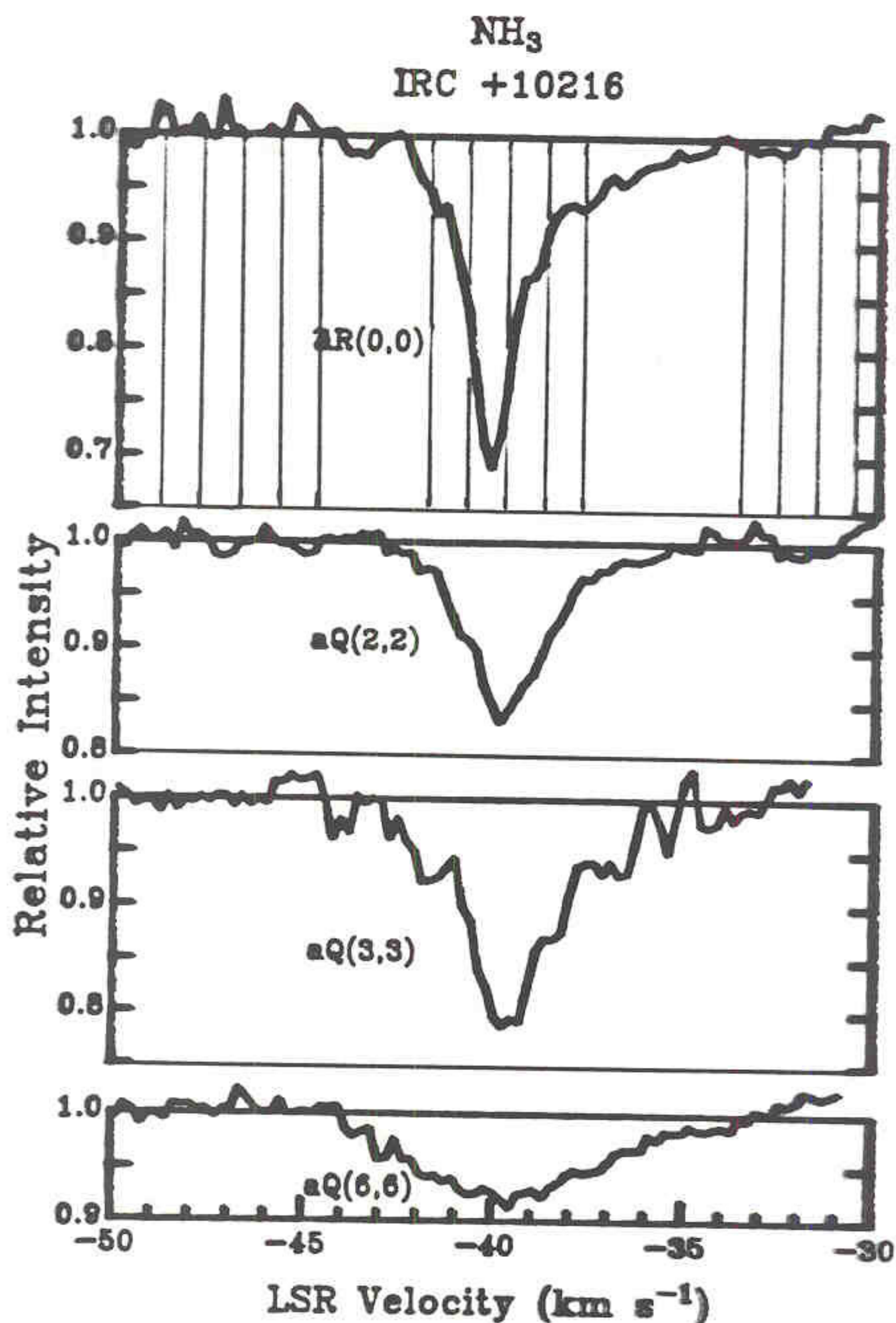
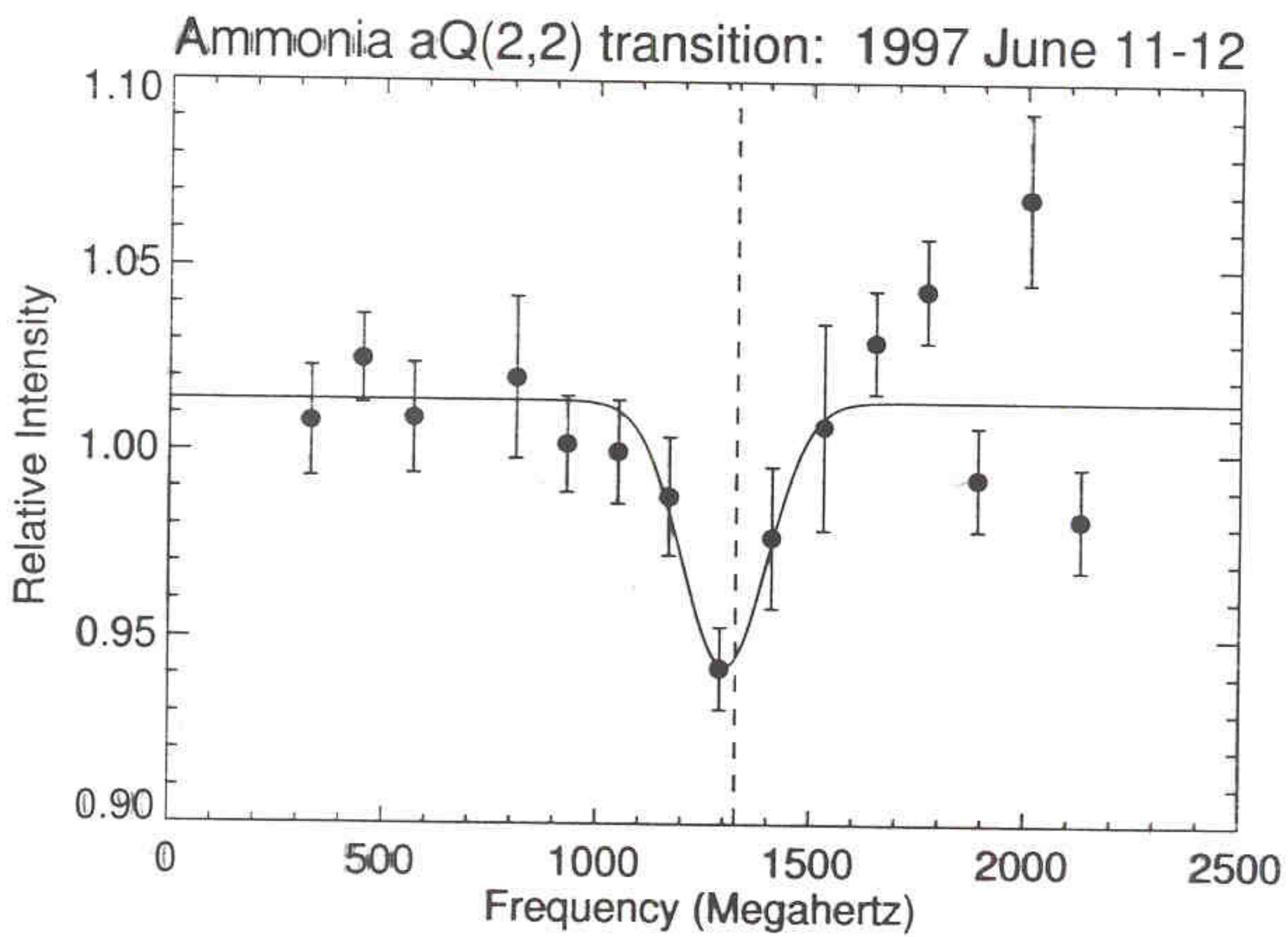
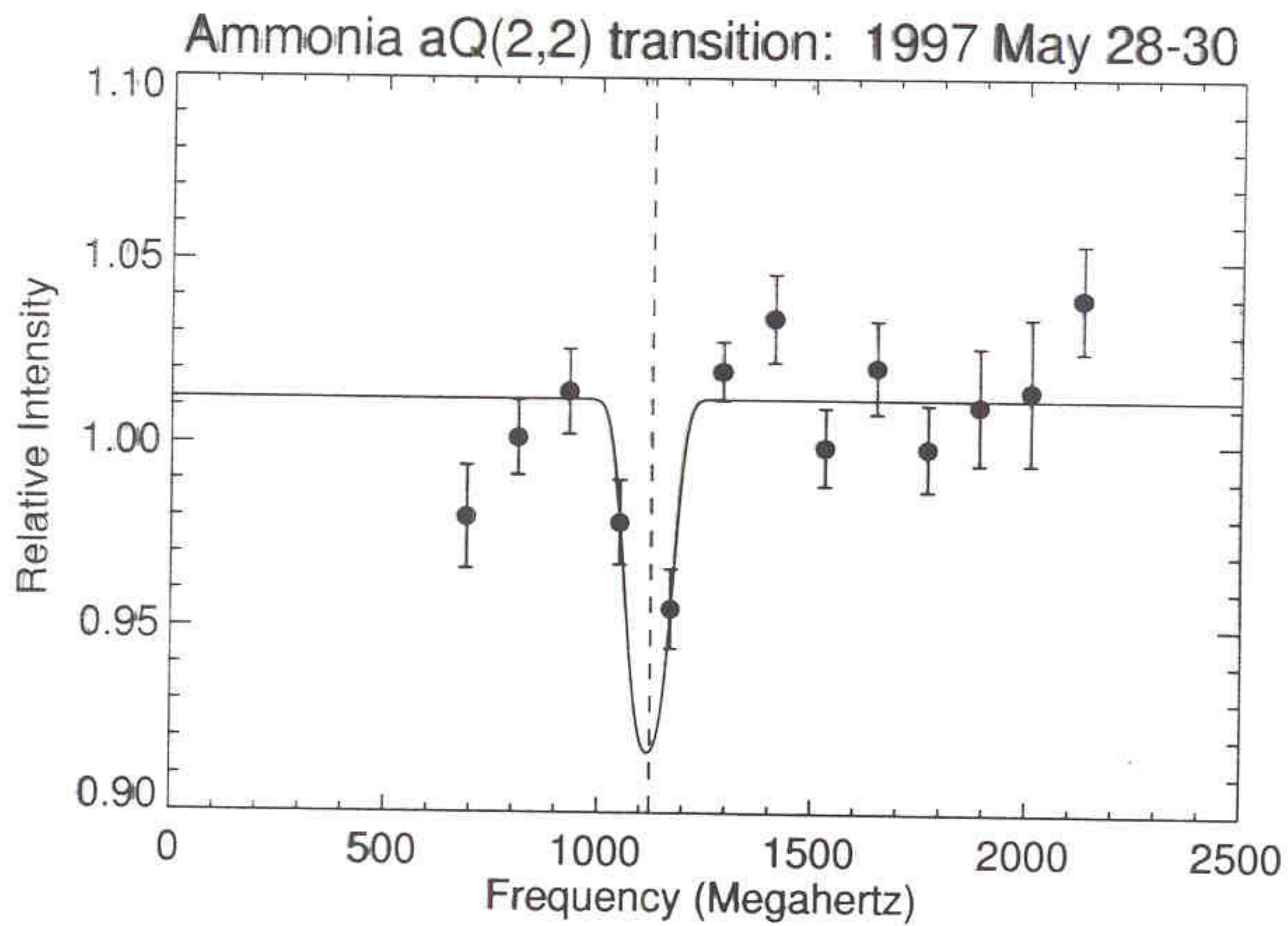


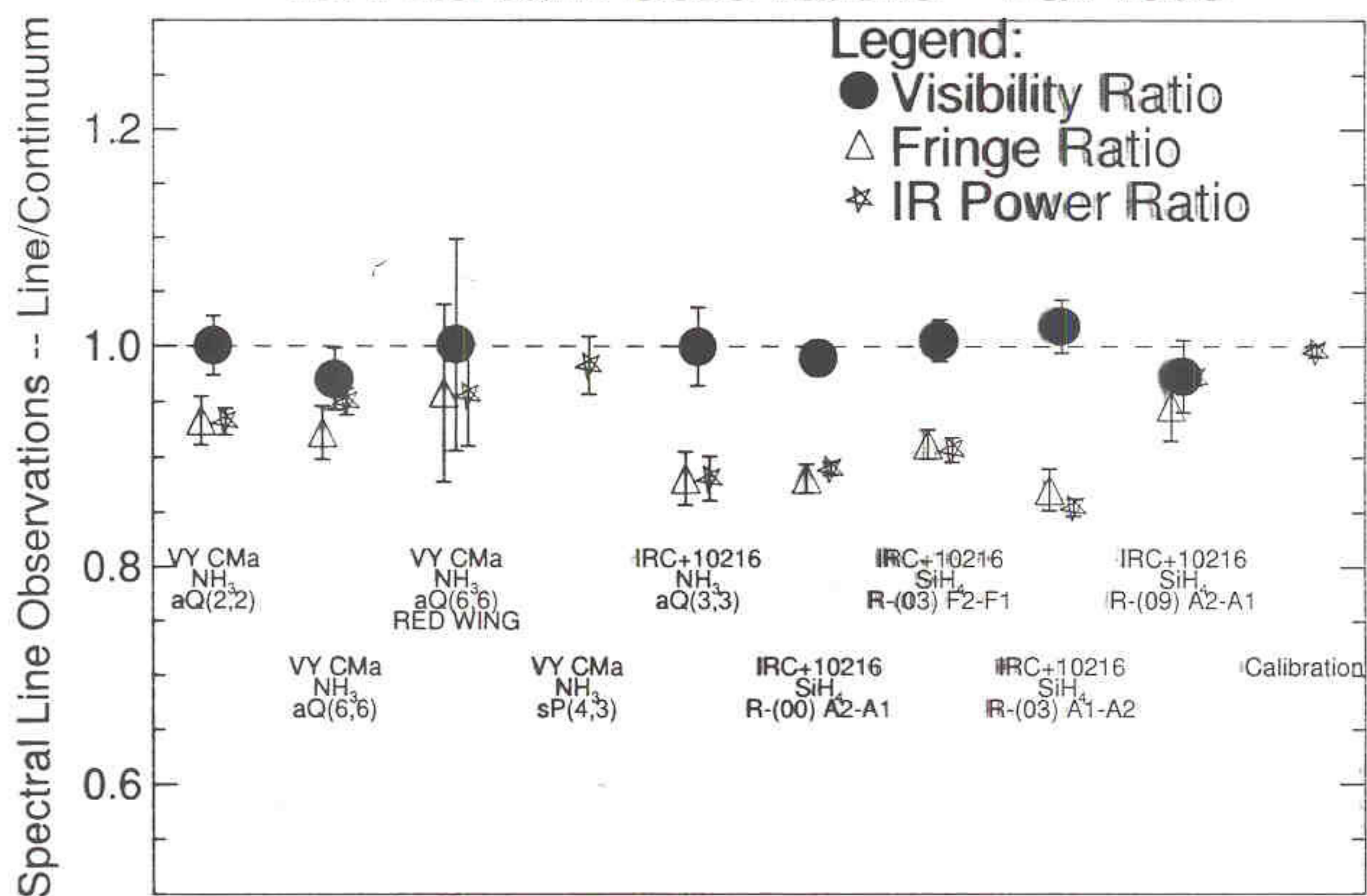
Fig. VI.10.

Absorption spectra of four lines of the ν_2 band of NH_3 observed in IRC +10216. The intensities are expressed relative to the observed SSB continuum level. These normalized SSB absorption profiles were extracted from the raw DSB absorption-emission profiles by the procedure given in Section VI.1.1.

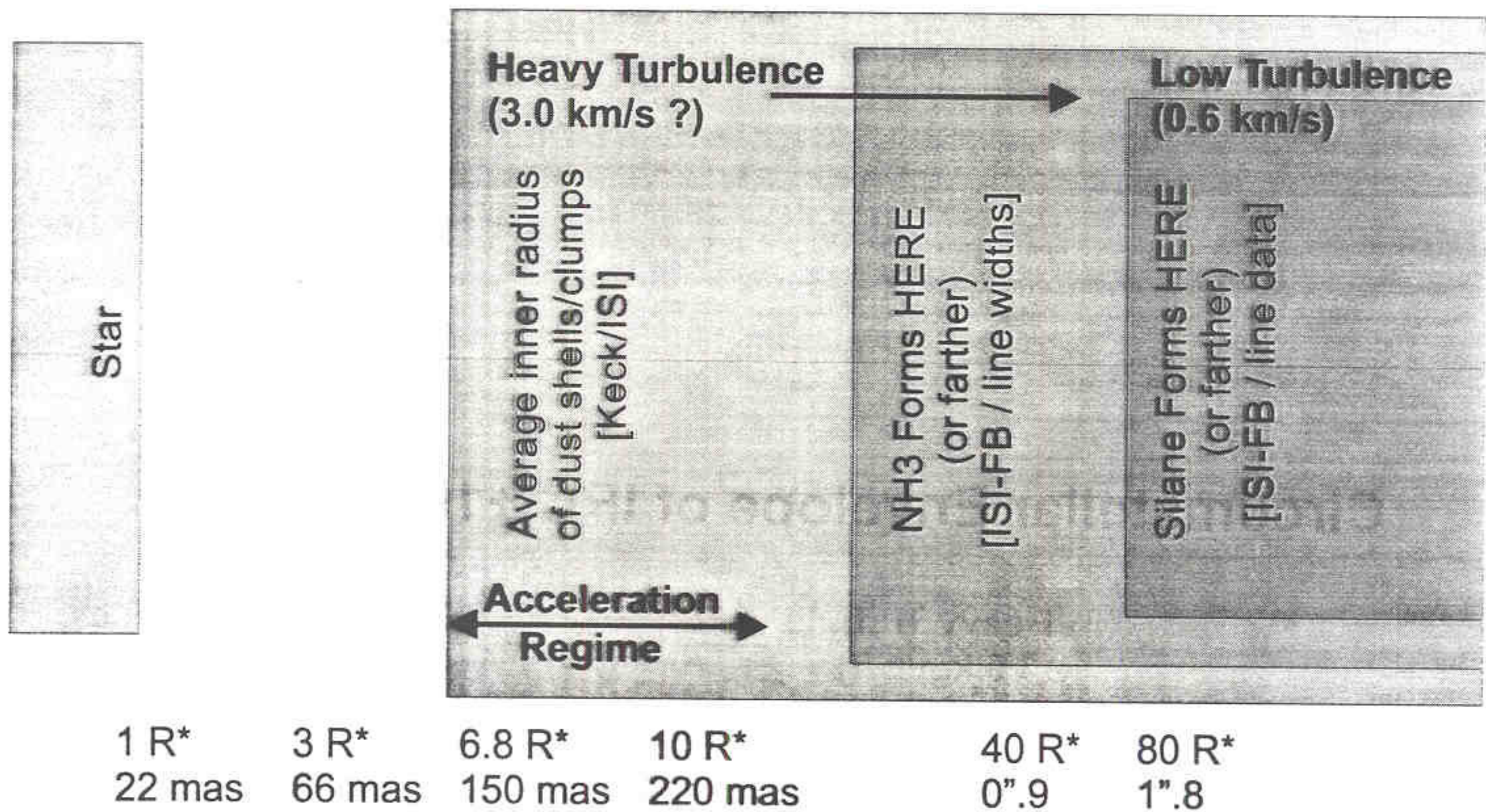
From: D.M. Goldhaber, Ph.D. Thesis, U.C. Berkeley, 1988



ISI Filterbank Observations -- Fall 1998



Circumstellar Envelope of IRC +10216



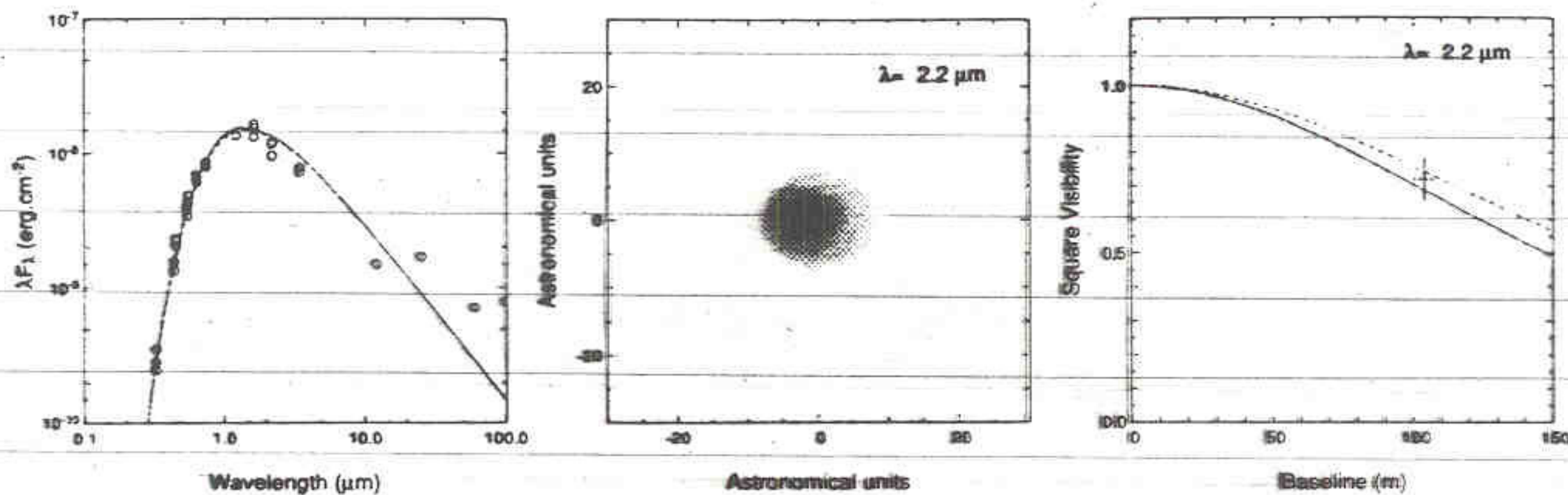


FIG. 4.— Accretion disk model: the left panel displays the SED from the literature data (circles) of the accretion disk model (dashed line), the star (dotted line), and the whole system (solid line), the middle panel displays the synthetic image of the accretion disk at $2.2 \mu\text{m}$, and the right panel displays the visibility curves of the accretion disk model for the x - and y -directions (solid line and dashed line, respectively). The result of our PTI observation of FU Ori is placed on the figure with its error bars.

$-\frac{1}{2}$ to $-\frac{3}{2}$), depending on the geometrical arrangement of the dust and heating source (Friedjung 1985). The temperature of dust 2 AU from this $L \sim 500 L_{\odot}$ object, i.e., at the minimum physical distance resolved by these observations, is ~ 750 K; at the 17 AU radius of the halo suggested by the speckle results, it is ~ 310 K. Hot material close to the star would emit strongly at $2.2 \mu\text{m}$ and with an optical depth roughly 5 times greater than the scattering optical depth (Draine & Lee 1984). The ratio of emitted light to scattered light is roughly

$$\frac{B_{\lambda}(T_{\text{eff}}(r))}{\omega B_{\lambda}(T_{\text{eff}})(r/R)^{-2}},$$

where ω is the albedo (~ 0.2 ; Draine & Lee 1984), r is the distance to the center, and R and T_{eff} are the equivalent radius and effective temperature of the central source, respectively. With $R = 4 R_{\odot}$ and $T_{\text{eff}} = 6000\text{--}8000$ K, the ratio is much larger than 1 at 2 AU and much smaller than 1 at 17 AU. While a detailed radiative transfer model must be used to assess the relative importance of scattering and thermal emission, we regard thermal emission as likely to be dominant if the radius of the putative dust halo is much smaller than ~ 10 AU, whereas scattering will be important if the radius is much larger.

Accretion disk model.—Following MB95, thermal emission from an accretion disk of the type proposed by HK85 and KHH88 is expected to be resolved in the PTI data, with approximately the observed fringe visibility. We computed a disk model with a surface temperature distribution proportional to

$r^{-3/4}$ in order to fit the observed SED.* The model implies an accretion rate of $\dot{M} \sim 6 \times 10^{-5} M_{\odot} \text{ yr}^{-1}$ for a $1 M_{\odot}$ star, an $A_V \sim 1$ mag, and an inclination angle of $i \sim 30^{\circ}$. The resulting synthetic image at $2.2 \mu\text{m}$ is displayed in Figure 4 (middle panel), together with the predicted visibility curves for the major and minor axes (right panel). Our interferometric data are in very good agreement with the accretion disk model. However, the precision of the individual visibility measurements is inadequate to constrain the position angle for the disk.

5. CONCLUSIONS

We have resolved a young stellar object for the first time using long-baseline interferometry in the near-infrared, achieving a projected spatial resolution of 2 AU using the Palomar Testbed Interferometer. Although the single visibility measurement presented here can offer only limited constraints on existing astrophysical models, it is reassuringly consistent with the accretion disk that was inferred from earlier spectral and spectrophotometric data. More sensitive multiaperture infrared interferometers like the Keck interferometer and the Very Large Telescope Interferometer, which are now under construction, will soon enable more robust studies by producing true images of the disks of FU Orionis stars with ~ 2 AU resolution and even more detailed images of the disks of less luminous T Tauri stars.

* The photometry data are from Allen (1973), Glass & Penston (1974), KHH88, and the IRAS.

REFERENCES

- Allen, D. A. 1973, *MNRAS*, 161, 145
 Burrows, C. J., et al. 1996, *ApJ*, 473, 437
 Colavita, M. M. 1998, *PASP*, submitted
 Colavita, M. M., et al. 1994, *Proc. SPIE*, 2200, 89
 DeWarf, L. E., & Dyck, H. M. 1993, *AJ*, 105, 2211
 Draine, B. T., & Lee, H. M. 1984, *ApJ*, 285, 89
 Friedjung, M. 1985, *A&A*, 146, 366
 Glass, I. S., & Penston, M. V. 1974, *MNRAS*, 167, 237
 Hartmann, L., & Kenyon, S. J. 1985, *ApJ*, 299, 462 (HK85)
 ———. 1996, *ARA&A*, 34, 207
 Herbig, G. H. 1966, *Vistas Astron.*, 8, 109
 Kenyon, S. J., & Hartmann, L. 1991, *ApJ*, 383, 664
 Kenyon, S. J., Hartmann, L., & Hewett, R. 1988, *ApJ*, 325, 231 (KHH88)
 Malbet, F., & Bertout, C. 1995, *A&AS*, 113, 369 (MB95)
 Nakajima, T., & Golimowski, D. A. 1995, *AJ*, 109, 1181
 Perryman, M. A. C., et al. 1997, *A&A*, 323, L49

TABLE 1
VISIBILITY DATA

Band	Baseline (M λ)	Visibility* (%)	rms (%)	Observation Number	Number of Nights
H	12.8	78 \pm 2	5.7	10	2
	23.1	56 \pm 1	3.7	14	3
K	9.6	85 \pm 1	1.0	3	2
	17.3	69 \pm 3	5.6	6	1

* The visibility uncertainties are the error in the mean, $\text{rms}/(N_{\text{obs}} - 1)^{1/2}$.

atmospheric seeing on the data. The visual magnitudes (V), spectral types, angular separations (d) from AB Aur, and the approximate angular diameter (θ) of the calibrator stars used for the AB Aur ($V = 7.1$, $H = 5.1$, $K = 4.4$, A0) observations are as follows: HR 1343 ($V = 4.93$, G8 III, $d = 9''.0$, $\theta = 1.5$ mas), HR 2219 ($V = 4.35$, G8.5 IIIb, $d = 17''.9$, $\theta = 2.0$ mas), and HR 1626 ($V = 6.14$, K0 II-III, $d = 2''.5$, $\theta = 1.0$ mas).

2.2. Visibility Results

Each individual fringe is fitted in the time domain, using the instrument's theoretical point-source response as a template, in order to determine the fringe visibility. From the 500 independent visibility values in each observation, we estimate the source visibility using a physical model of the visibility distribution function. Our model incorporates the source visibility, the signal-to-noise ratios of the individual visibilities, and the effect of random tilts between the wave fronts from the two telescopes that arise from atmospheric seeing. We find that seeing effects can strongly bias the estimate of visibility from a distribution. Hereafter, we use the term "visibility" to mean the estimated source visibility, with the atmospheric seeing and instrumental biases removed. A detailed description of the model and estimation procedure will be presented in a future paper. We note that a simpler method for the estimation of visibilities, such as the mean of the 500 independent values, results in a larger scatter when nights of different seeing conditions are included; however, the main results of this Letter would be essentially unchanged.

Observations of AB Aur were made throughout the time period 1997 October–1998 March using two baselines, the longest IOTA baseline of 38 m, which is oriented approximately north-northeast, and a 21 m north-south baseline. For these baselines, the projected baseline length on AB Aur varied by less than 1% over the hour angle range observed (approximately -1 to 3 hr). Moreover, measurements made on the longest baseline show no evidence of a variation in the visibility as the interferometer baseline rotated with respect to the source. For these reasons, we have considered all observations of AB Aur on a given baseline to be independent estimates of the same visibility value, and we have used the observed distribution of measurements about the mean value for each baseline to assess the overall measurement error.

The average values of visibility for the H and K' bands are presented in Table 1. We find that the distribution of visibility estimates about the mean is characterized by an rms value of approximately 5%, which therefore would represent the typical error in a single AB Aur measurement due to all sources. We attribute the bulk of this uncertainty to residual calibration errors, since this value exceeds the expected error due to random noise in the initial fringe-fitting process, which is on the order of 1%. Photometric variations of the star itself, which are common in pre-main-sequence objects, may also contribute

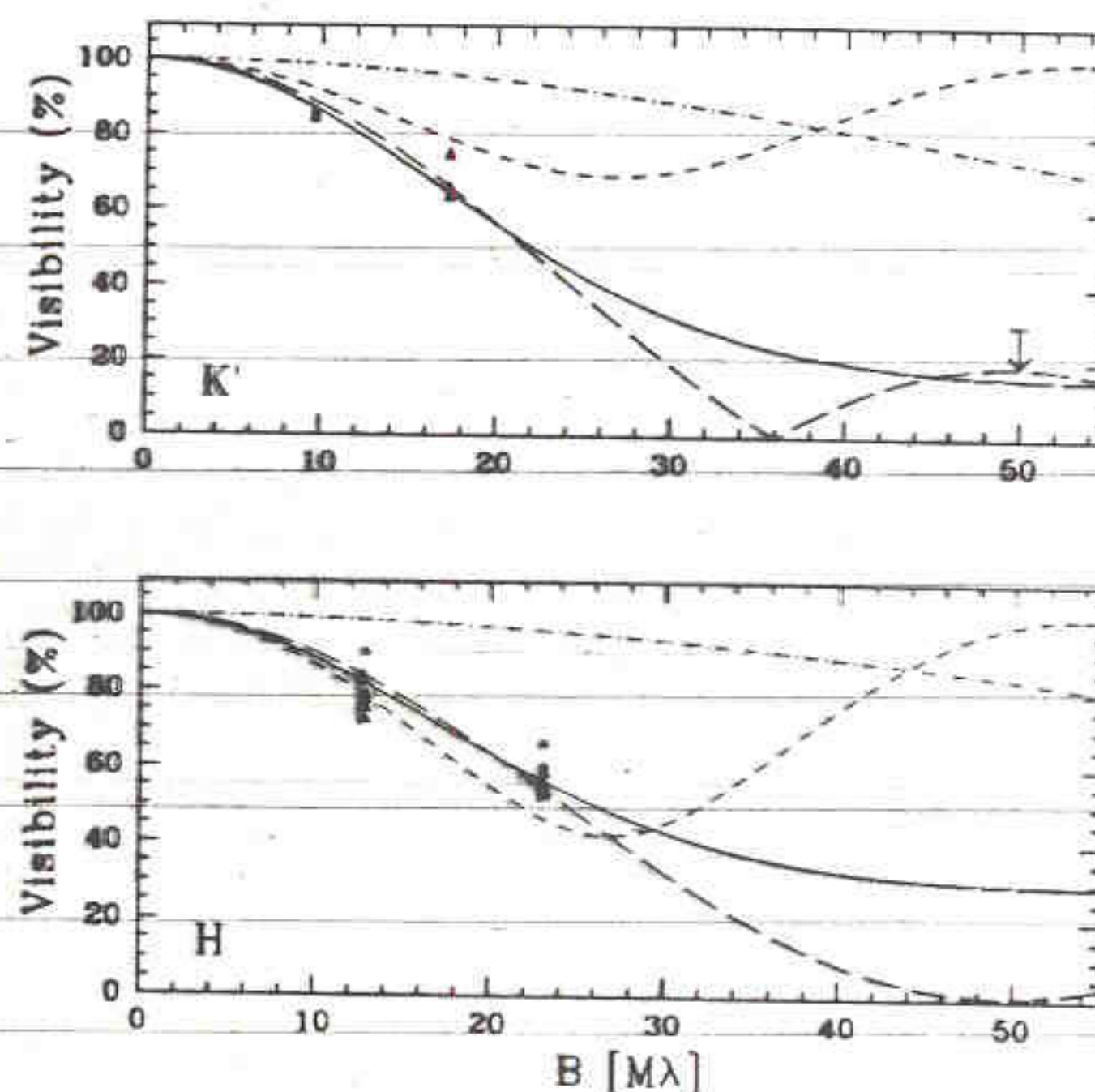


FIG. 1.— Visibility of AB Aur as a function of baseline length data and comparison with models of the source brightness distribution described in the text. The bottom panel shows the H -band data, and the top panel shows the K' -band data. The K' panel also shows the upper limit corresponding to the PTI observation. The models are plotted as follows: Gaussian (solid lines); ring (long-dashed lines); binary (dashed lines); and accretion disk (dash-dotted lines). The Gaussian and ring models provide an acceptable fit to the visibility data.

to the observed dispersion. However, we note that a change in the near-IR magnitudes of 0.1 would result only in a 1% change in the visibility, and therefore this effect is not believed to dominate the residual night-to-night variations observed.

Even considering a 5% calibration error source, the data demonstrate clearly that the AB Aur system is resolved. Moreover, we may use this error estimate to place an upper limit on the variation of visibility with changing baseline position angle on the source. We find that the visibility varies by less than 5% over the range of position angles observed (-10° to 20°). This result is important since it suggests that the source is not highly elongated. The data are shown in Figure 1, where we also include a visibility upper limit of 30% at a longer baseline (110 m) set by the nondetection of fringes in K -band observations at the Palomar Testbed Interferometer (PTI) (Berger 1998).

3. SOURCE MODEL

3.1. Near-IR Excess due to Circumstellar Material

The near-IR flux from the AB Aur system arises from both circumstellar material and AB Aur itself, and both contributions need to be taken into account in order to interpret the visibility data. To estimate the stellar and circumstellar near-IR fluxes, we use the V , R , I , H , and K photometry data tabulated by Hillenbrand et al. (1992), and we adopt an extinction to the star ($A_V = 0.5$) and an effective temperature of 10,000 K (van den Ancker et al. 1997). By adjusting the stellar radius to match the dereddened V , R , and I fluxes, we derive $R_* = 2.32 R_\odot$.

Using this model to represent the stellar contribution, we calculate the H and K stellar fluxes, and we deduce the excess fluxes due to circumstellar emission by subtracting from the dereddened total fluxes. We find that the excess flux represents

about 71% of the total in *H* and 84% in *K*. From the *H* and *K* excess fluxes (6.79 and 9.48 Jy, respectively), we derive a color temperature of 1865 K for the circumstellar material.

3.2. Visibility Models

The decrease in visibility with baseline length in Figure 1 indicates that the source is resolved by the interferometer and permits an estimate of the effective size of the near-IR-emitting region to be made. However, the size estimate depends significantly on the details of the source brightness distribution, and therefore we have made estimates for three plausible models of the source brightness. Each of the three models has two components, with the emission from the central star arising from a point source (R_* derived above results in an angular diameter at 144 pc of 0.15 mas and is therefore assumed unresolved) and the excess near-IR emission contributed by either (1) a circularly symmetric Gaussian brightness distribution; (2) a uniformly bright circular ring; or (3) a companion star modeled as a second point source. The peak surface brightness in the Gaussian model is set by the requirement that the flux of this component match the near-IR excess flux, and therefore, in this case, there is no a priori constraint on the actual intensity. For the ring model, however, we have constrained the extended component to have a surface brightness equivalent to that of a blackbody at the color temperature derived from the observed excess at *H* and *K*. Thus, for all models, the only fitted parameter is the size of the extended component or the binary separation. Finally, we note that in all cases, except the binary case, the model is circularly symmetric so as to be consistent with our limit on the variation of visibility with baseline position angle.

Table 2 summarizes the detailed features of each of the models and the results of fits of the models to the visibility data. The visibility functions for the best-fitting models are displayed in Figure 1 along with the data. A formal model fit to each individual color yields a somewhat larger size for the emission in the *H* band than for the emission in the *K* band. However, within the errors, we find that the derived sizes in the *H* and *K* bands are consistent with a single value. Thus, Table 2 contains the results of fits to the entire data set (excluding the PTI upper limit).

In addition to the descriptive models presented in Table 2, it is also possible to compute visibility predictions for physical source models considered by previous workers. Thus, in Figure 1, we present a model calculation for an accretion disk model (cf. Hillenbrand et al. 1992) for comparison with the data. For this example, we have adopted a $T \propto r^{-3/4}$ falloff for the temperature in the disk, and we determine the size of the hole and the temperature at the inner edge of the hole from the near-IR excess observed at *H* and *K*. The values thus obtained are 0.68 mas (0.10 AU) for the hole diameter and 3026 K for the brightness temperature at this position. These values are similar to those derived for AB Aur by Hillenbrand et al. (1992) from their fit to the entire infrared excess. Since the fluxes completely determine the model in this case, there are no free parameters left to fit to the visibility data, and therefore Figure 1 simply shows the visibility function that is predicted by the model. It is clear that this model does not agree with the visibility data.

4. DISCUSSION OF MODELS

Previous high angular resolution observations of AB Aur, via millimeter-wave interferometry (Mannings & Sargent 1997), mid-infrared imaging (Marsh et al. 1995), and near-IR speckle interferometry (Leinert, Richichi, & Haas 1997), have

TABLE 2
SUMMARY OF SOURCE MODELS

Parameter	Gaussian ^a	Ring ^b	Binary ^c
Size (mas)	4.66 ± 0.11	4.74 ± 0.09	3.85 ± 0.41
Size (AU)	0.67 ± 0.02	0.68 ± 0.01	0.55 ± 0.06
<i>H</i> -band T_b (K)	1318	1865	1865
<i>K</i> -band T_b (K)	1200	1865	1865
rms (%)	5.6	5.7	9.9

^a Gaussian model: the size is FWHM; T_b is the brightness temperature at the Gaussian peak. The observed brightness temperatures are consistent with optically thin emission from the source (see text).

^b Ring model: the size is the inner diameter of ring; the outer diameter is adjusted to match the flux in the *H* and *K* bands, yielding a ratio of outer/inner diameter of 1.14. The ring is considered to be optically thick, and T_b is constrained to be the color temperature of the infrared excess.

^c Binary model: the size is the angular separation of the primary and secondary (the companion is assumed unresolved) projected along the baseline direction; T_b is constrained to be the color temperature of the infrared excess.

all failed to resolve the inner ~1 AU where the near-IR emission arises. However, in this work, the use of a long-baseline, near-IR interferometer has enabled the system to be resolved for the first time. It is clear from Figure 1 and from consideration of the residual rms values that the Gaussian and ring models provide an adequate fit to the data, while the binary model and accretion disk models do not.

4.1. Binary Model

As noted by Hartmann et al. (1993), one plausible model for the infrared excess in Herbig Ae/Be stars is a companion embedded in a thick envelope of dust. In this case, the companion is invisible in the optical parts of the spectrum and appears as an infrared source because of the absorption of starlight by the dust envelope and the subsequent reradiation at cooler temperatures. The binary model shown in Table 2 and Figure 1 does not fit the visibility data as well as the other models presented. Moreover, our limit on the variation in visibility with baseline position angle constrains the possible orientation of the binary system. Considering the most complete set of data, the *H*-band observations on the longest IOTA baseline, we find that the binary position angle would have to lie within the range of 0° – 10° in order to be consistent with the 5% limit on the visibility variation. These special constraints make this model a less attractive explanation than the others presented here.

4.2. Accretion Disk Model

Figure 1 shows the visibility function that is predicted by the accretion disk model, and it is clear that this model does not agree with the visibility data. Indeed, we find that it is not possible to match simultaneously the visibility data and the infrared excess for any temperature power-law model in the range $T \propto r^{-0.5}$ – $r^{-1.5}$. Finally, we find that a general property of the visibility function of such models is that the effective size of the disk at the *H* band is smaller than that in the *K* band, in contradiction to the observation that both data sets are consistent with the same effective size. Thus, it appears that the accretion disk models commonly used to explain the source SED are not consistent with our interferometric measurements.

4.3. Ring Model

The choice of a ring to describe the emission was originally motivated by a desire to find a structure that is consistent with the effective size measured by the interferometer and with

Aperture Masking at Keck

Results and Science Potential

- Highest resolution images of circumstellar envelopes available
- Spiral dust shells discovered around Wolf-Rayet stars – colliding winds?
- Multi-wavelength diameter measurements to probe the atmospheric structures of Miras and Red Supergiants
- Circumstellar disks around Young Stellar Objects (YSOs) can be resolved for the first time
- Highly asymmetric flows around prototypical dusty AGB stars insist on new mass-loss mechanisms – or at least new twists on the old
- Proper motion studies in infancy, could be key to understanding these complicated envelopes
- In general, these observations offer an important data set to view in context of high resolution visible data (stellar hotspots) and radio/mm observations (SiO and H₂O masers)

Table 2. Uniform disc and point-source parameters for Betelgeuse.

Wavelength (nm)	Disk	Point source parameters		
	Diameter (mas)	Flux (percent of total)	Radius from center (mas)	PA (degrees)
846	57(+/-2)	10(+/-3)	9(+/-1)	391(+/-3)
		10(+/-3)	4(+/-5)	385(+/-10)
833	50(+/-1)	24(+/-2)	8(+/-2)	38(+/-5)
		11(+/-2)	4(+/-5)	390(+/-3)
700	49(+/-3)	10(+/-3)	8(+/-1)	385(+/-3)
		10(+/-3)	4(+/-1)	382(+/-3)
710	54(+/-2)	12(+/-2)	9(+/-2)	385(+/-3)
		11(+/-2)	9(+/-2)	385(+/-4)

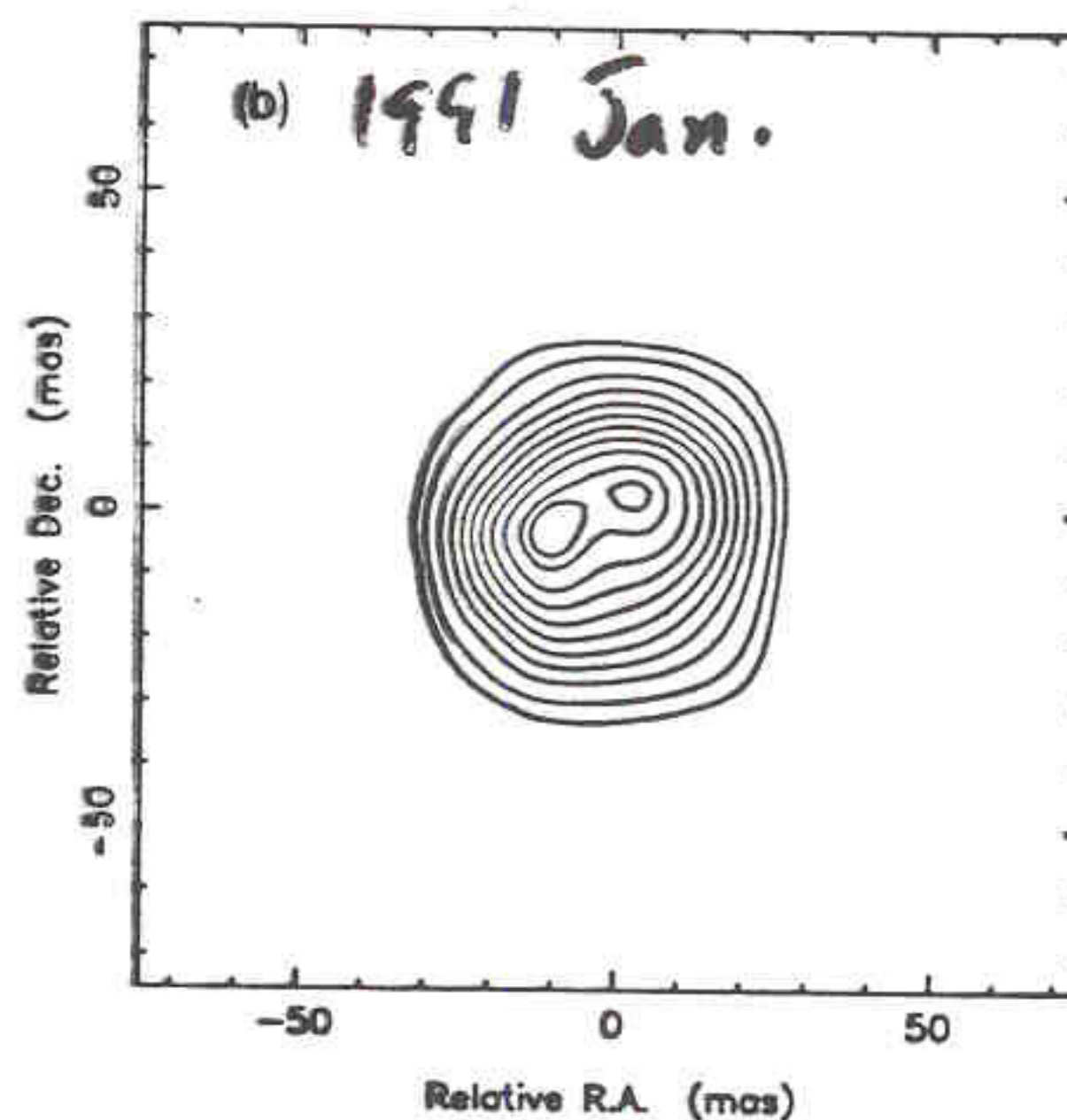
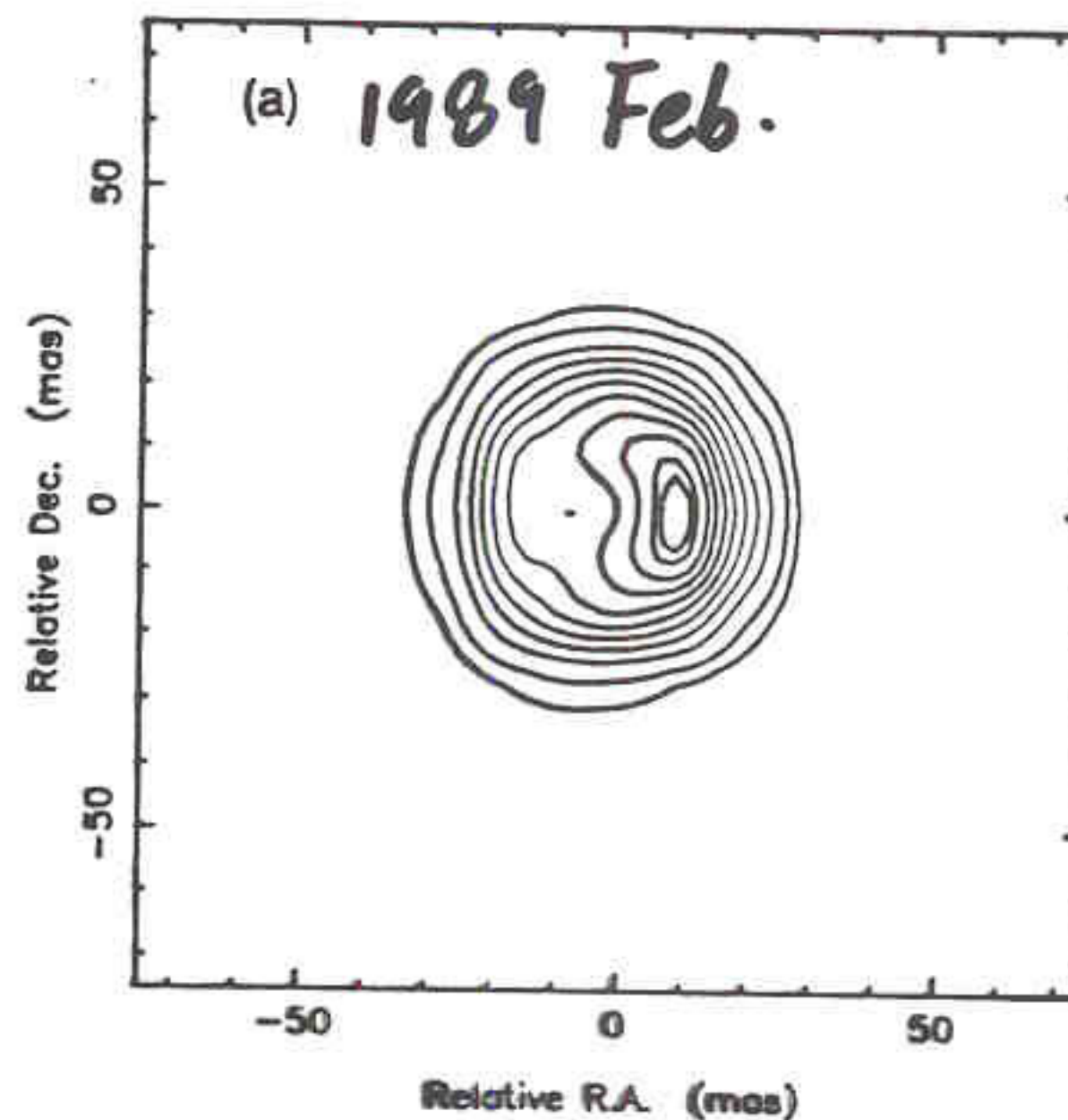
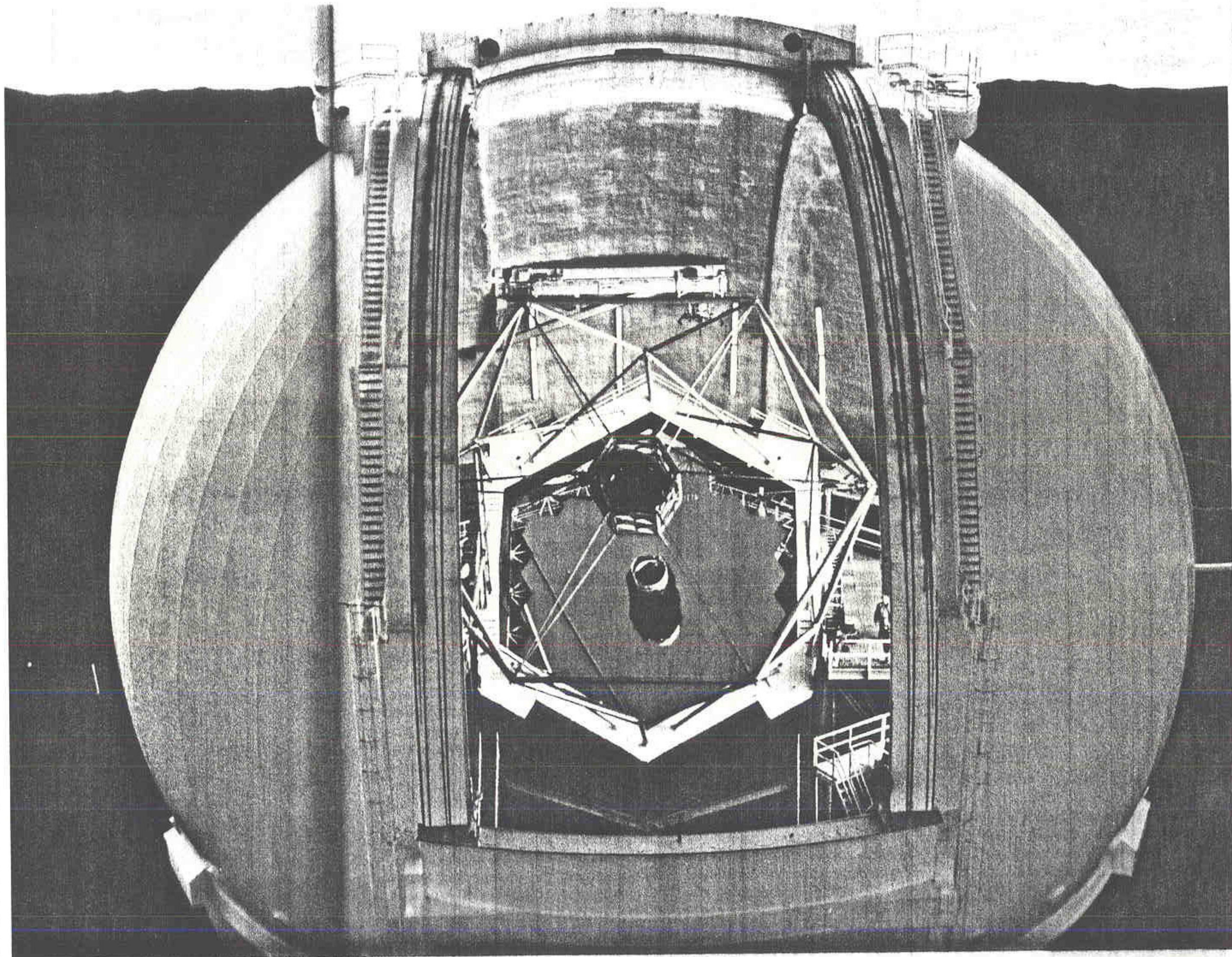


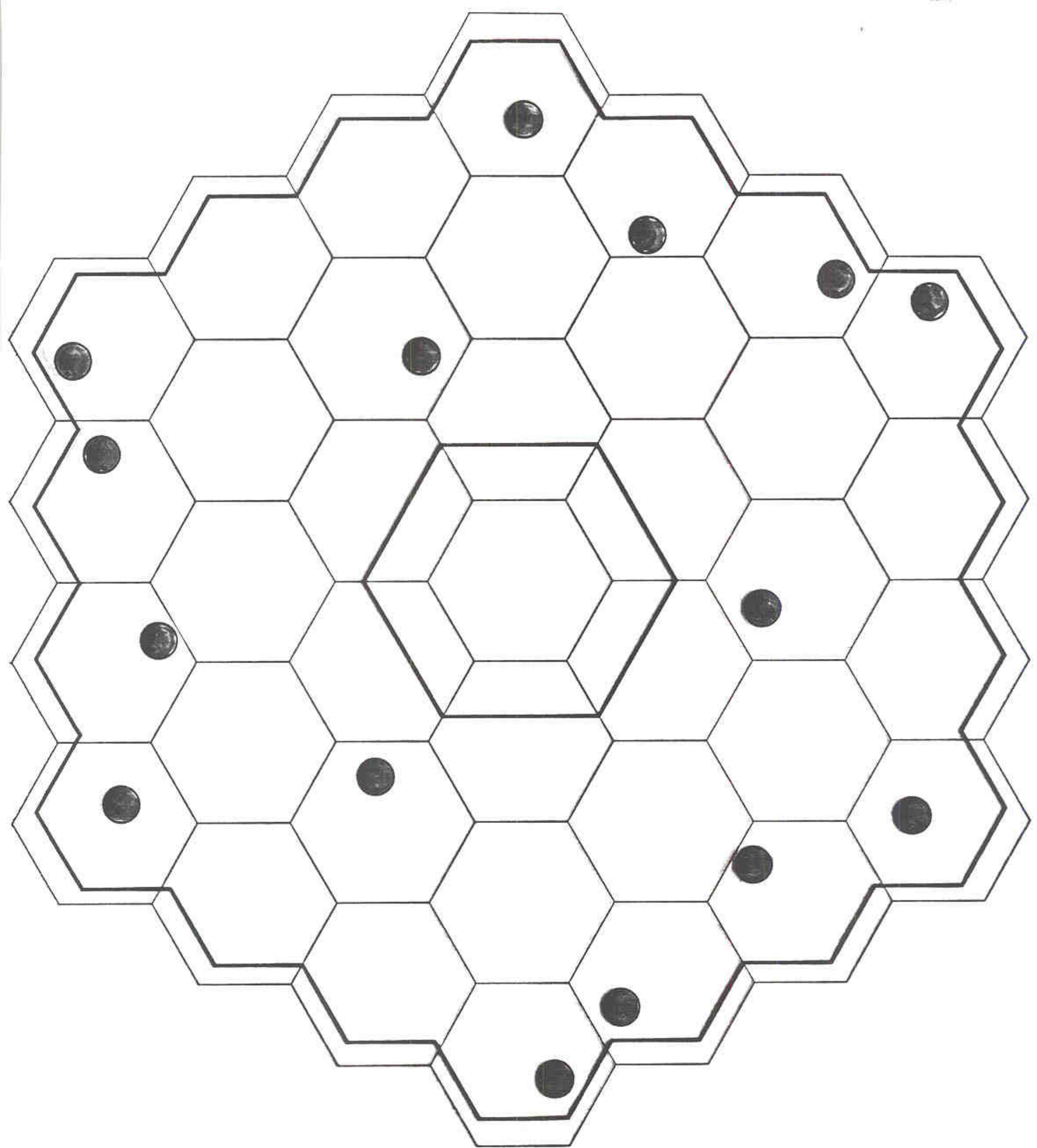
Figure 4. MEM reconstructions of Betelgeuse at 710 nm in (a) 1989 February, and (b) 1991 January. Contours are 5, 10, 20,..., 90, 95 per cent of the peak intensity.

ES

de 5 m
struments
pour
du ciel.
avoir
aux
le nous,
s.

çonnés de la
ie des étoiles
tous les gros
sent actuelle-
LT européen,
illiard de F,
onfrère orbi-
ds miroirs de
de collecter
aire travailler





Keck Pupil Mask

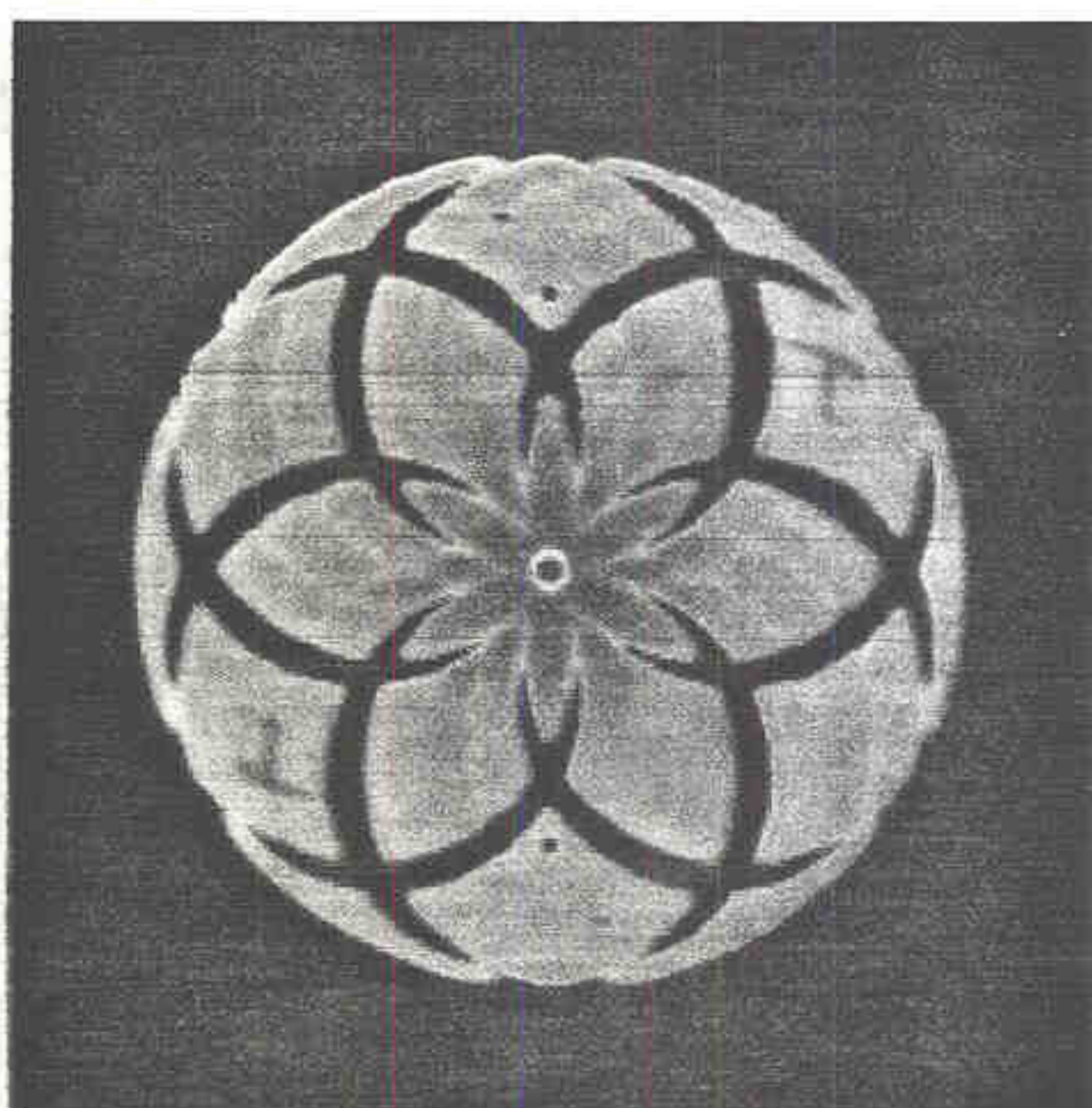
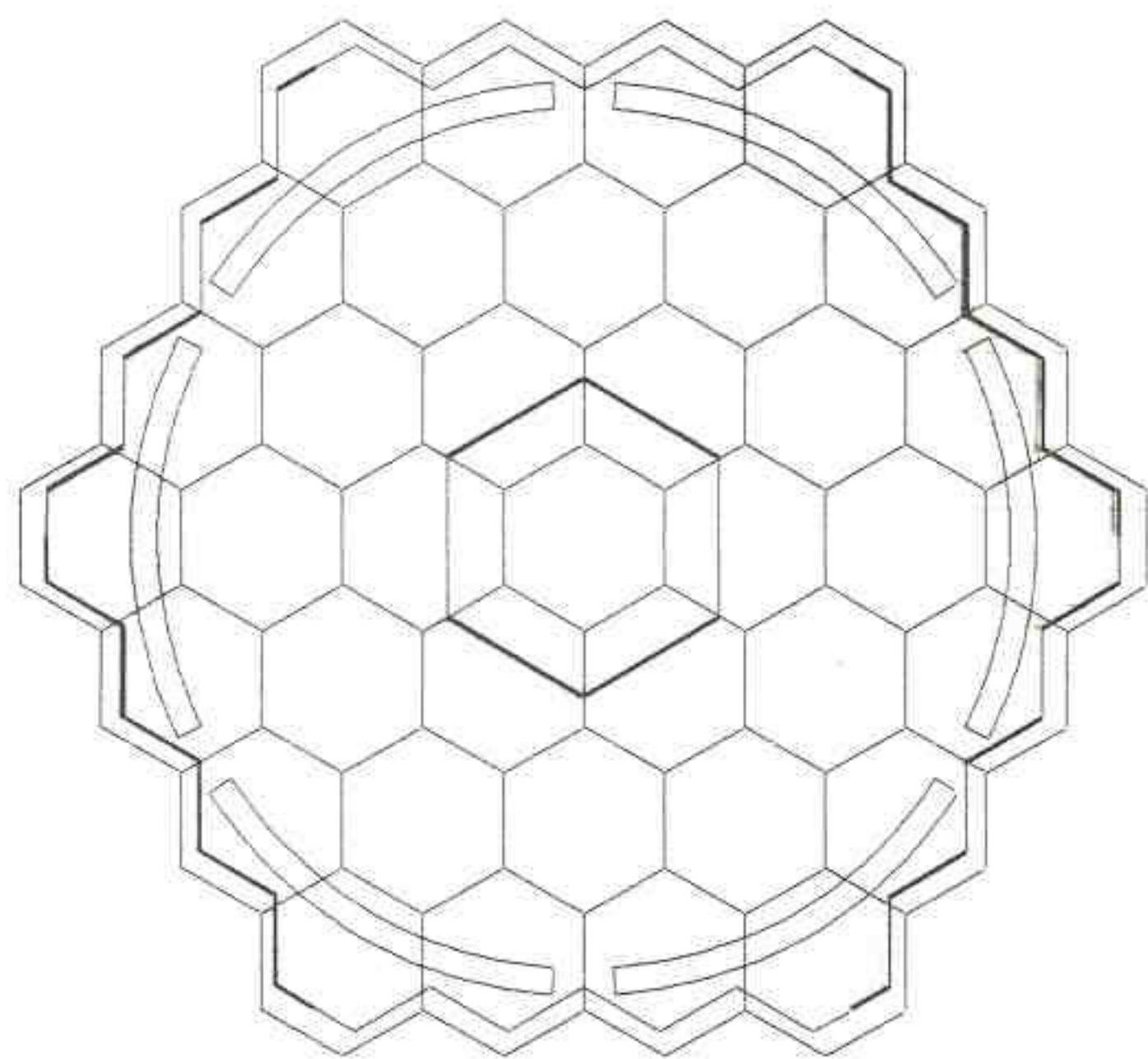
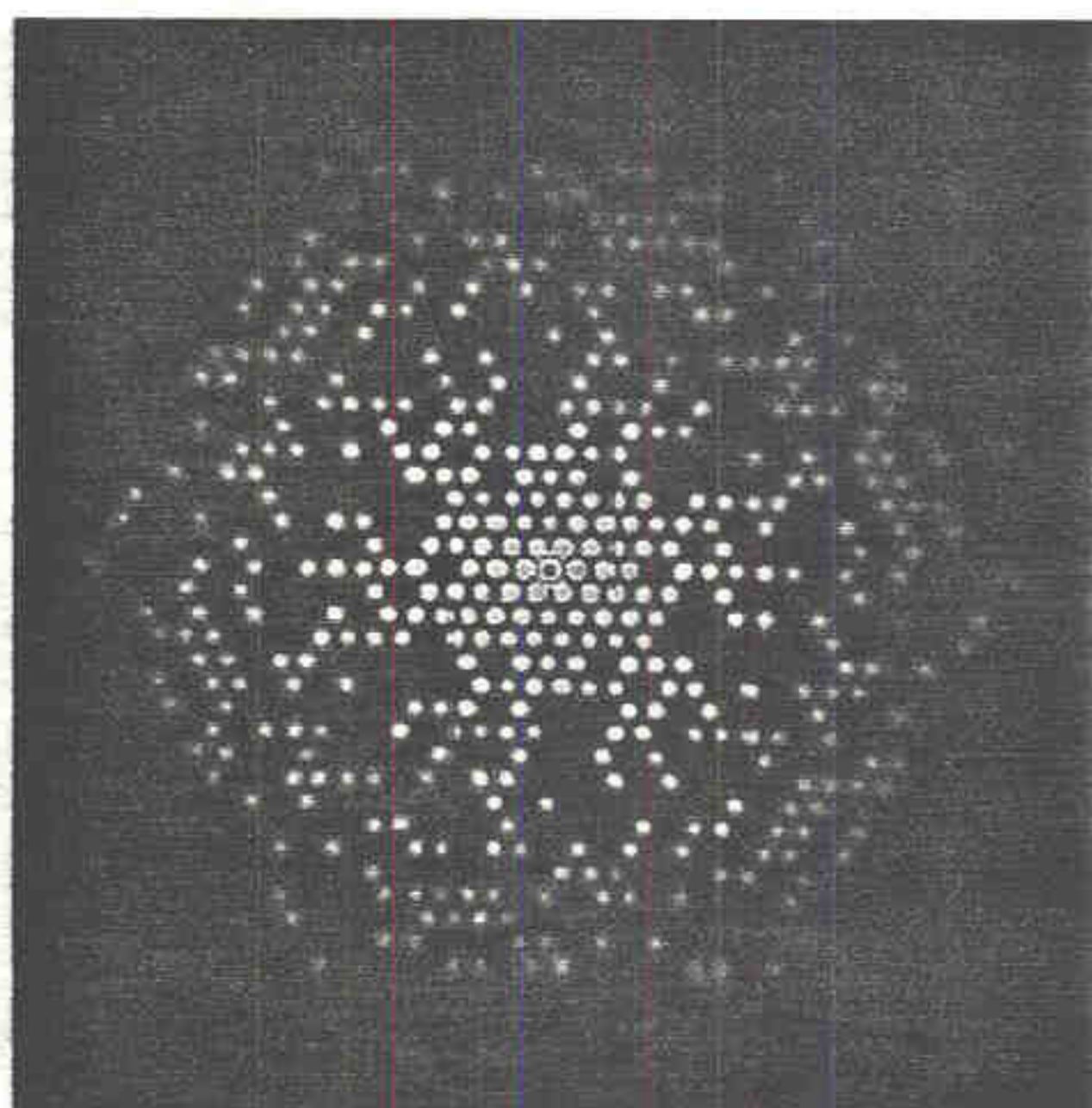
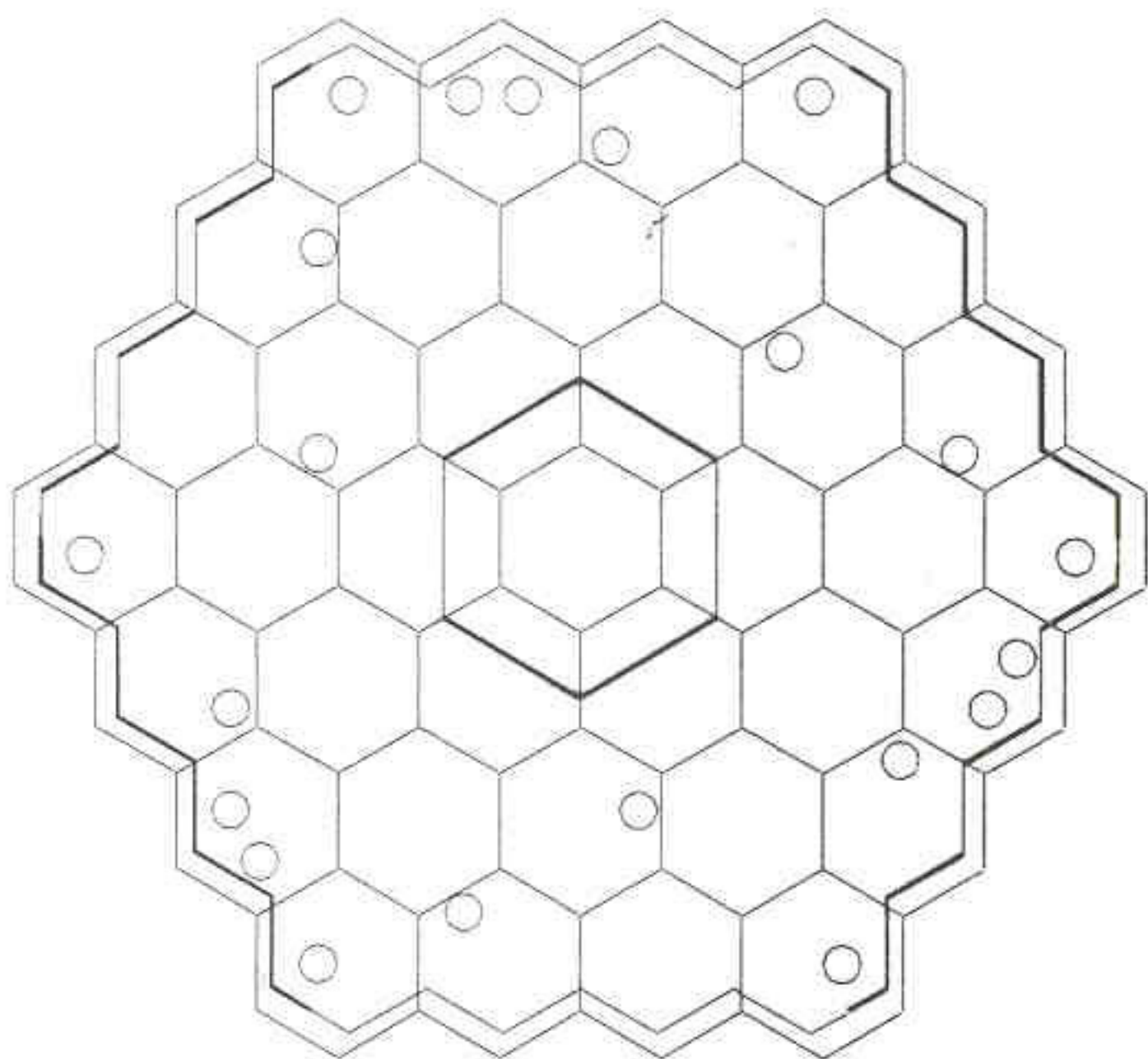
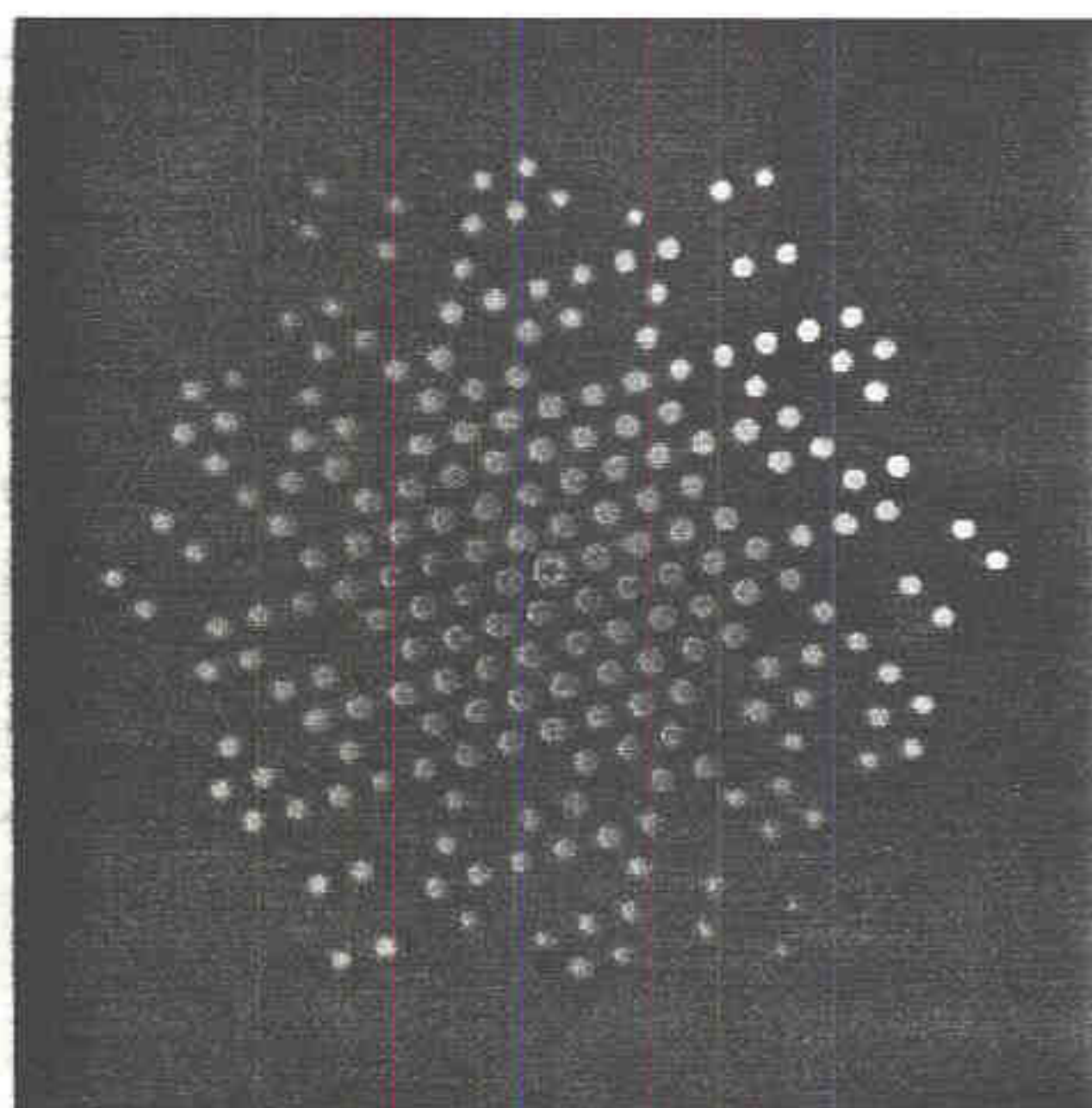
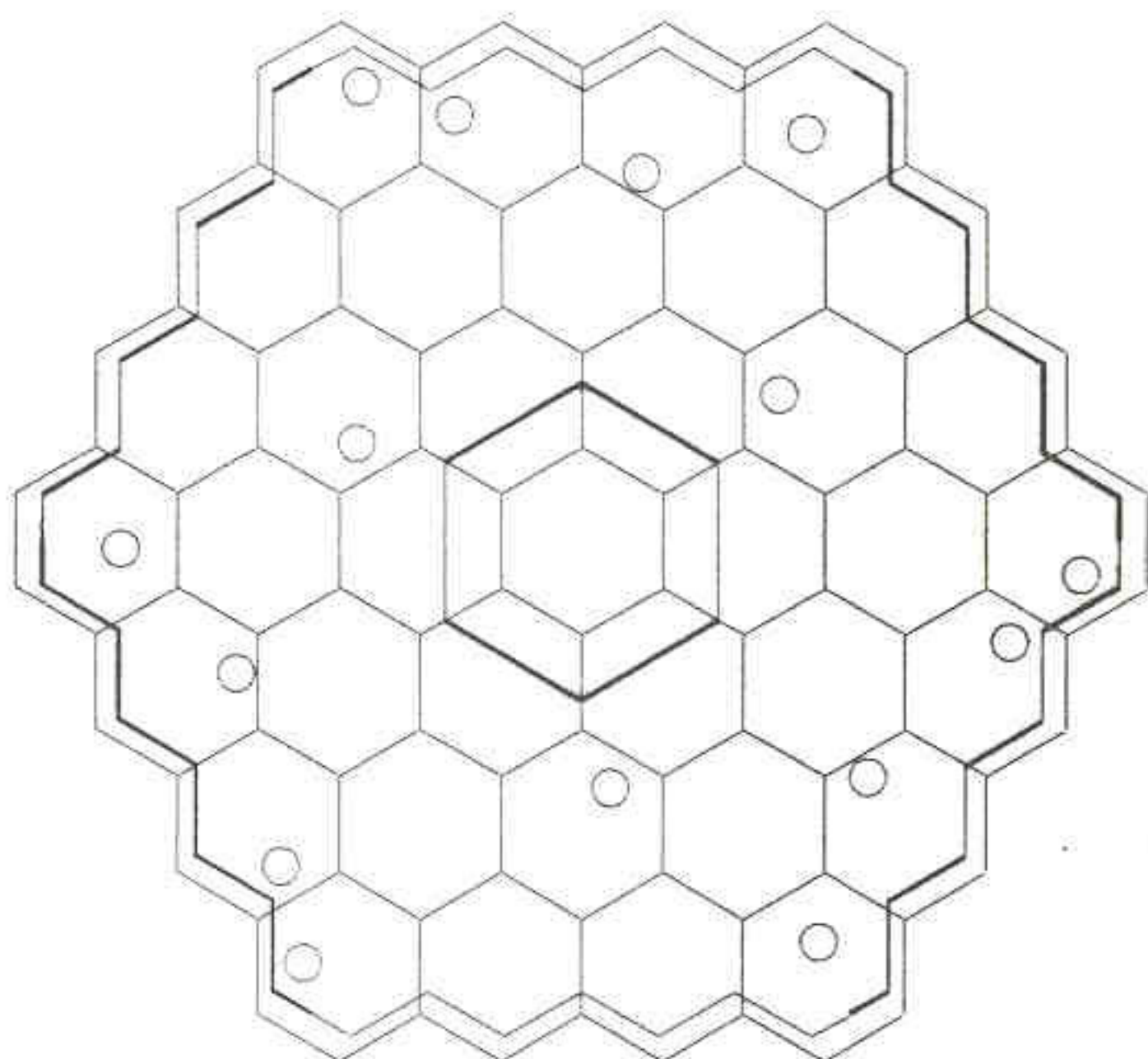
DRAWN BY: Peter Tuthill

DATE: 25-Feb-97

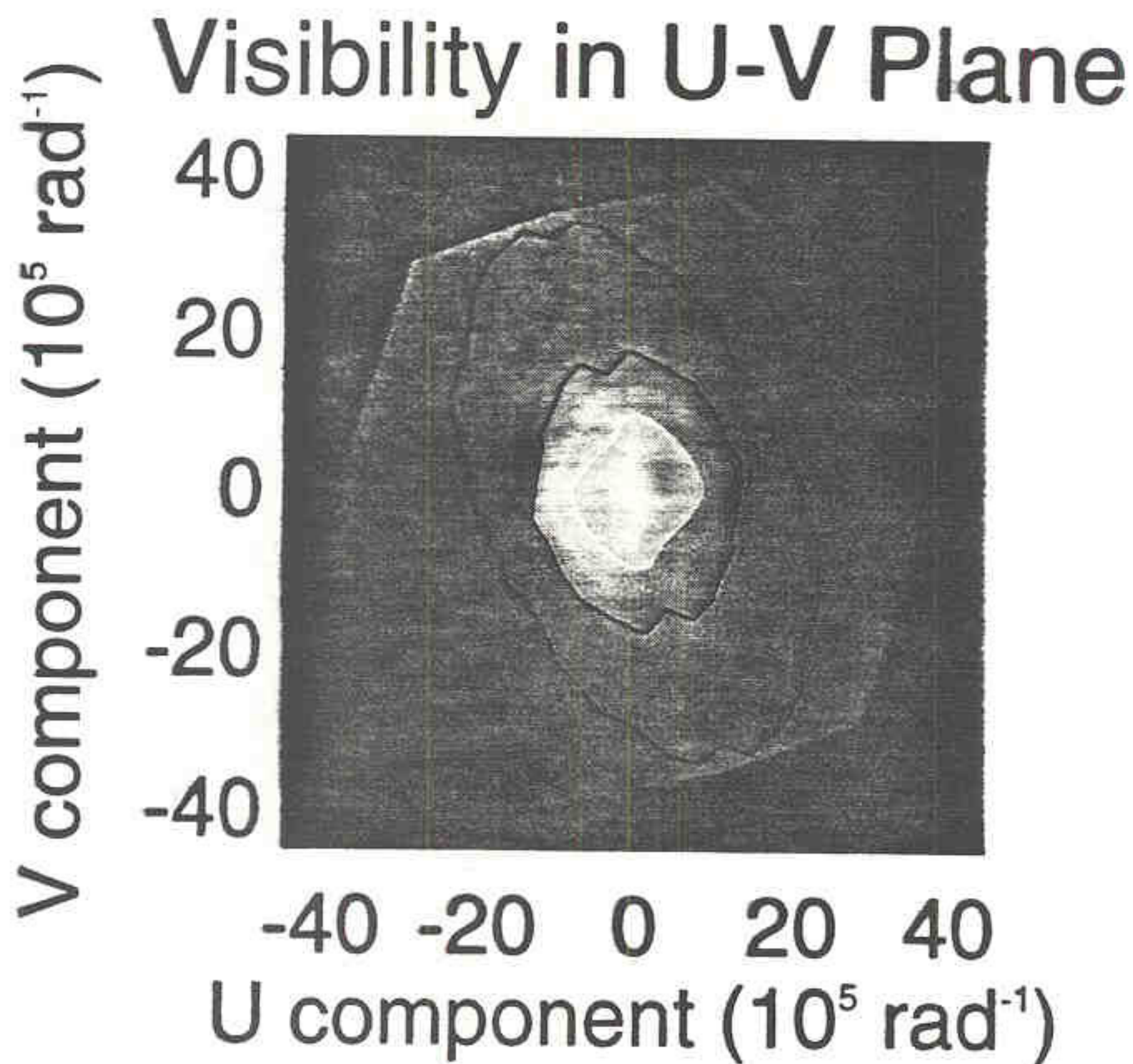
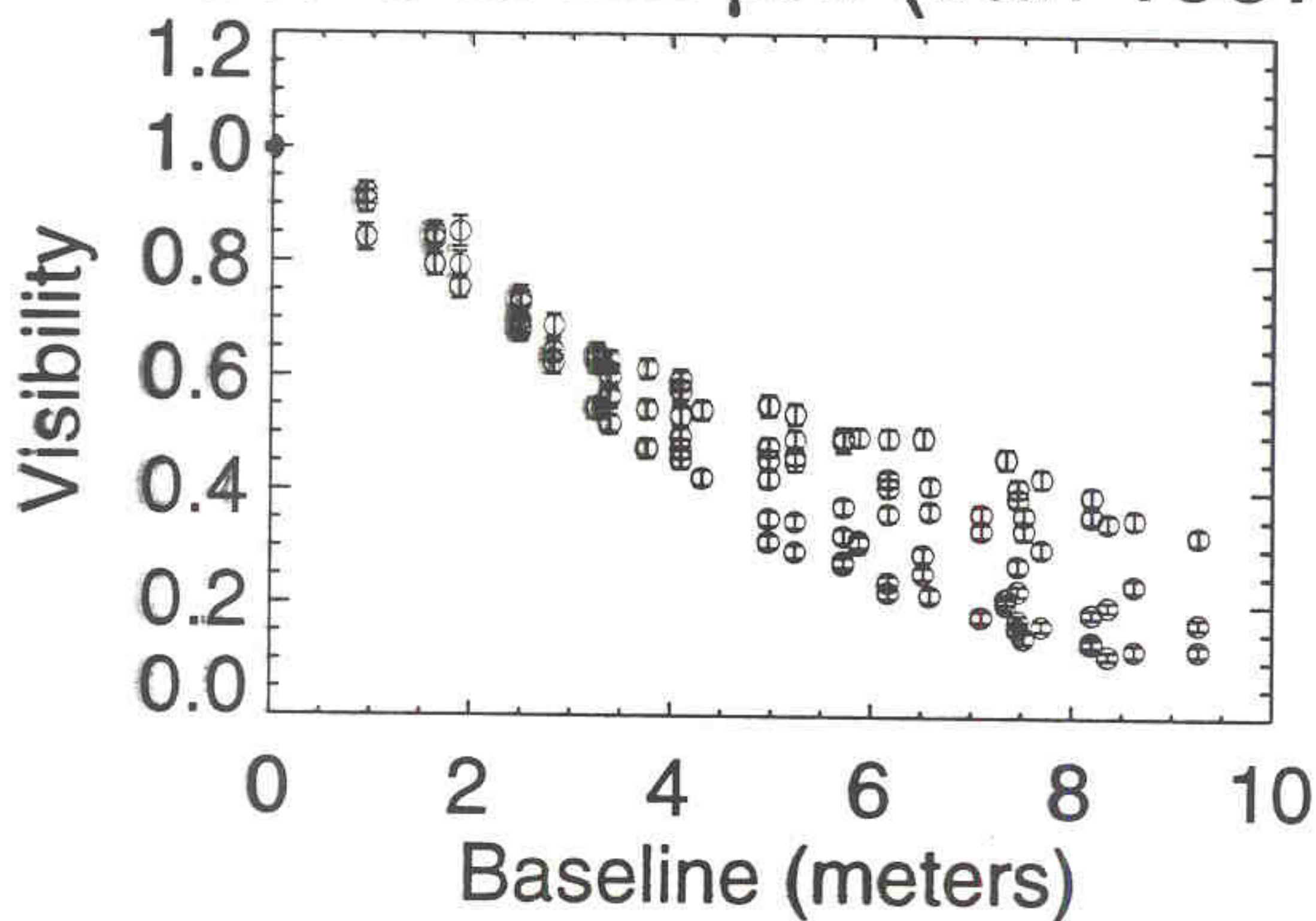
SCALE: 1:50

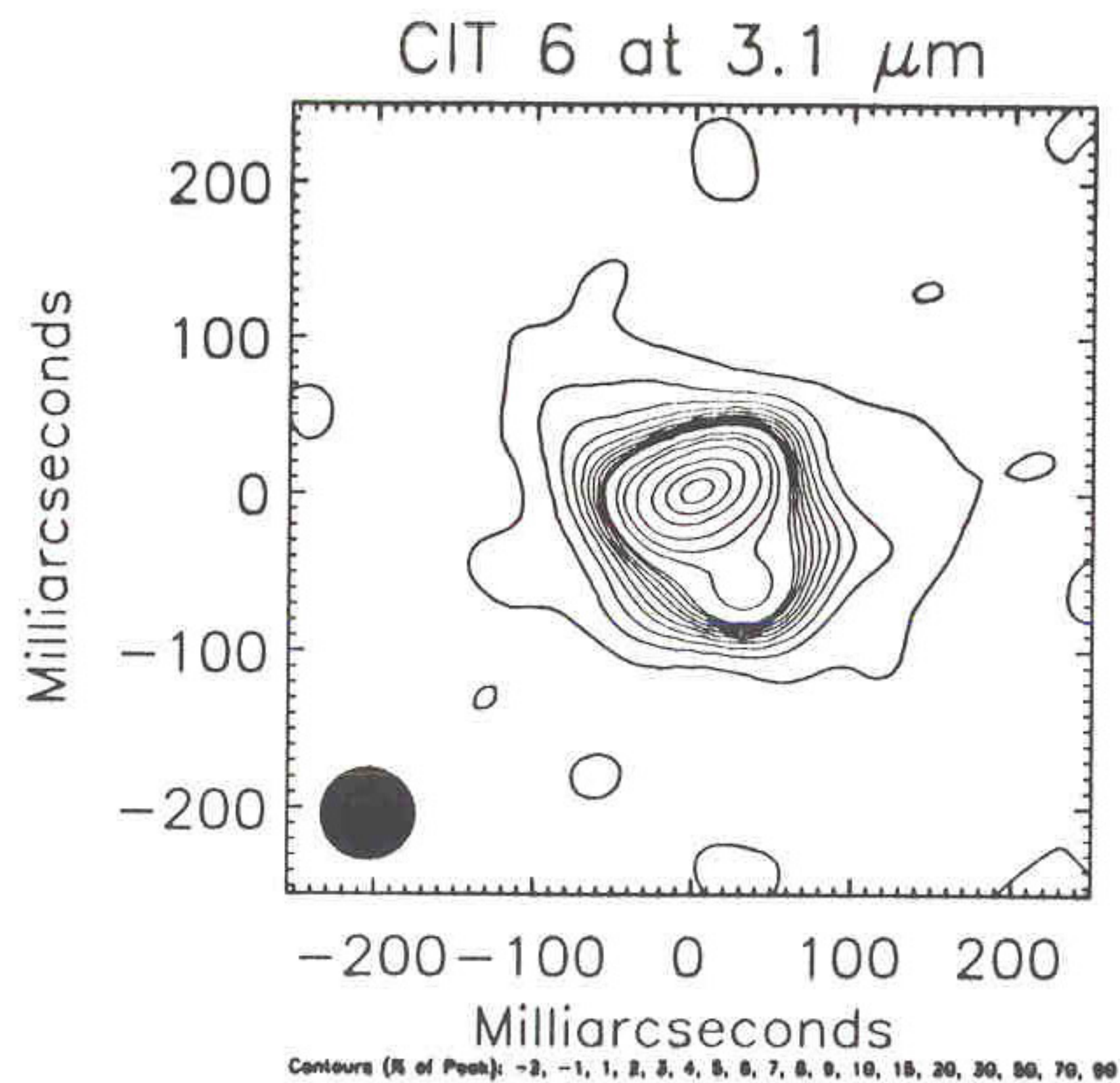
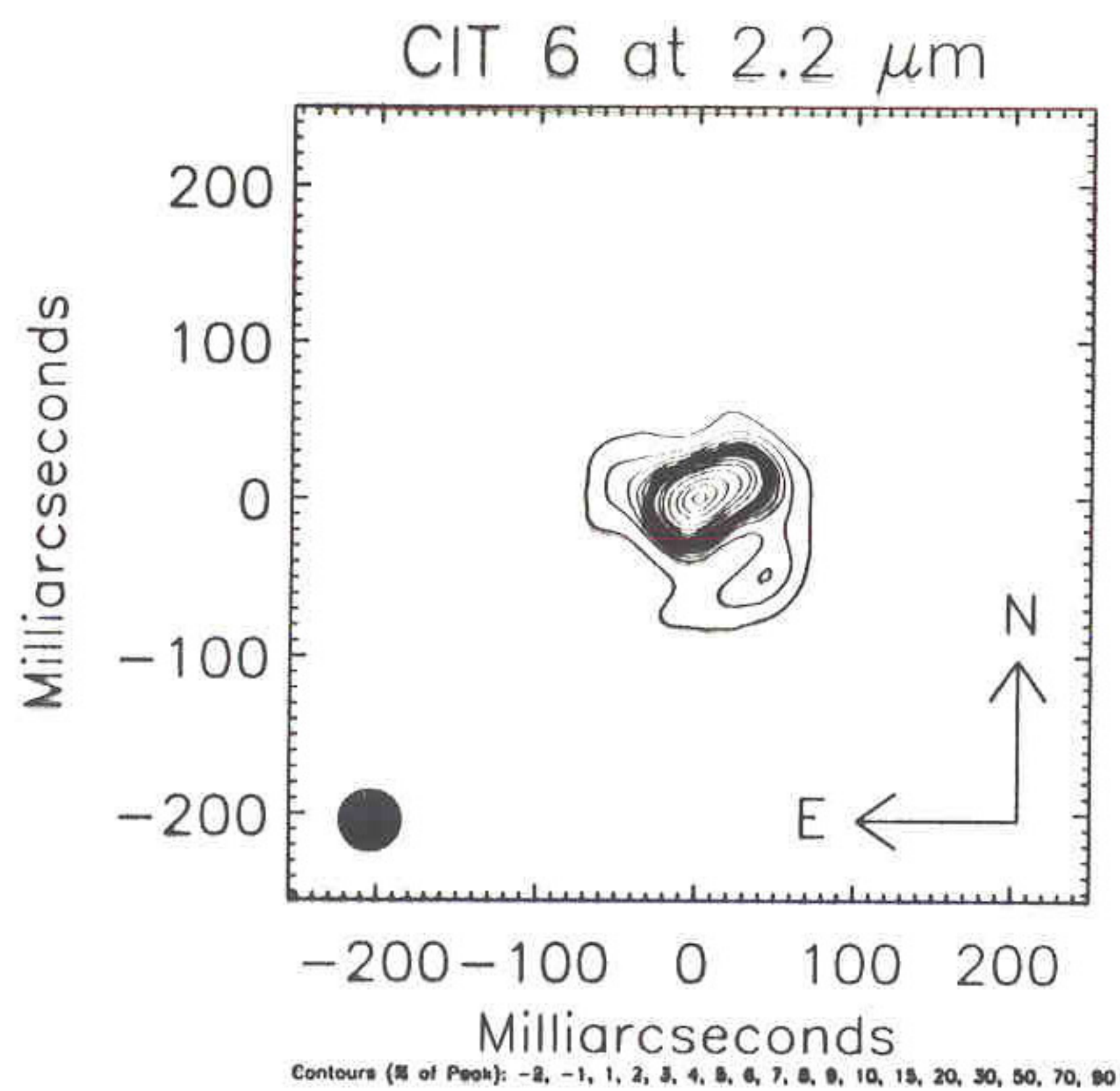
MATERIAL: Aluminum

15 Hole Golay (35cm holes)

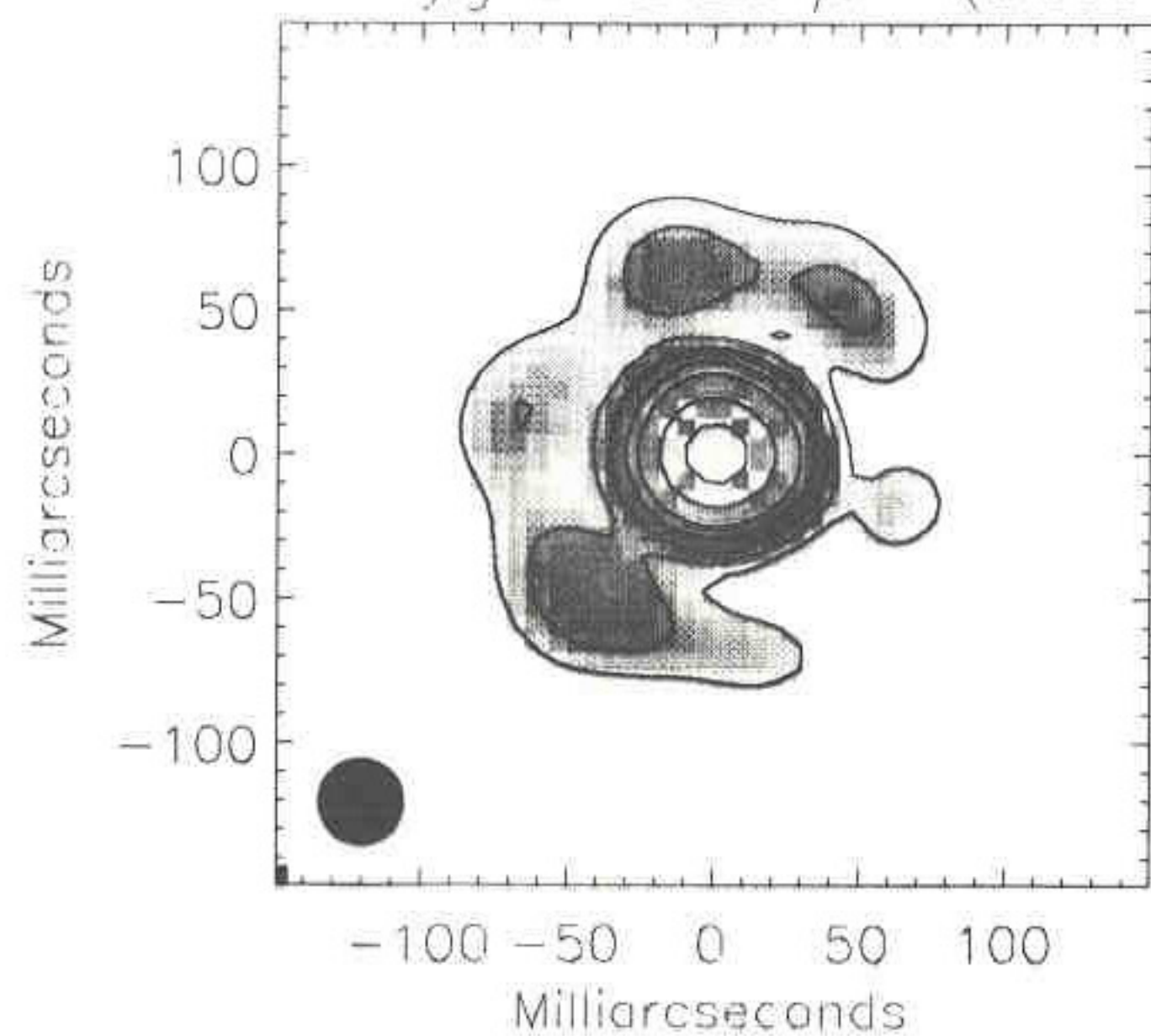


CIT 6 at 2.2 μm (Jan 1997)

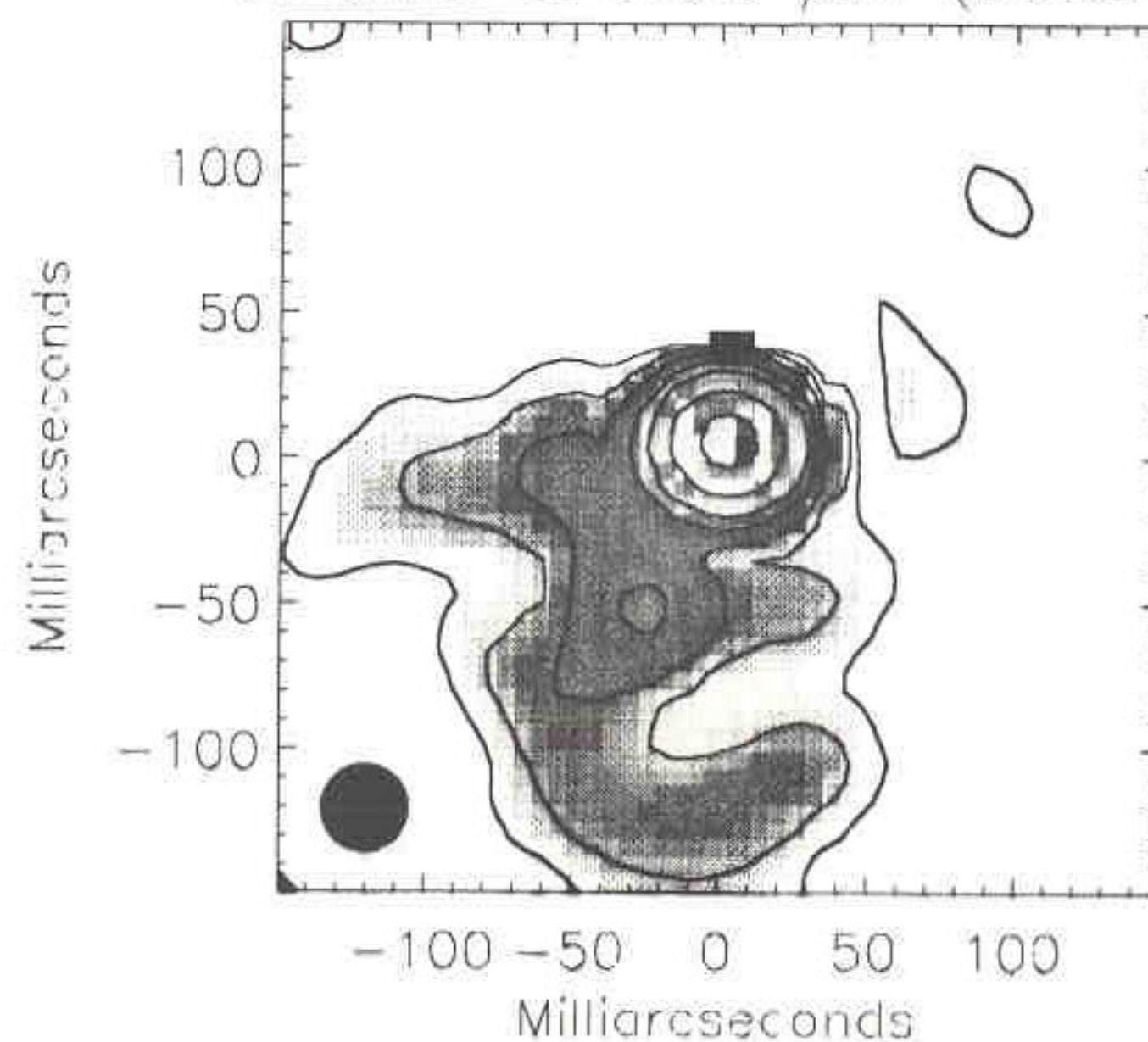




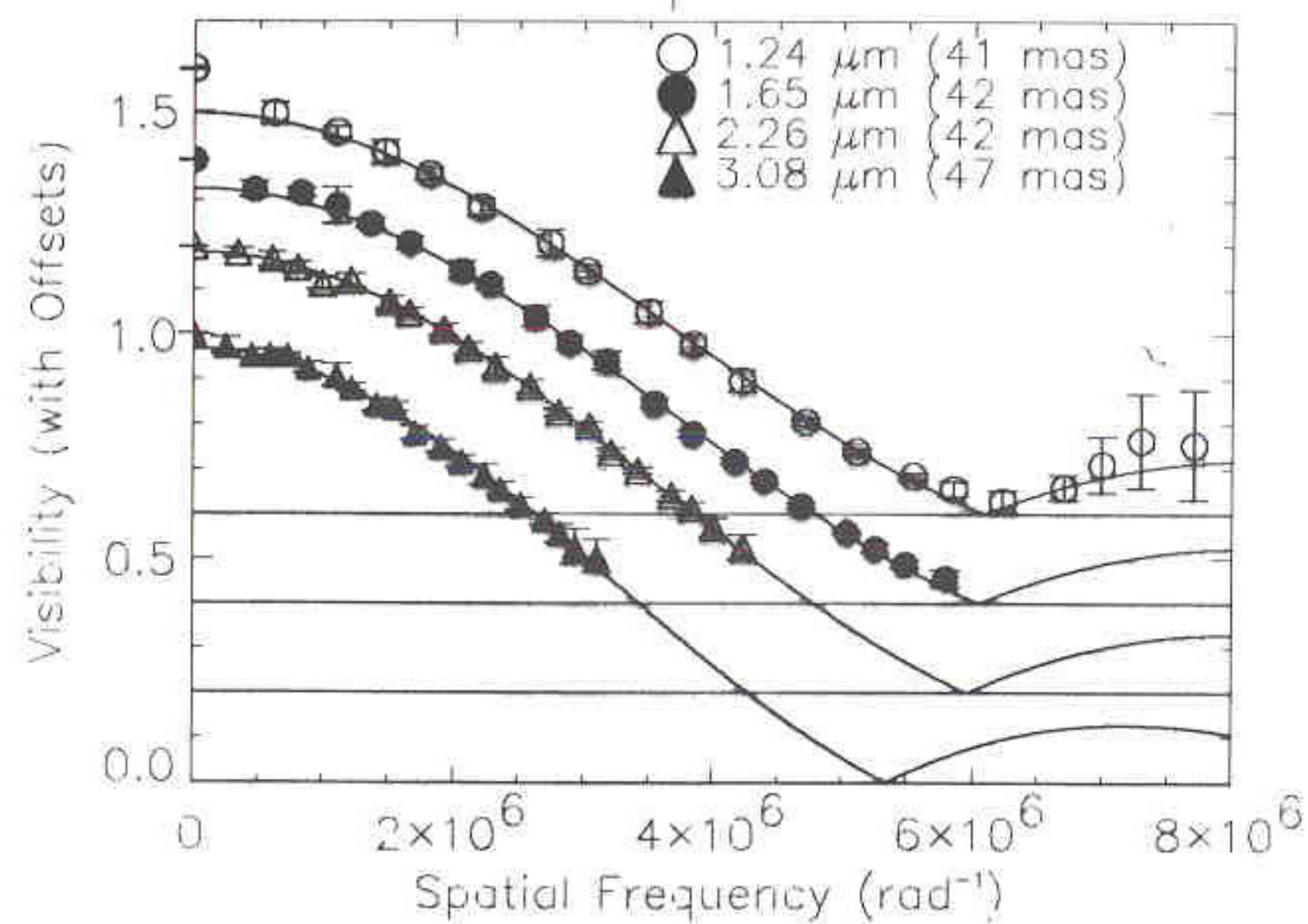
NML Cyg at $2.26 \mu\text{m}$ (Dec97)



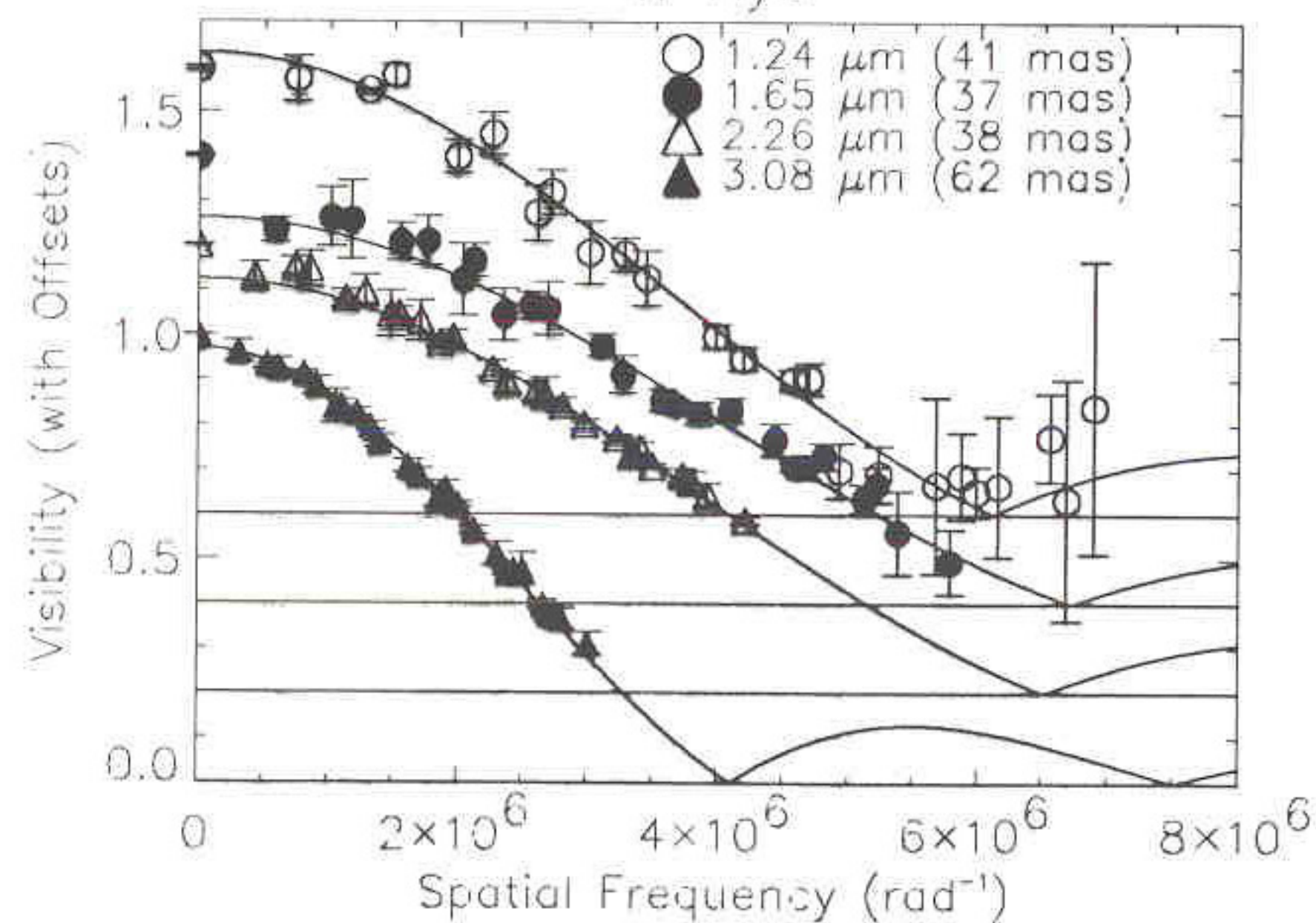
VY CMa at $2.26 \mu\text{m}$ (Dec97)



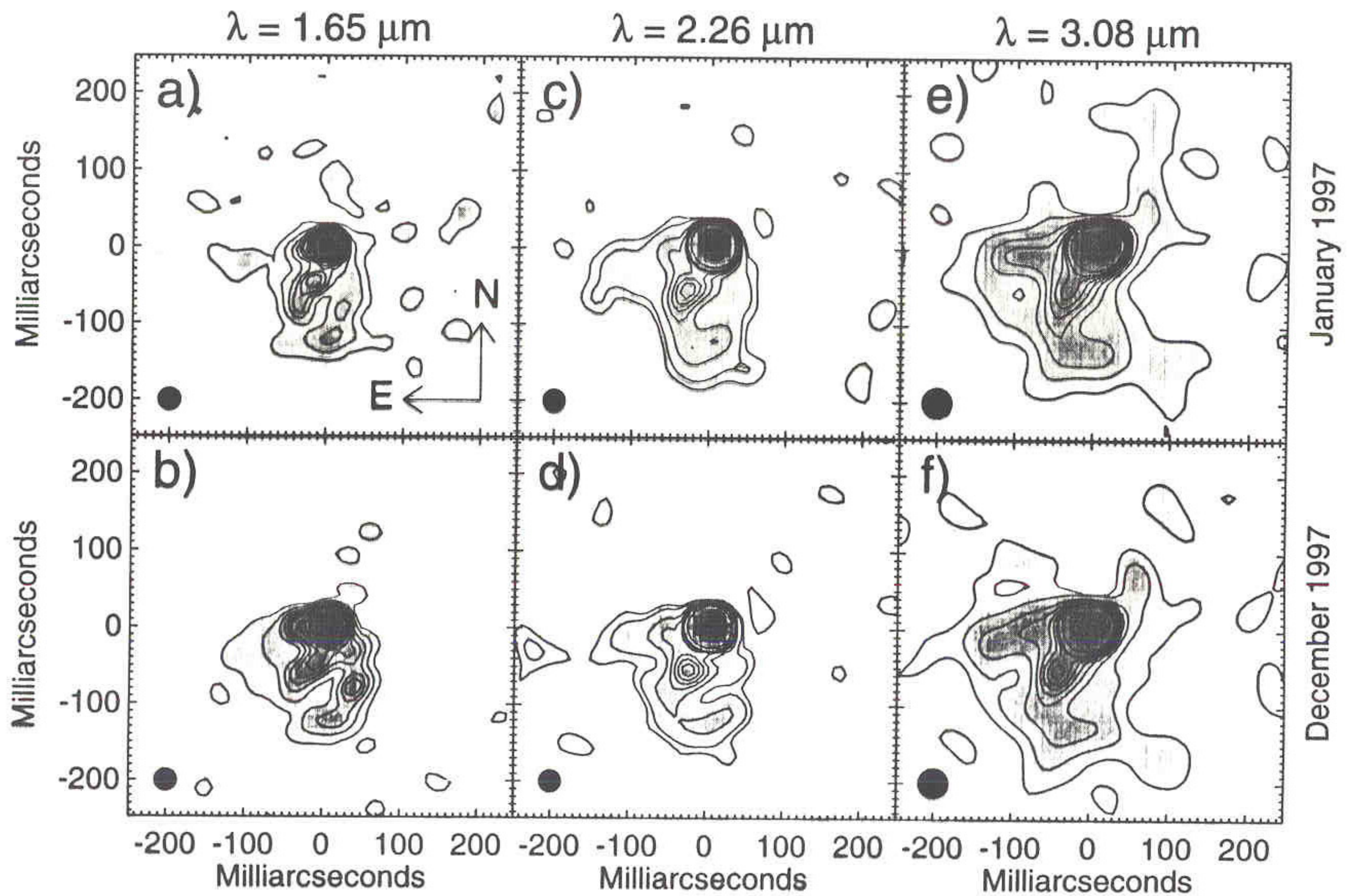
Alp Ori



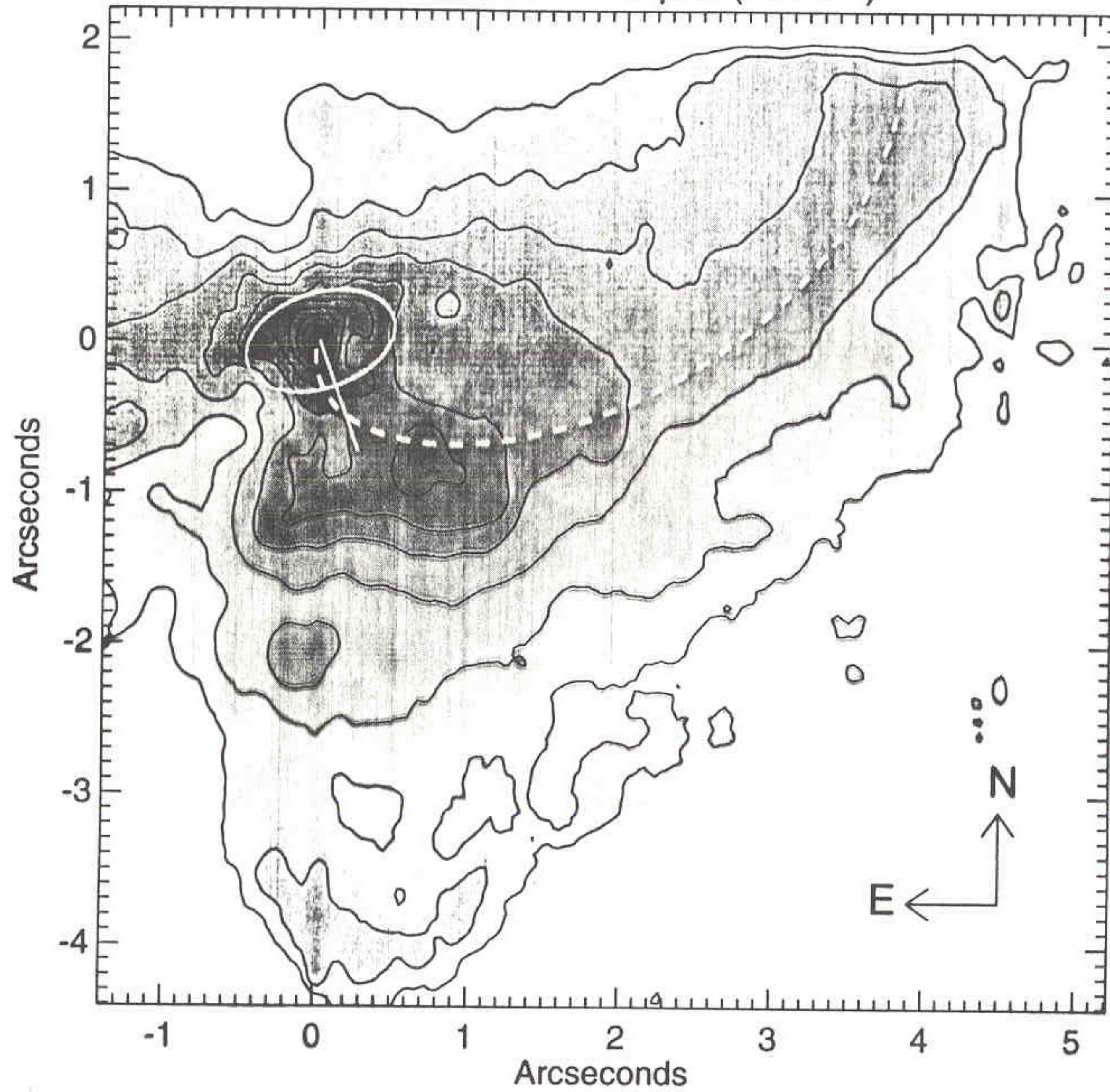
W Hya



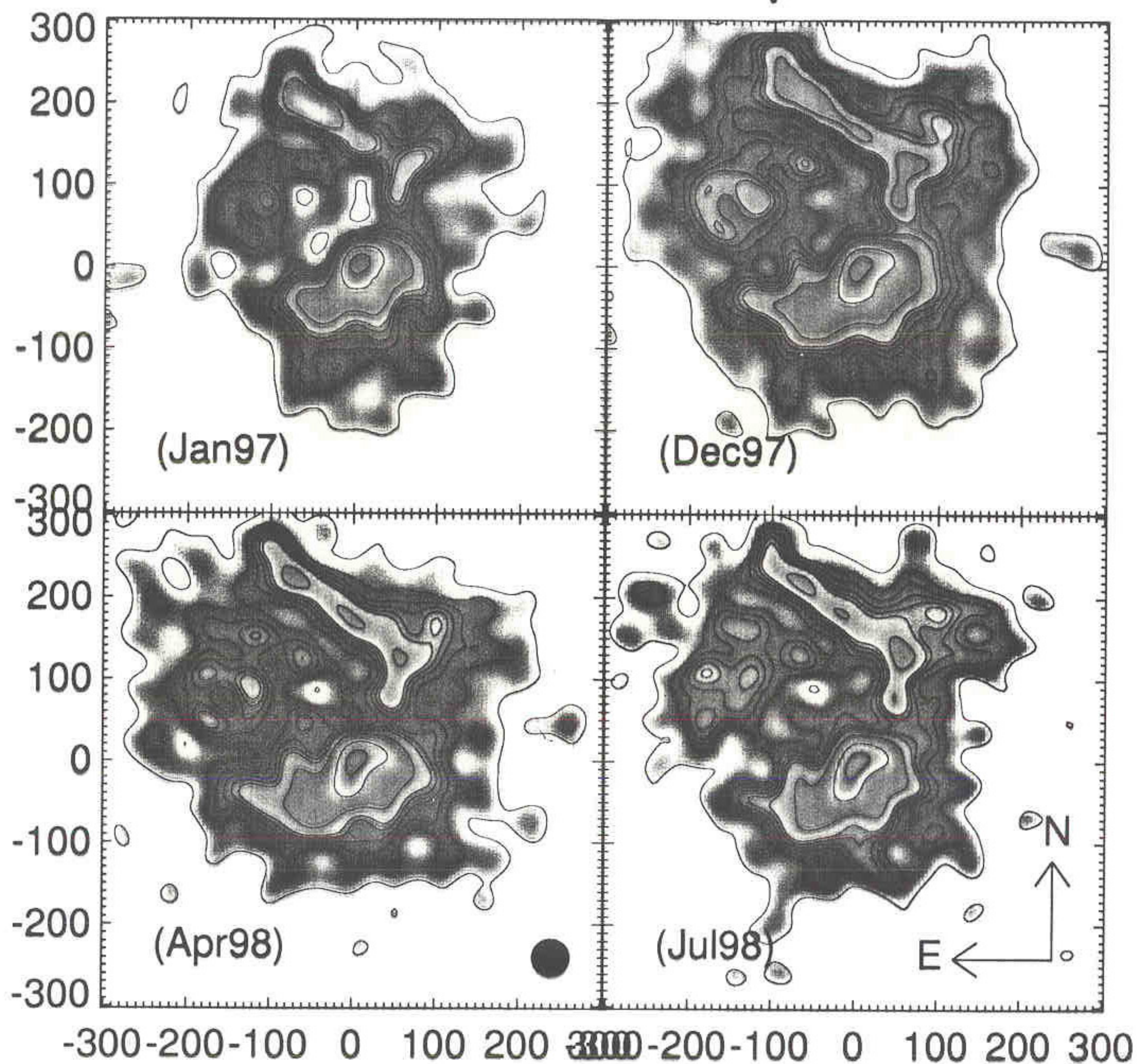
VY CMa



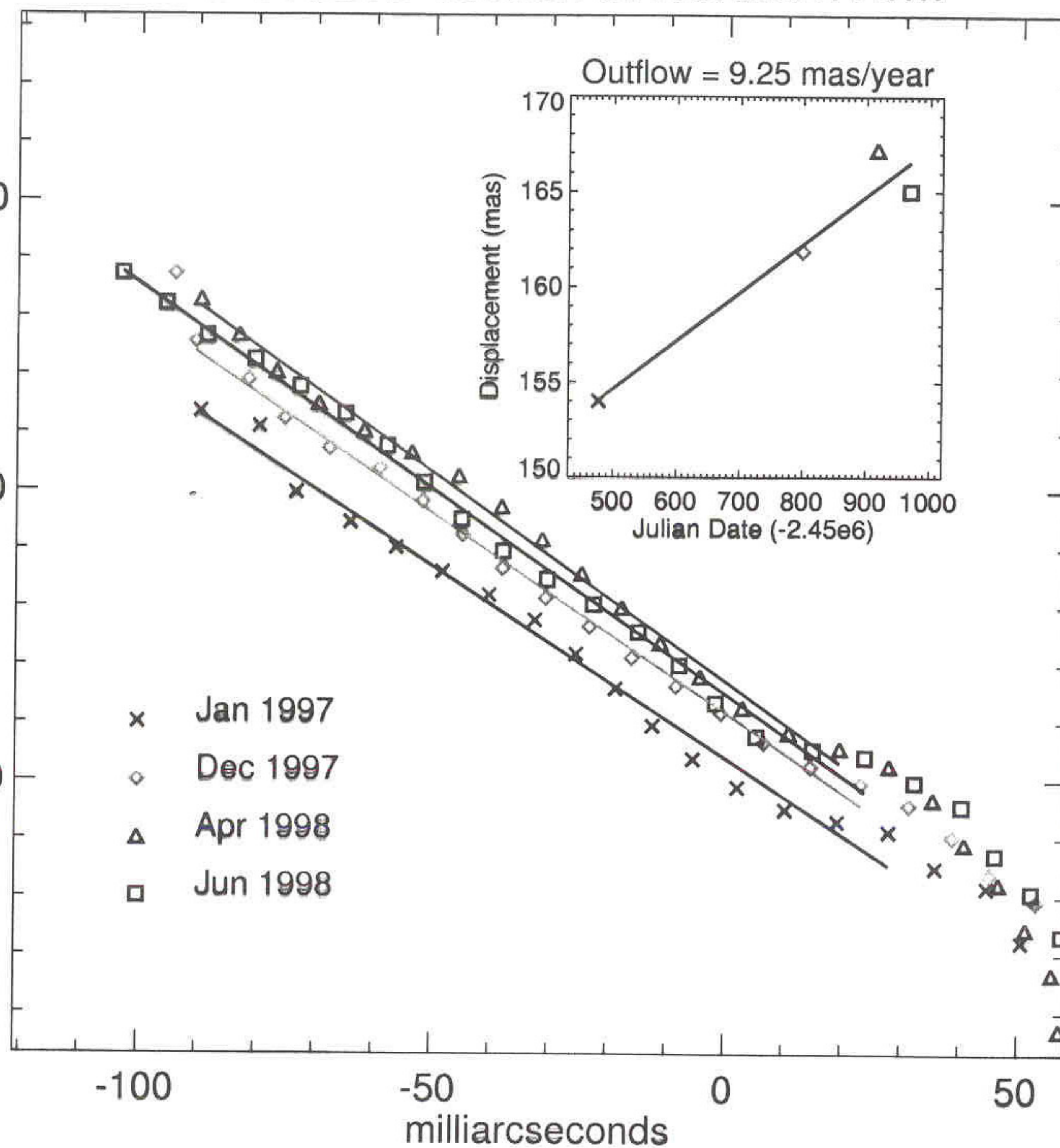
VY CMa at 1.25 μm (Dec96)



IRC +10216 at 2.2 μm



Contours (% of Peak): 1. 2. 3. 4. 5. 6. 10. 30. 70.

[illegible]

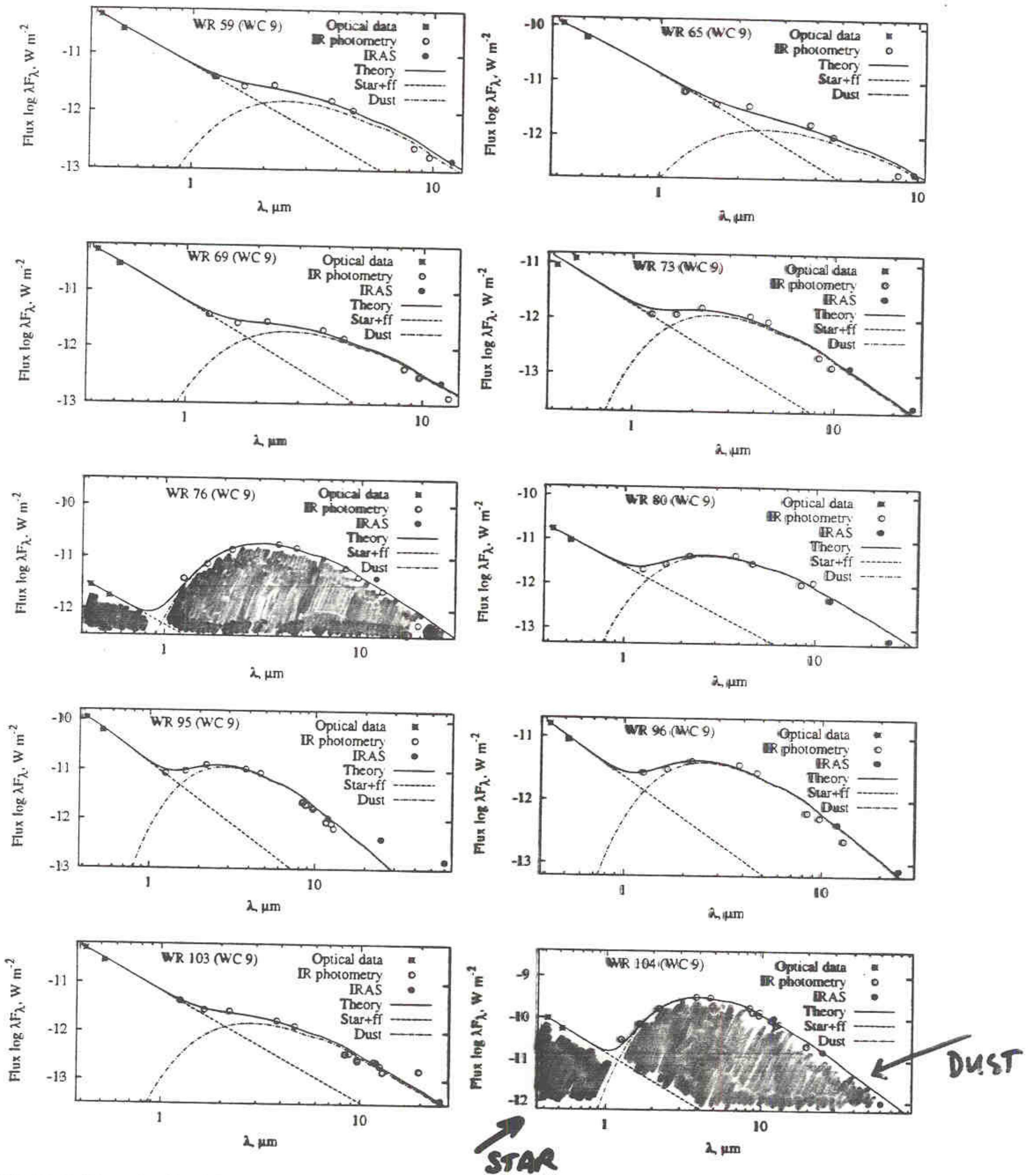
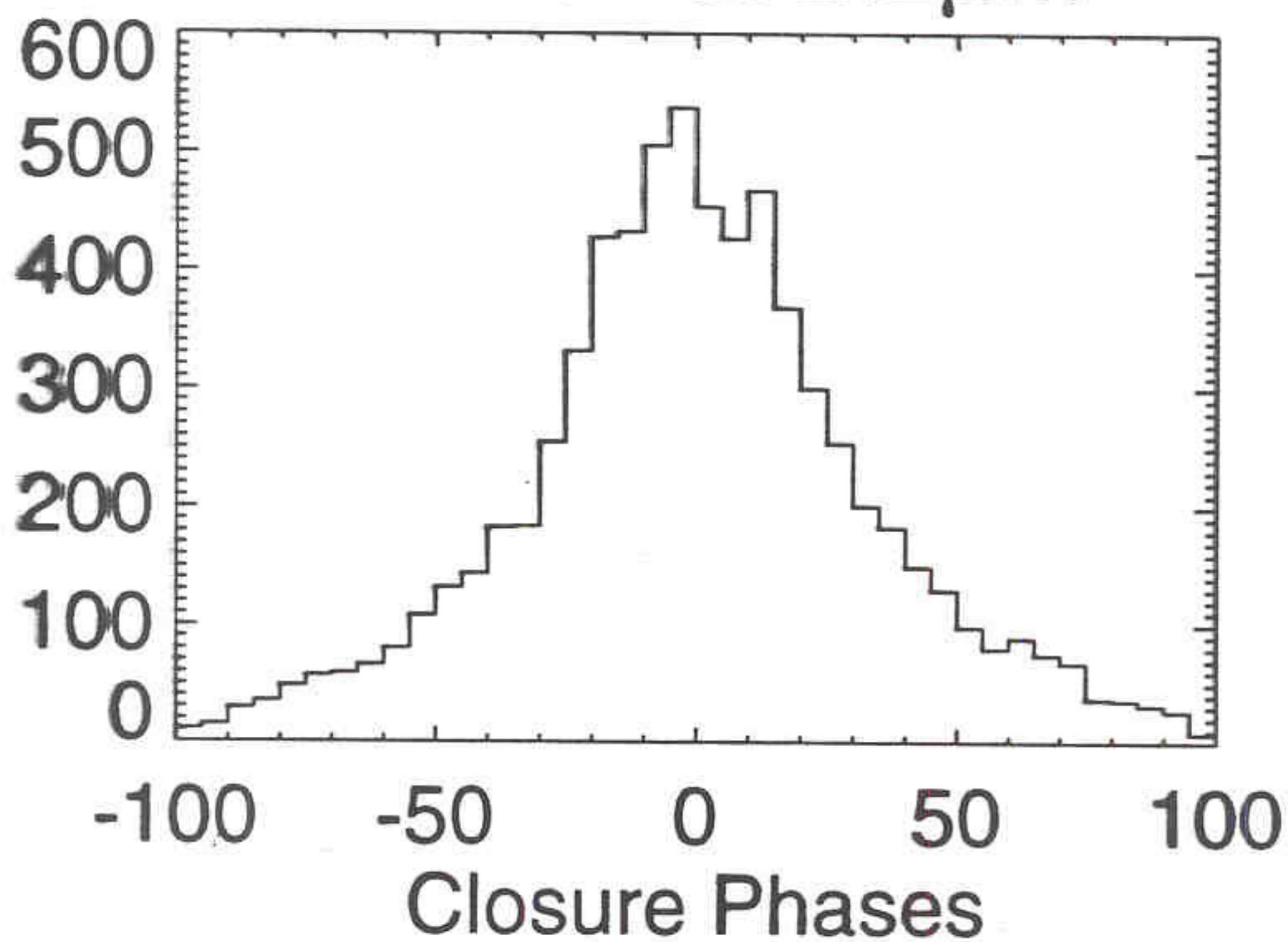
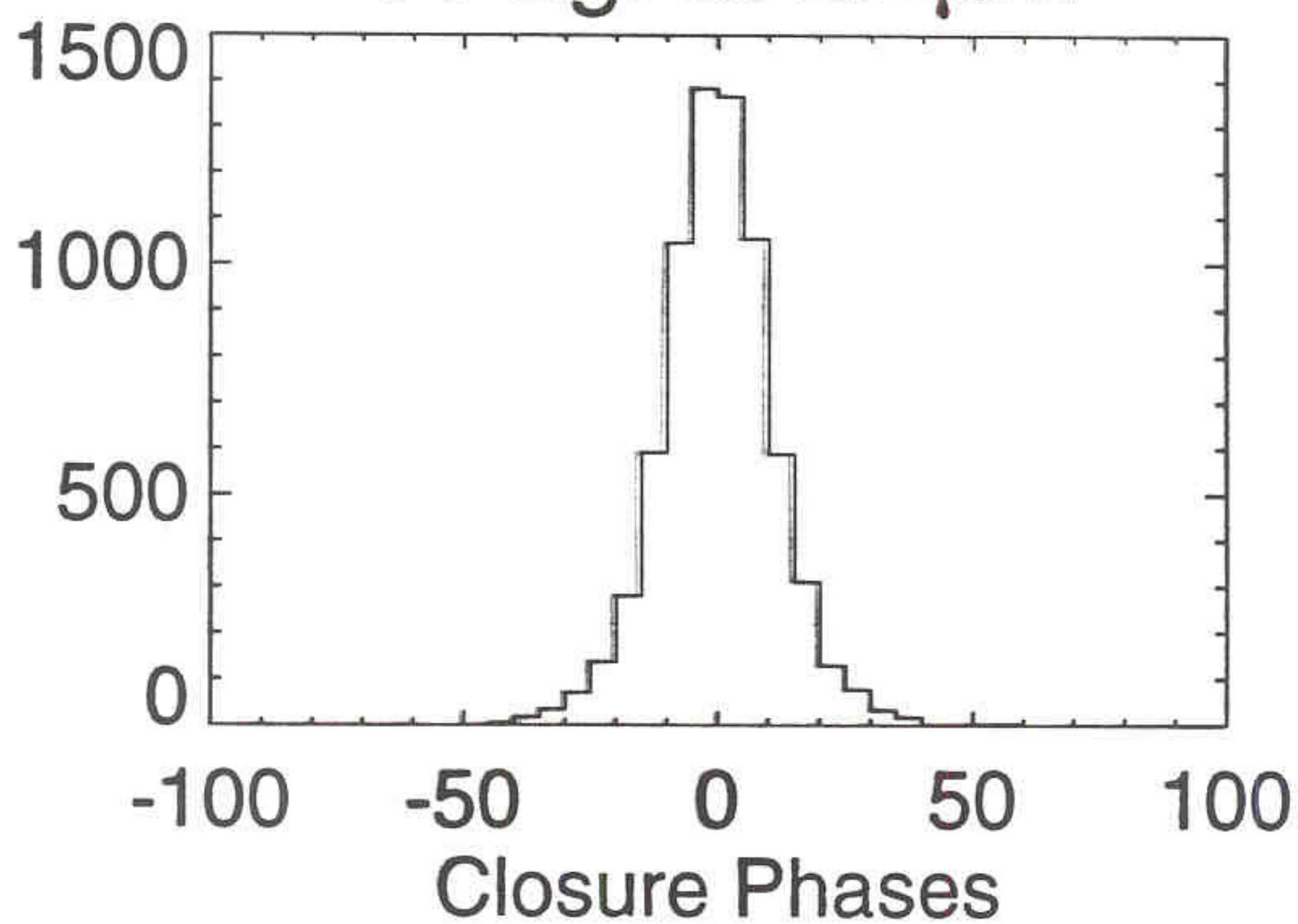


Figure 2. Observational and theoretical energy distributions of WR stars. The observational data are marked by asterisks (optical photometry), open circles (ground-based IR photometry) and filled circles (IRAS); the model spectra are depicted by solid lines and the contributions of 'star+wind' and dust emission by dashed and dot-dashed lines, respectively.

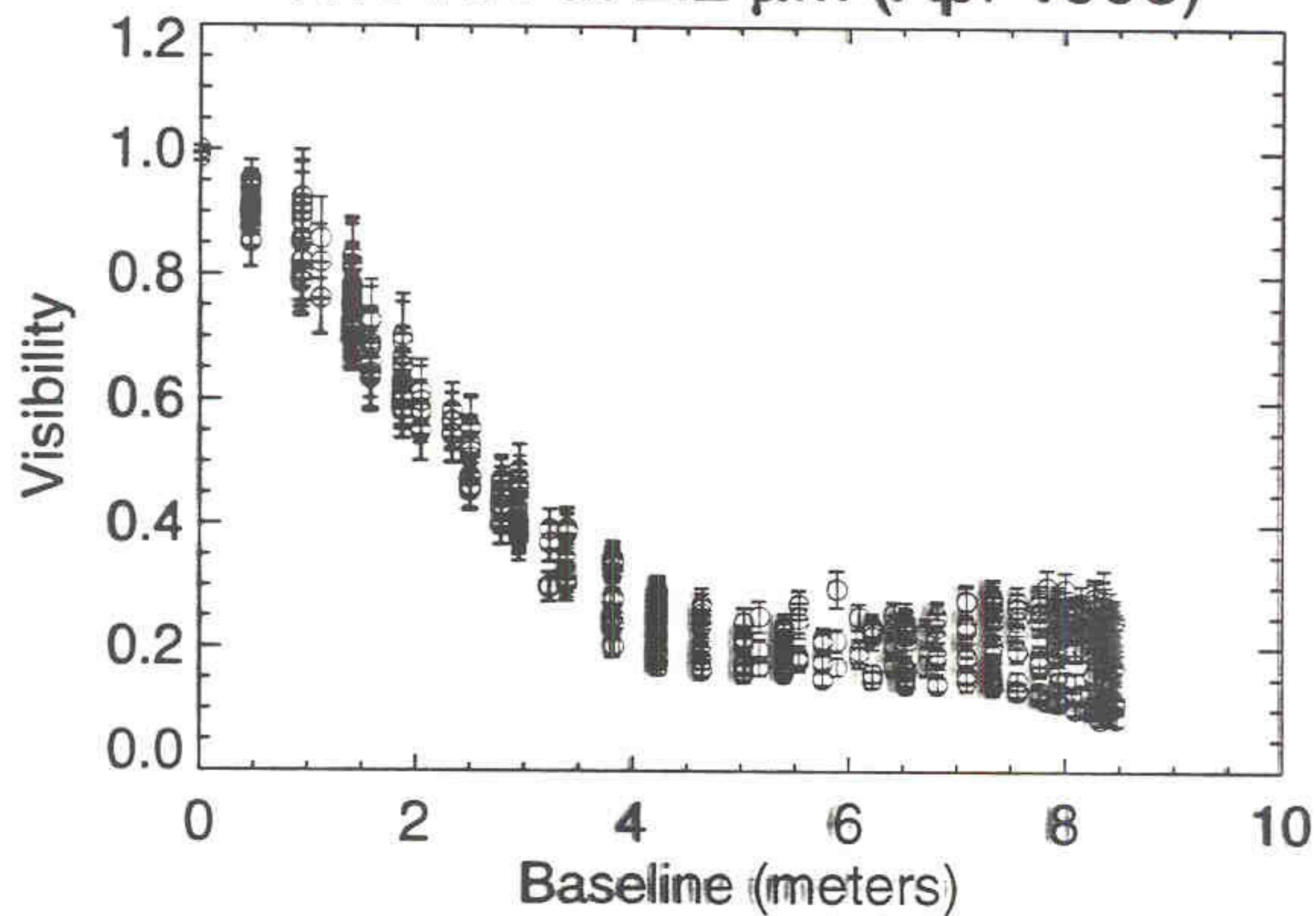
WR104 at $2.2\mu\text{m}$



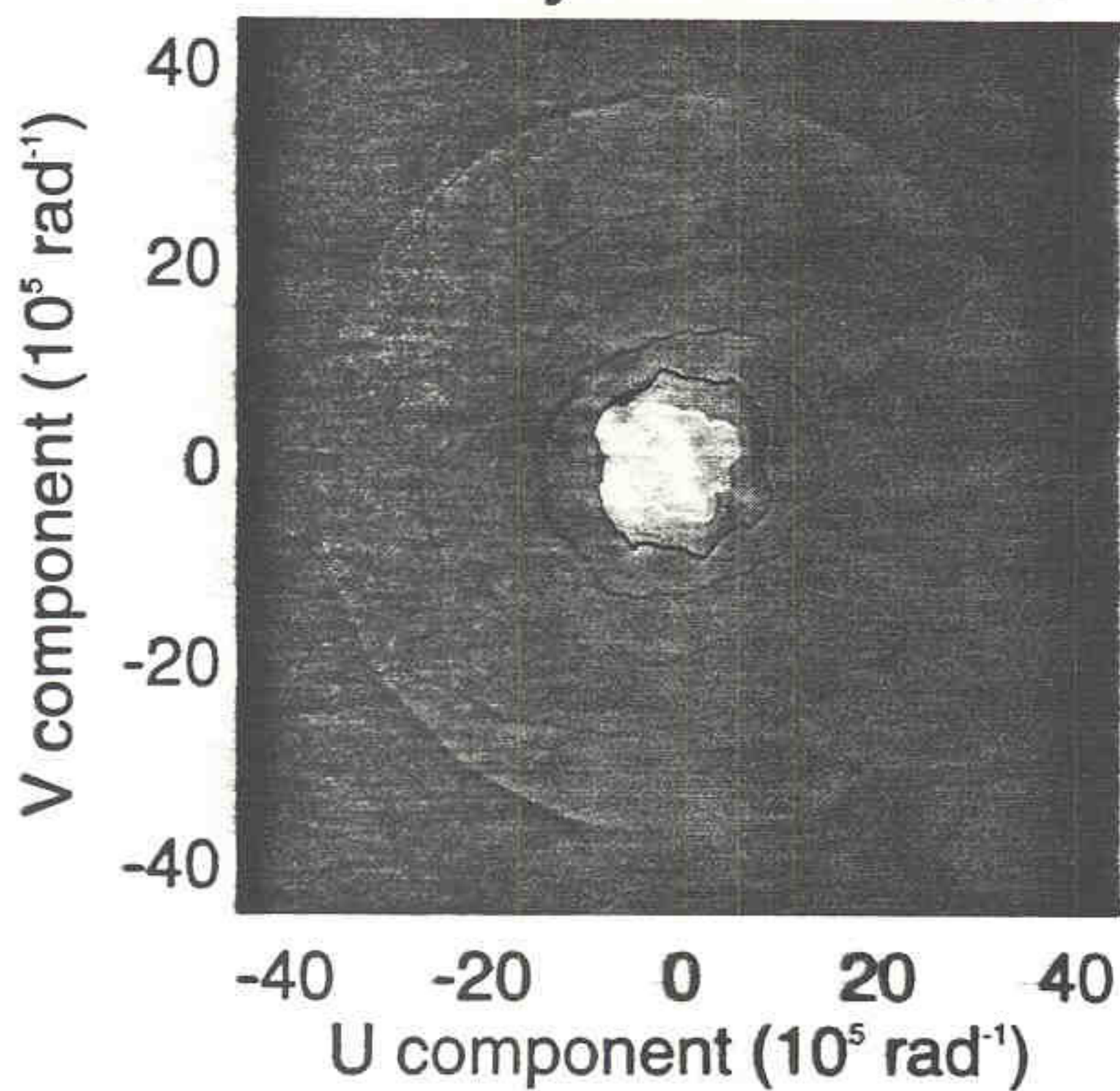
14 Sgr at $2.2\mu\text{m}$



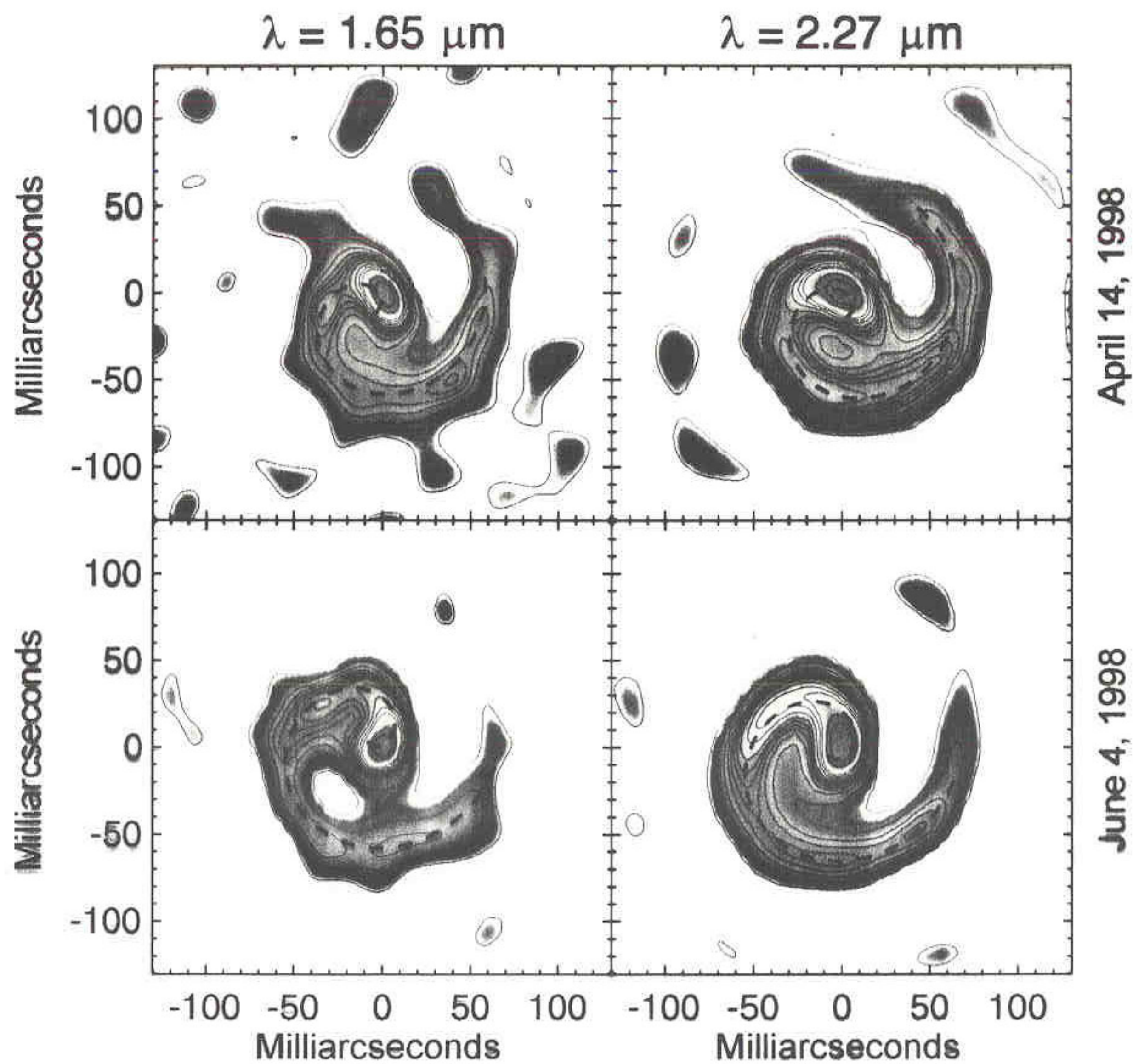
WR 104 at 2.2 μm (Apr 1998)



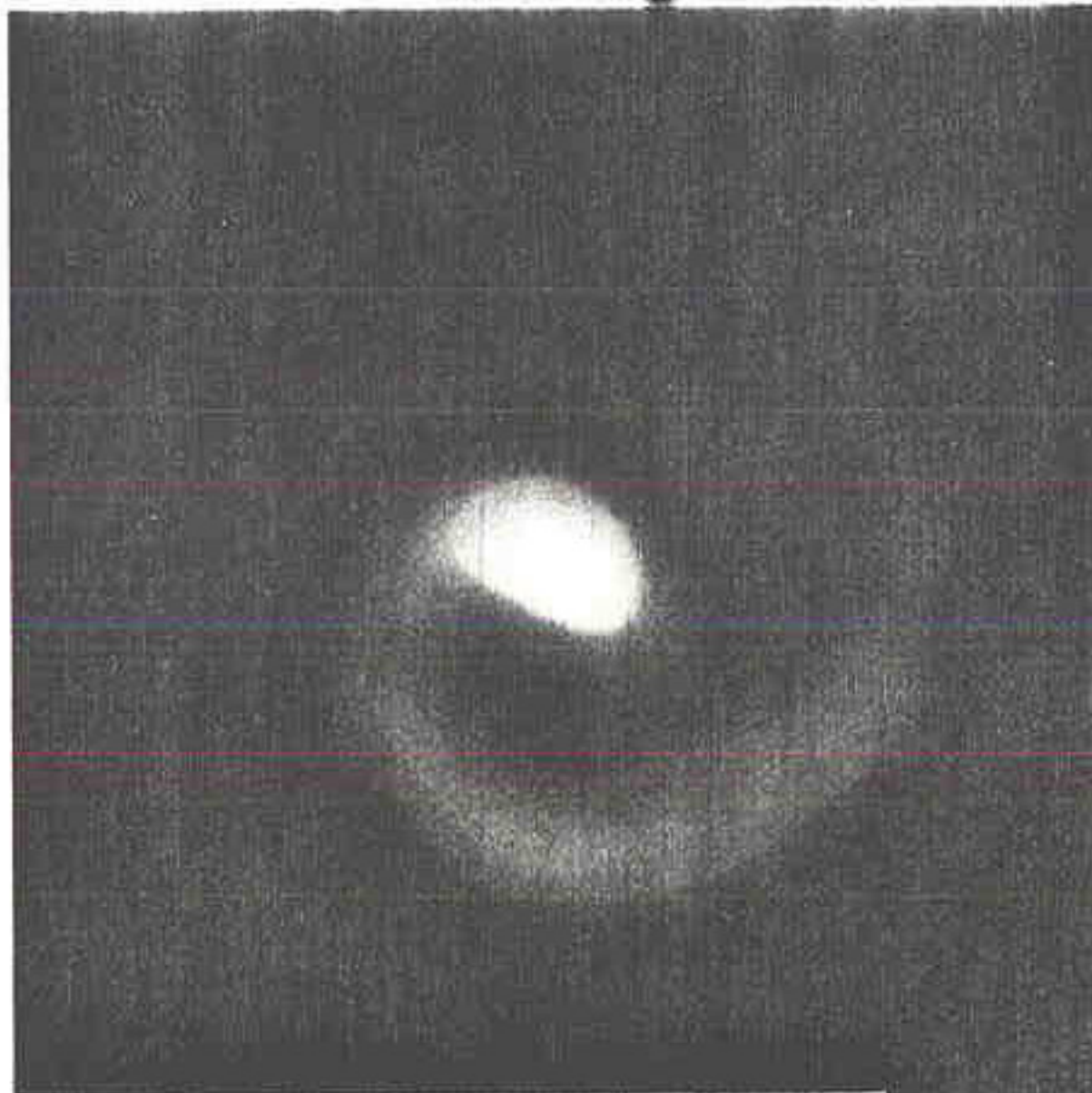
Visibility in U-V Plane



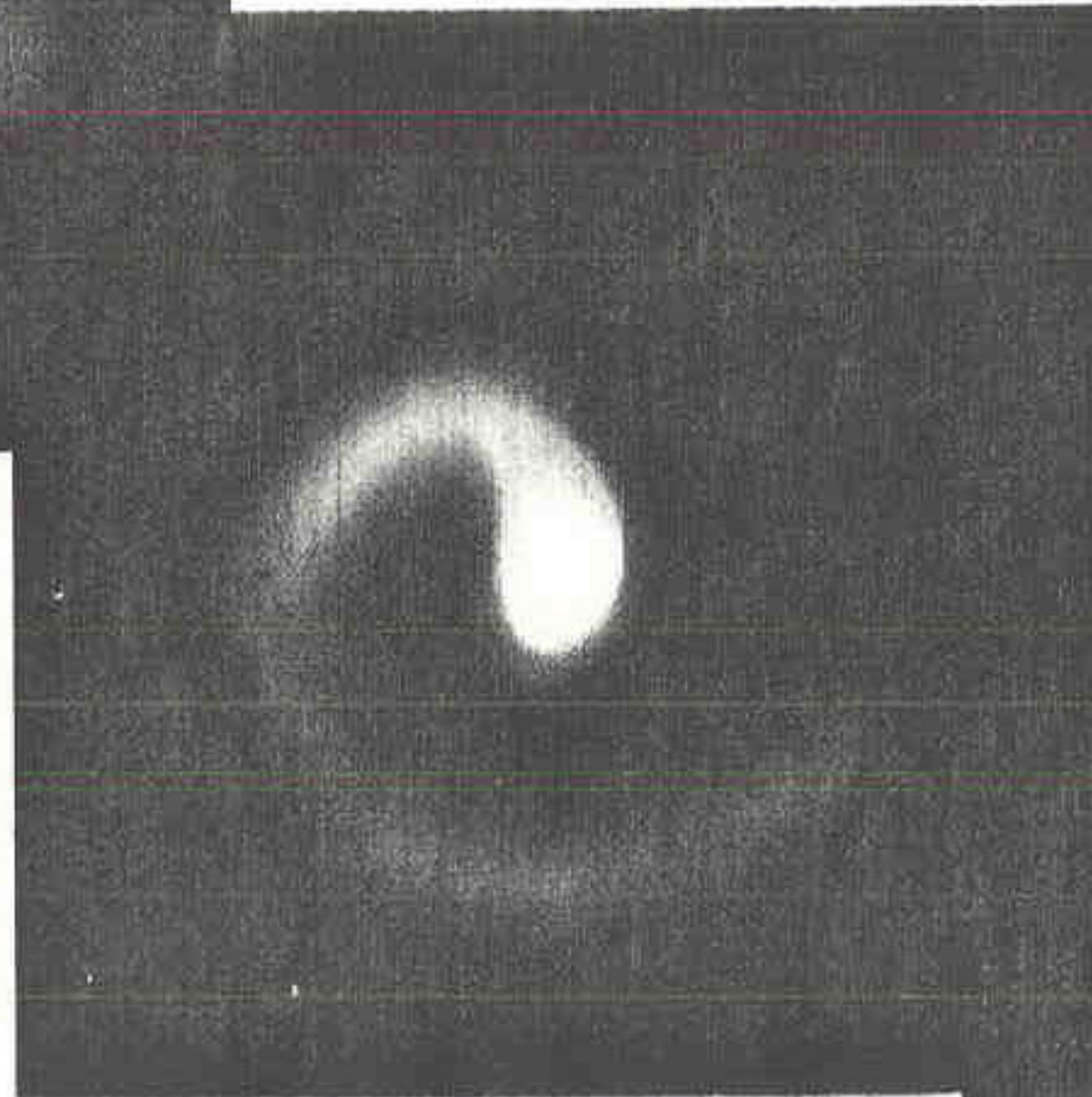
WR 104



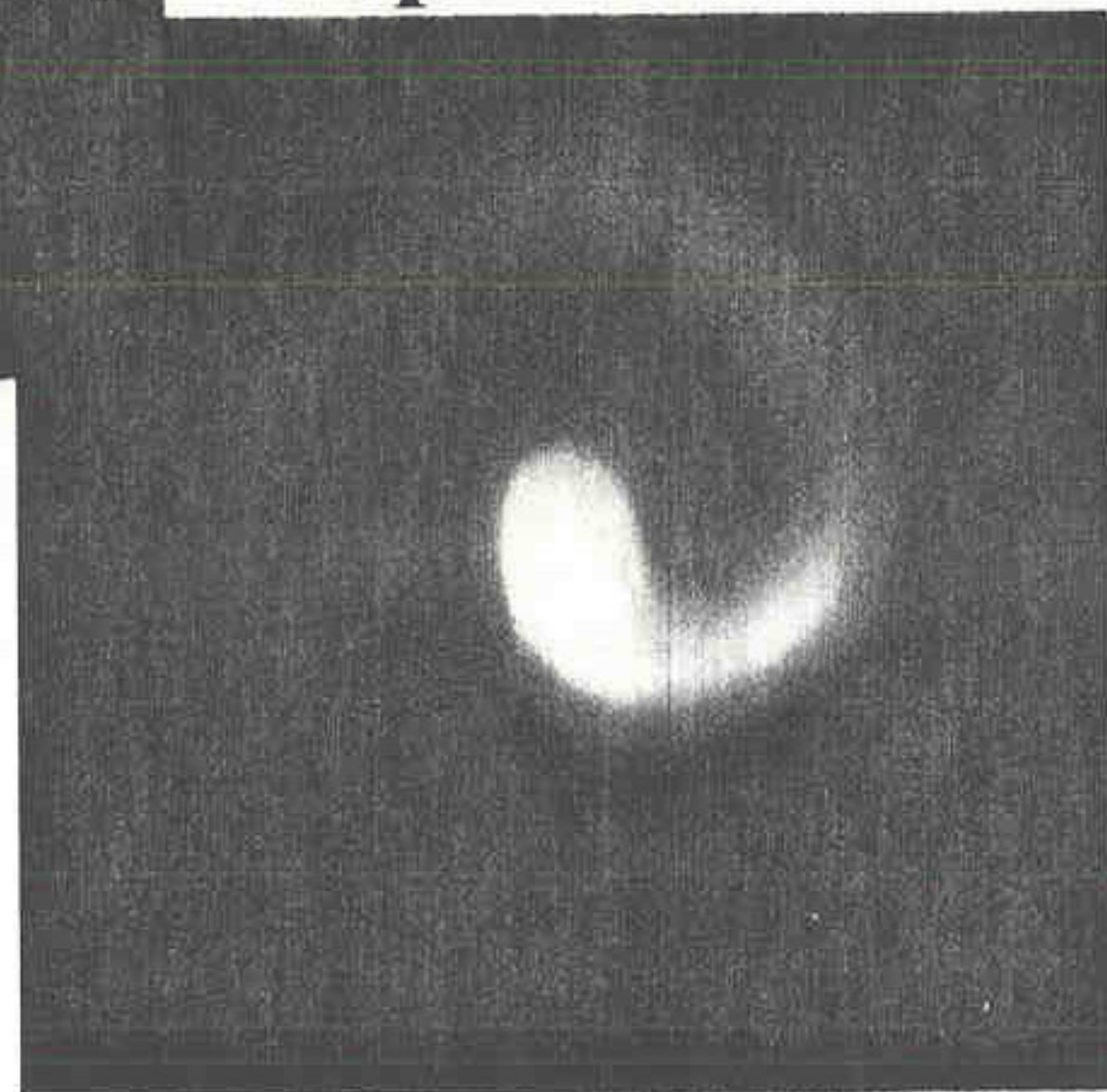
April 1998



June 1998

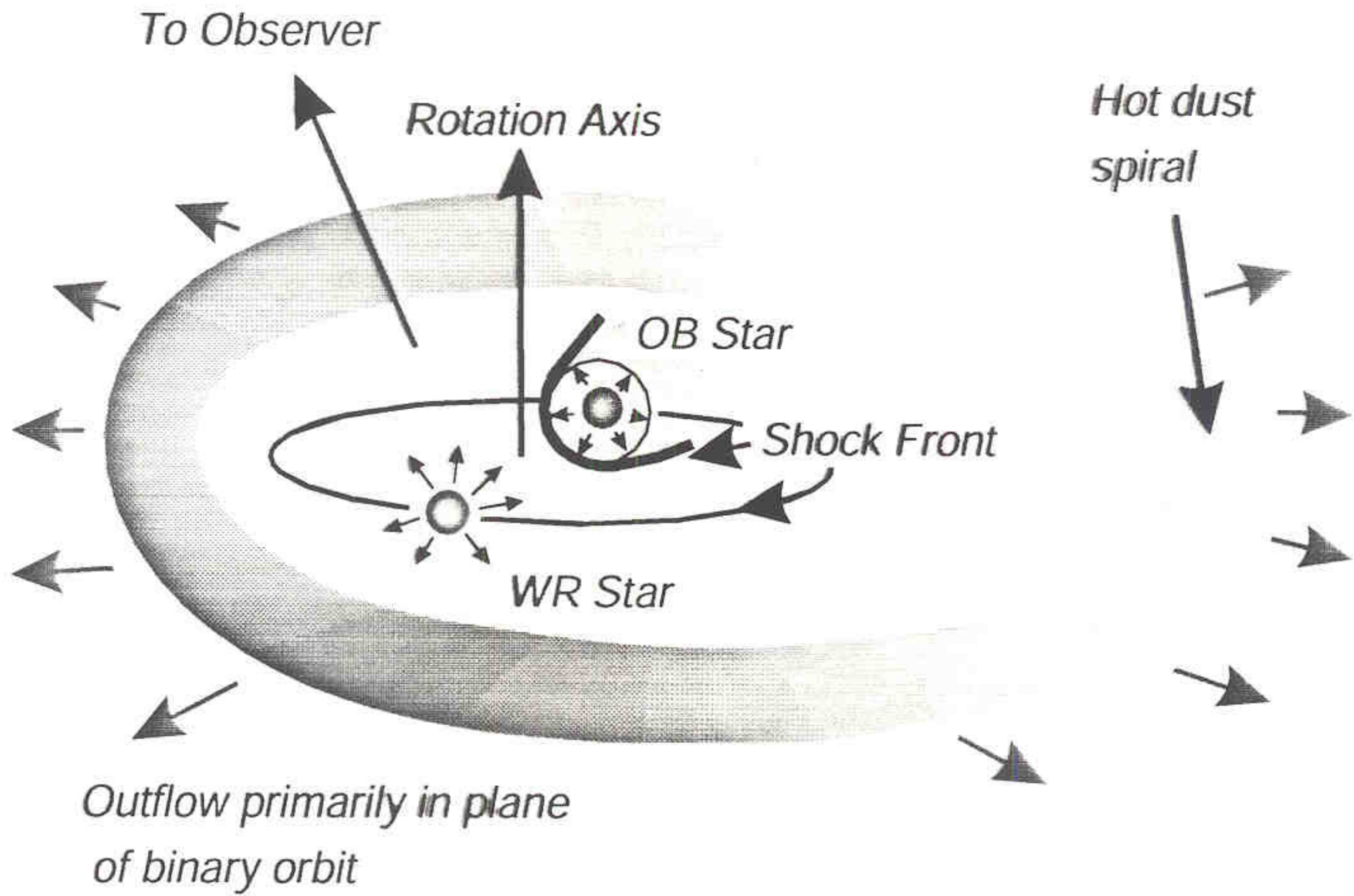


September 1998

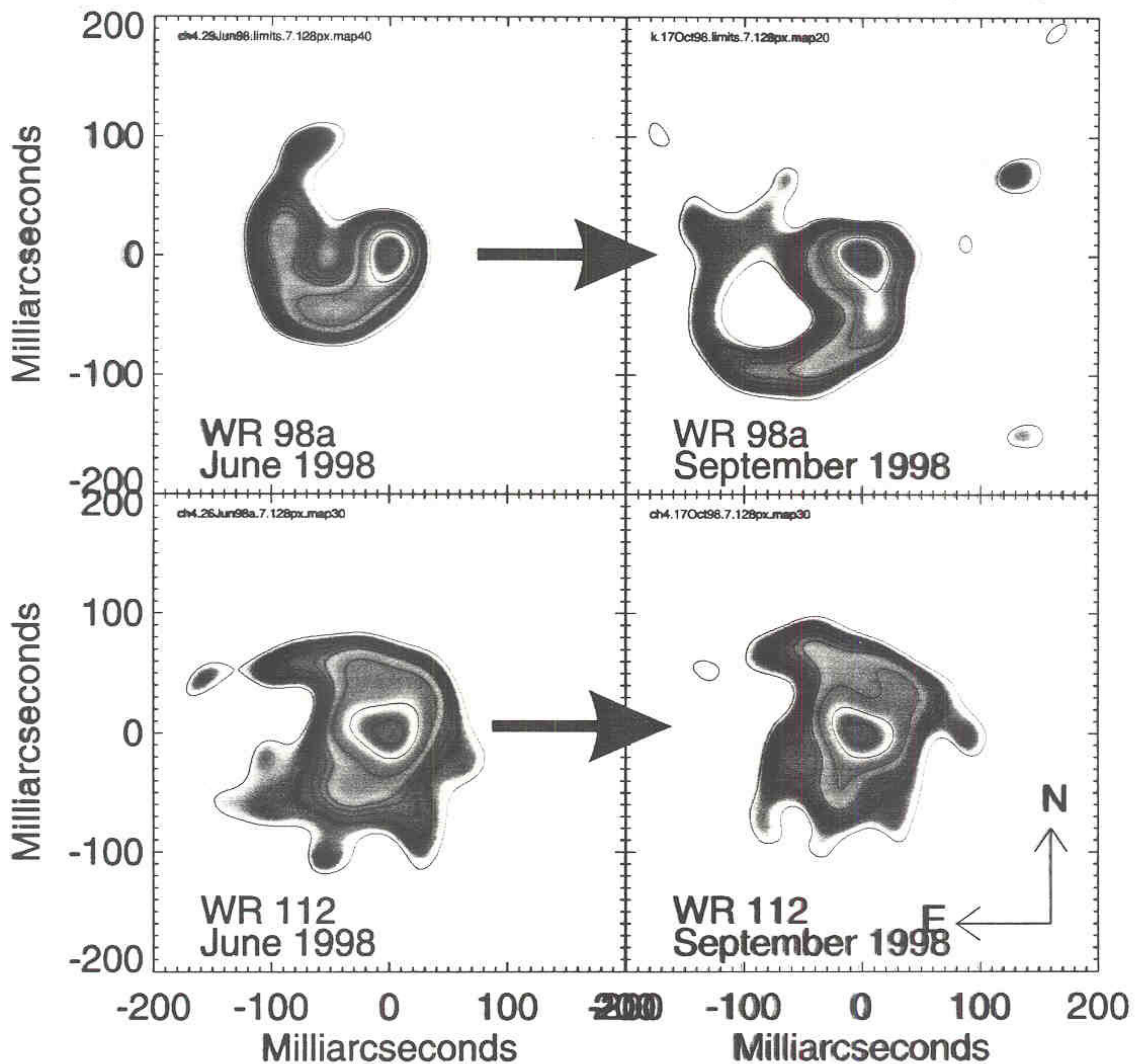


WR 104

Interacting Binary Wind Model of Spiral Outflow Around WR 104



Wolf-Rayet Dust Shells (2.2 μ m)



Herbig Ae/Be Stars

- **Began with study by Herbig (1960) of 26 pre-main sequence stars of masses $M_* > 1 M_\odot$, spectral range F0 to B0, having emission lines (Balmer).**

- **Now about 300 known.**

- **Parameters are:**

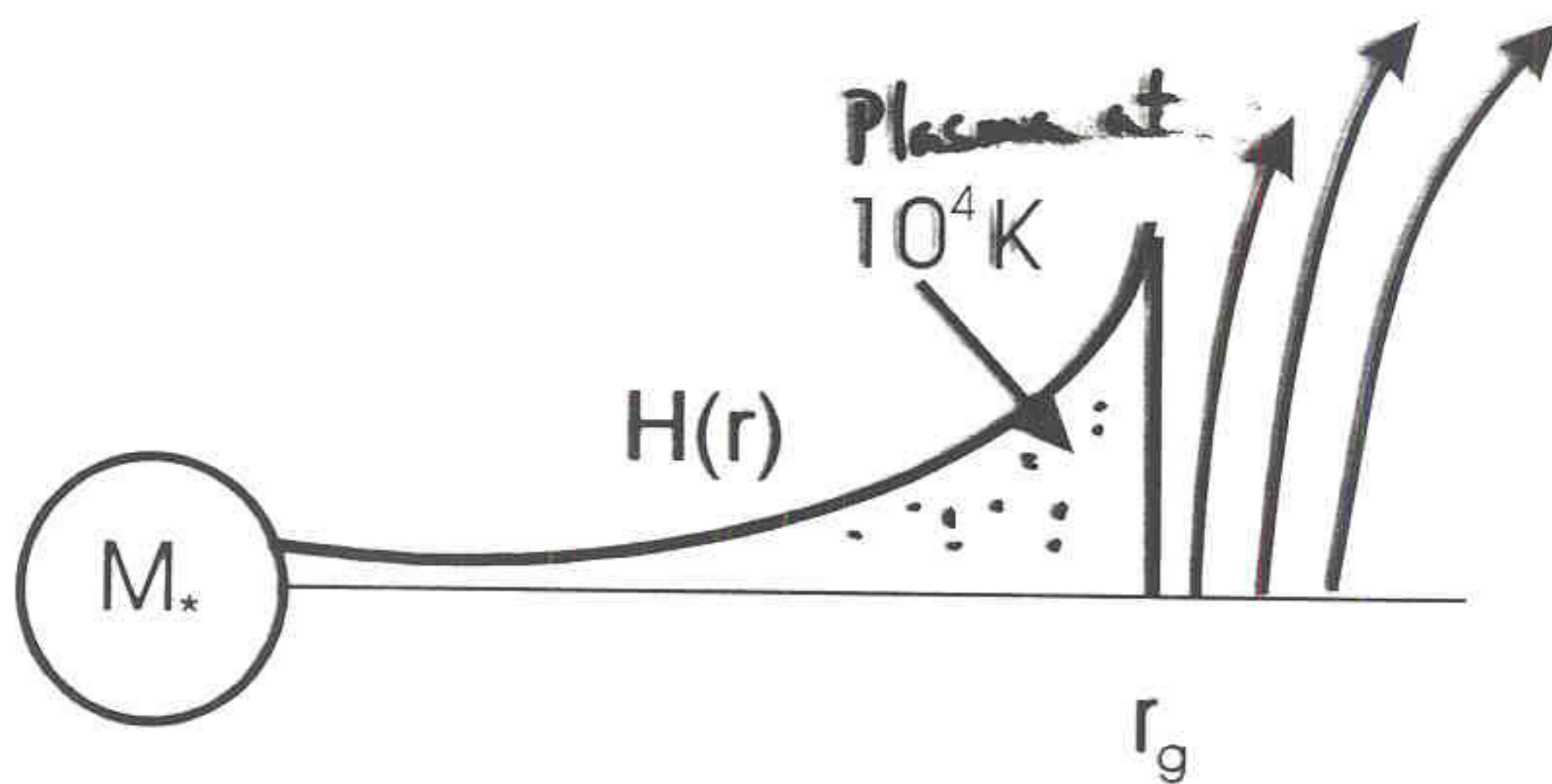
masses:	$2 M_\odot < M_* < 20 M_\odot$,
luminosities:	$2 L_\odot < L_* < 10^4 L_\odot$,
temperatures:	$8000 < T_{\text{eff}} < 30,000 \text{ K}$
ages:	$< 10^5 \text{ yr} < t < 10^7 \text{ yr}$

- **Mostly studied by their Spectral Energy Distributions (SEDs).**
- **Historical debate as to whether disk morphologies were common or unusual compared to envelope morphologies.**
- **Classified into 3 groups based on SEDs by Hillenbrand et al. (1992).**
 1. **Group I – Fitted by models with flat circumstellar accretion disks**
 2. **Group II – Fitted by models with roughly spherical envelopes**
 3. **Group III – Small IR excess, consistent with little circumstellar material left**

- Our goal is to look at some of the Herbig Ae/Be stars where disks are suggested based on SEDs and see if disks can be observed with the aperture masking technique.

Photoevaporation of Stellar Disks Application to Compact HII Regions

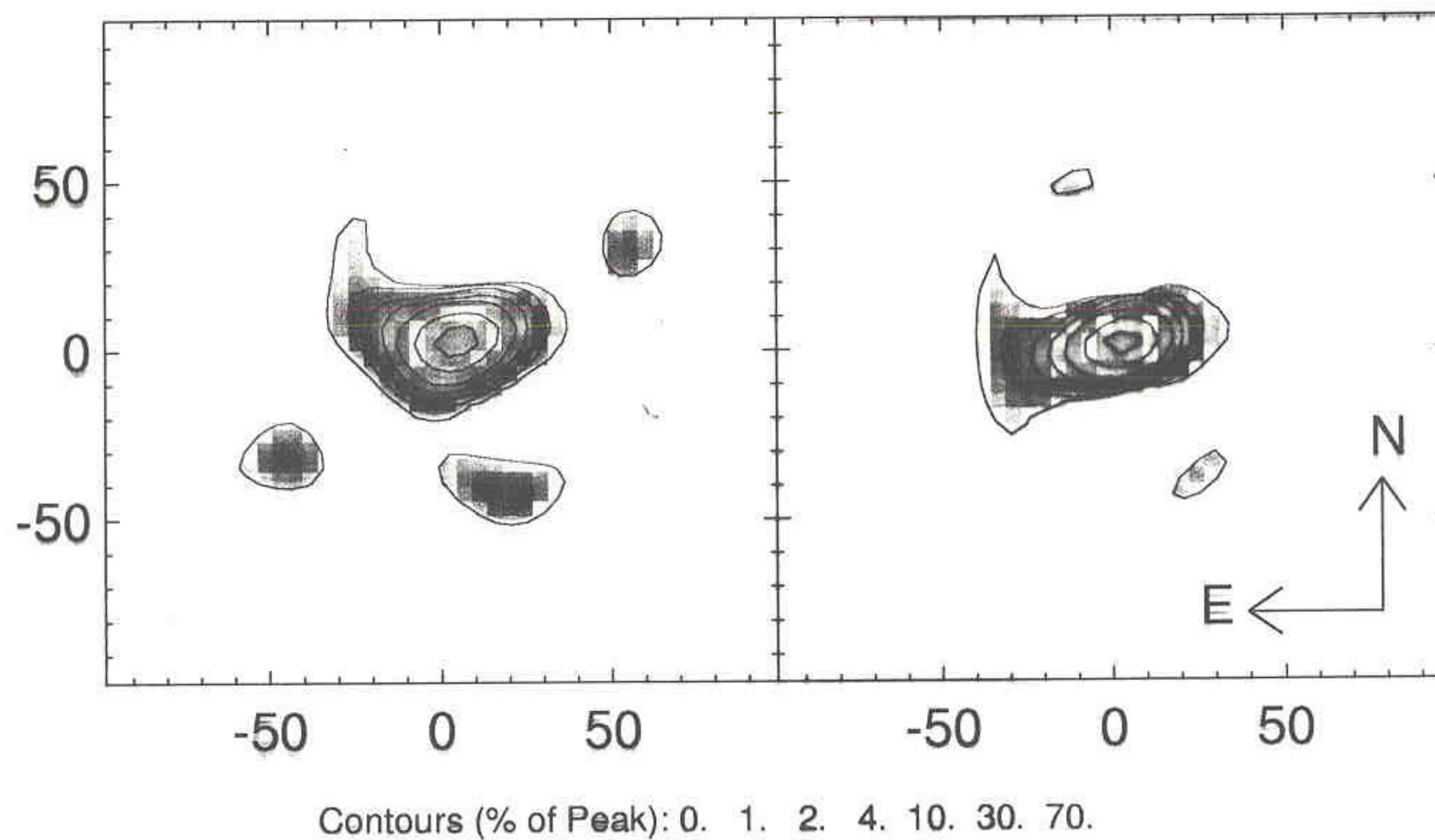
$$15 M_{\odot} < M_{*} < 65 M_{\odot}$$

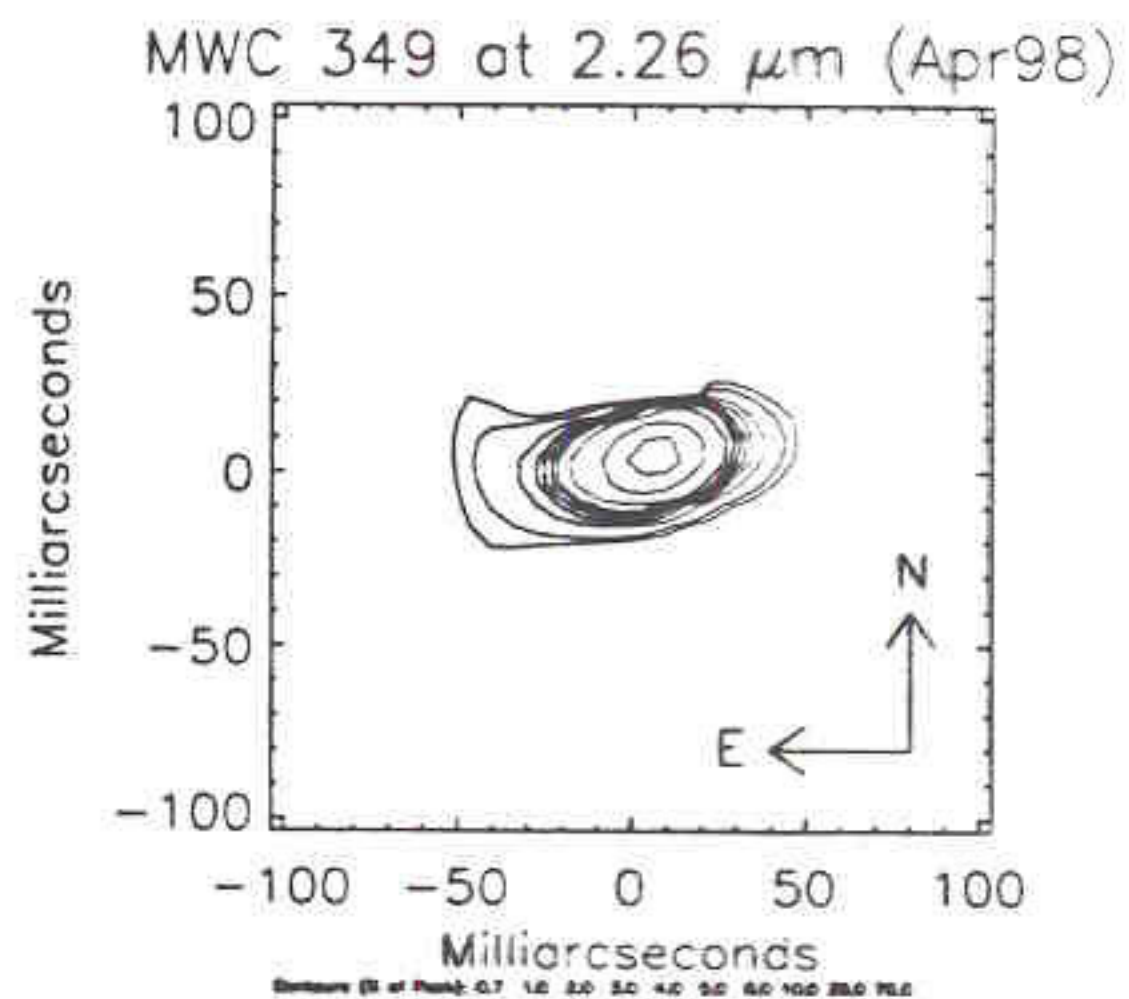
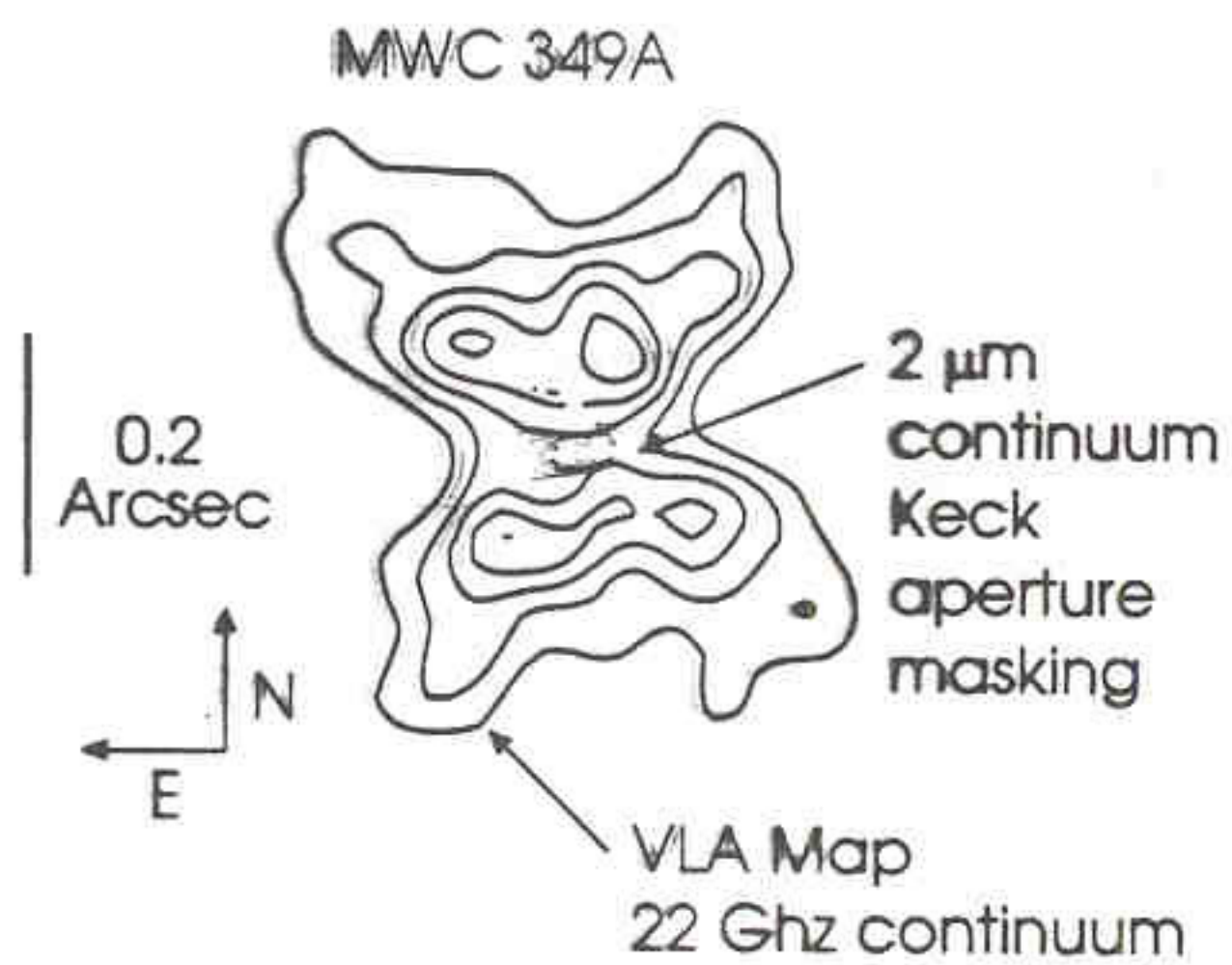


$$H(r) \propto r^{+3/2}$$

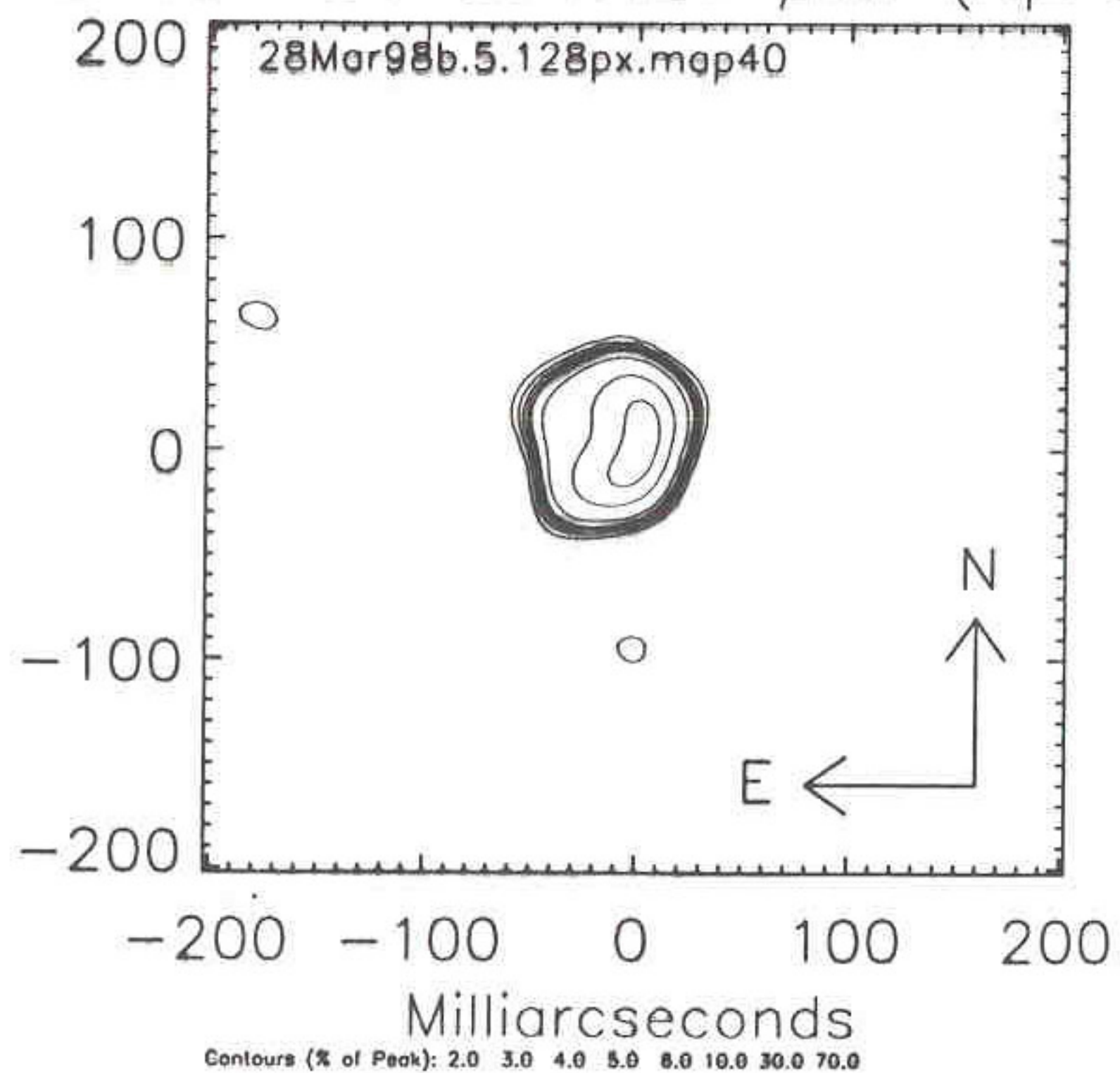
$$r_g \sim 10^{15} \left(\frac{M_{*}}{10 M_{\odot}} \right) \text{ cm}$$

MWC 349 at 1.6 and 2.2 μm (Apr98)





LkHa 101 at 2.26 μm (Apr98)



LkHa 101 at 2.26 μm (Apr98)

